

UNIVERSITY OF BELGRADE

FACULTY OF PHYSICS

Vesna I. Berec

ION-ATOM QUANTUM ENTANGLEMENT
IN A MAGNETIC FIELD BASED ON THE
SUPERFOCUSING EFFECT –
THE SPIN QUBIT PROCESSING IN
SILICON

Doctoral Dissertation

Belgrade, 2013

УНИВЕРЗИТЕТ У БЕОГРАДУ

ФИЗИЧКИ ФАКУЛТЕТ

Весна И. Берез

ЈОНСКО-АТОМСКА КВАНТНА
КОРЕЛАЦИЈА У МАГНЕТНОМ ПОЉУ
БАЗИРАНА НА ЕФЕКТУ
СУПЕРФОКУСИРАЊА –
ПРОЦЕСИРАЊЕ СПИНСКОГ КУБИТА
У СИЛИЦИЈУМУ

докторска дисертација

Београд, 2013

Thesis advisor, Committee member:

Dr Marin Tadić
Associate research professor,
Institute of Nuclear Sciences „Vinča“,
University of Belgrade.

Thesis Committee:

Prof. Dr Zoran Radović,
Professor,
Faculty of Physics,
University of Belgrade.

Prof. Dr Goran Poparić,
Associate Professor,
Faculty of Physics,
University of Belgrade.

Prof. Dr Edib Dobardžić,
Associate Professor,
Faculty of Physics,
University of Belgrade.

The Doctoral Dissertation defense date: _____

ION-ATOM QUANTUM ENTANGLEMENT IN A MAGNETIC FIELD BASED ON THE SUPERFOCUSING EFFECT – THE SPIN QUBIT PROCESSING IN SILICON

Abstract

We have theoretically and numerically examined the $\langle 100 \rangle$ thin silicon crystal and isotopically purified silicon nanocrystal in the 2 T magnetic field as a medium for the direct generation of an ion-atom entanglement obtained as a mixed quantum state of hyperpolarized $\frac{1}{2}$ nuclear spins hyperfine-coupled with electron spin, using the superfocusing channeling effect. Numerical modeling and characterization of entanglement as a state vector in the Hilbert space of the composite system that cannot be expressed as the direct tensor product of states: $|\psi_1\rangle, |\psi_2\rangle$, in a given case include mixed quantum state induced by the superimposed hyperchanneled proton beam of 1 and 2 MeV energy over electron spin states in ^{29}Si . Motivated by the fact that direct induction of ion-atom entanglement and coherent storage of quantum bits (qubits) into desired long lived quantum states could permit the precise qubit manipulation, and single qubit measurement for times which could exceed seconds, we have for the first time investigated the features and benefits of hybrid solid- state qubits under ion channeling regime, based on coupling of electron spin to nuclear spin in the isotopic, 99% pure ^{29}Si nanocrystal target. Obtained results reveal a pathway for production of a new type of memory unit for quantum processing in nanocrystalline silicon and support further exploration toward implementation of single memory unit below atomic scale aimed for information storage and solid state quantum engineering, since the achieved robust entanglement of ^{29}Si nuclear states becomes far more isolated from destructive interactions.

Keywords: Solid state qubit, Silicon, Spin, Superfocusing effect, Ion channeling, Quantum information.

Field of Science: Physics.

Research Area: Condensed Matter Physics.

UDC number: 538.9

ЈОНСКО-АТОМСКА КВАНТНА КОРЕЛАЦИЈА У МАГНЕТНОМ ПОЉУ БАЗИРАНА НА ЕФЕКТУ СУПЕРФОКУСИРАЊА – ПРОЦЕСИРАЊЕ СПИНСКОГ КУБИТА У СИЛИЦИЈУМУ

Резиме

Теоријским и нумеричким моделовањем испитиван је танак <100> кристал и изотопски пречишћени нанокристал силицијума у 2 Т магнетном пољу, као медијум за директно генерисање јон-атом квантне корелације добијене као мешано квантно стање хиперполаризованих нуклеарних $\frac{1}{2}$ спинова, спрегнутих са спиновима електрона помоћу ефекта суперфокусирања. Нумерички модел и карактеризација квантне корелације спрезања као стања вектора у Хилбертовом простору који не могу бити изражени директним тензорски производом квантних стања: $|\psi_1\rangle$, $|\psi_2\rangle$, у датом случају укључује мешано квантно стање индуковано суперпонираним хиперканалисаним протонским снопом енергије 1 и 2 MeV на спинским стањима електрона у ^{29}Si . Мотивисани чињеницом да директна индукција јонско-атомске квантне корелације и кохерентног складиштења квантних битова (кубита) у пожељна „дуго-живућа“ квантна стања може омогућити прецизну манипулацију кубита и јединствено мерење кубита у времену које превазилази секунде, истраживање особина и предности хибридних кубита у кондензованој материји смо први пут извршили у режиму јонског каналисања, базирано на ефекту спрезања електронског и нуклеарног спина у изотопски, 99% чистој мети нанокристала ^{29}Si . Добијени резултати откривају пут ка продукцији новог типа меморијске јединице намењеној квантном процесирању у нанокристалном силицијуму и подржавају даље истраживање ка имплементацији јединствене меморијске јединице на субатомској скали намењеној складиштењу информације и квантном инжењерингу у чврстом стању, обзиром да остварена снажна квантна корелација ^{29}Si нуклеарних спинских стања постаје далеко изолованија од деструктивних интеракција.

Кључне речи: Кубит у системима чврстог стања, Силицијум, Спин, Ефекат суперфокусирања, Јонско каналисање, Квантна информација.

Научна област: Физика.

Ужа научна област: Физика кондензоване материје.

УДК број: 538.9

Acknowledgments

There are many people who have helped me during the course of my Ph.D., and to whom I am greatly indebted. First and foremost my parents for their constant support during these years deserve the credit for where I am today.

My thesis advisor, dr Marin Tadić and the University of Belgrade Physics Department, deserve avowal for giving me a chance to prove myself as a scientist. Especially, I would like to express my gratitude to the thesis committee for their time and support.

At last, I thank to my colleagues and my friends who were on my side of the “story” and made my experience of Ph.D. life the richer.

Dedicated to my parents

Mirko and Dragica

Contents

Title Page	i
Abstract	ii
Acknowledgments	iii
Dedication	iv
Table of Contents	v

I Main Principles

Chapter 1

Silicon – based solid state qubits

1.1 Introduction	1
1.2 Thesis outline and structure.	3

Chapter 2

Main concepts involving the spin qubit quantum information processing

2.1 Pure and mixed states	6
2.2 Entanglement.	9
2.2.1 Classical correlation versus quantum correlation & nonlocality.	10
2.2.2 Separability:	11
2.3 Entangled states.	12
2.3.1 Bell state.	12
2.3.2 Werner state.	14
2.4 Tailoring entanglement over the four - dimensional space organized as a 2×2 tensor product space.	16
2.5 The Qubit	20

Chapter 3

Manipulation of semiconductor spin qubits

3.1 Introduction	23
3.2 Manipulation of a single spin.	24
3.2.1 Isolated spin in a static magnetic field	24
3.2.2 Rotating reference frame.	26
3.3 Spin precession and magnetic resonance condition	28
3.4 Interaction between two electrons	30
3.5 A magnetic coupling between nuclear spin and electron spin.	33
3.5.1 Isotropic and anisotropic hyperfine interaction.	33
3.6 Electron – nuclear spin interaction.	38
3.6.1 Static Hamiltonian.	38
3.6.2 Exact diagonalization of the static Hamiltonian.	39
3.7 Interaction of electron-nuclear spin system with electromagnetic radiation.	43

Chapter 4

Ion channeling in crystals

4.1 Introduction	46
4.1 Continuum Model.	47
4.2 Thomas-Fermi interaction potential in continuum approximation	48

II Results

Chapter 5

Superfocusing of channeled protons in a $\langle 100 \rangle$ Si thin crystal

5.1 Introduction	53
----------------------------	----

5.2 Semiclassical model of the superfocusing effect induced by proton channeling . . .	55
5.3 Results and Discussion	57

Chapter 6

Quantum entanglement and spin control in silicon nanocrystal

6.1 Introduction	72
6.2 The logarithmic singularity under continuum approximation	72
6.3 Quantum model of the superfocusing effect for excitation and coherent control of electron and nuclear spin states	75
6.4 Mapping of quantum states, transformation matrix and mixed coupling induced by superimposed CP field	80
6.5 Numerical methods and simulation model	87
6.6 Discussion	91

Chapter 7

7.1 Concluding remarks and outlook.	99
---	----

Bibliography	101
-------------------------------	-----

I

MAIN PRINCIPLES

Chapter 1

Silicon – based solid state qubits

1.1 Introduction

The most exploited material in the field of Micro- and Nanoelectronics, crystalline silicon (Si) has taken the central role in condensed matter systems due to its scalability in compatible, multifunctional materials, planar device interconnection, and its proven capability to operate as a single quantum device [1]. Silicon integrated circuits have provided the computation capacity that created the Information Age [2]. In particular, spin qubits based in silicon are currently one of the most promising architectures for quantum information processing (QIP). Among others, one especially favorable feature is that spins in silicon possess long coherence times [3, 4]. Moreover, silicon quantum electronics has already demonstrated fast operation and a proven record of scalable integration over variety of other materials [5]. As a result, the full benefit of existing silicon technology is now disposable to facilitate advantages of spin qubits based in crystalline Si on nanoscale. Recent results of the exchange coupling in coupled nanocrystals (QD) have revealed the promising potential of these structures for the purpose of quantum processing [6, 7].

Moreover, as today's nanotechnology focus becomes primarily oriented toward the production and manipulation of materials at the subatomic level, allowing the performance and complexity of interconnects when the device density accepts more than hundreds devices on a single chip, the manipulation of semiconductor nanostructures at the subatomic level including the engineering of Si isotope superlattices in which alternating layers of different isotopes were formed with nanoscale precision [8, 9] represents the next natural step. Silicon naturally exists in the form of three stable isotopes: ^{28}Si , ^{29}Si and ^{30}Si , characterized with the fixed relative abundance: 92.2% (^{28}Si), 4.7% (^{29}Si) and 3.1% (^{30}Si), and associated with nuclear spin differences: $I = 1/2$ for ^{29}Si , but $I = 0$ for ^{28}Si and ^{30}Si , where the mass difference between the isotopes represents important feature at the nanometer scale length.

A Kane's famous proposal of phosphorus-doped silicon (Si:P) quantum computer [10] was put in front plane the implementation of solid-state spin architectures in QIP. Following these steps, a single silicon atom as a bit carrier for processing and storing of information [11] has been proposed recently. A phosphorus atom attached at the end of the ^{29}Si nuclear spin chain was suggested for the initialization and read-out of the ^{29}Si nuclear spins.

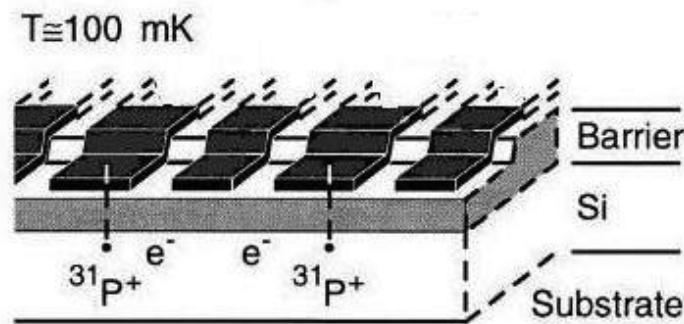


Figure 1.1: Schematic of Kane's proposal for a nuclear-spin quantum computer utilized on ^{31}P donors in a silicon matrix [10].

In contrary to recently investigated doped silicon architectures [12], where the main problem of decoherence in view of the temperature dependent spin-boson, and temperature independent spin-spin mechanisms predominates, a long quantum information coherence time of 25 seconds for ^{29}Si nuclear spins at room temperature as one of the main the criteria for nuclear spin to be utilized as a memory qubit, was experimentally confirmed [13], while the isotopically purified silicon was simultaneously investigated to prove that it would be possible to fabricate the single wire of ^{29}Si atoms exclusively [14-16]. Moreover, the recent experimental study of coherent quantum information transfer involving ^{29}Si nuclear spins in silicon, actually demonstrate advantage of ^{29}Si nuclear spins as excellent candidates for solid state qubits [17, 18].

However, to succeed in the way of QIP implementation one still needs to resolve many open questions. For instance, the small magnetic moment of nuclear spin prevents the substantial equilibrium polarization at accessible experimental conditions operated

under nuclear polarization techniques like dynamic (DNP), and optical nuclear polarization (OPN) [19]. Besides, the challenges of effective initialization and the read out of the nuclear spin states are necessary tasks which must be addressed and improved.

1.2 Thesis outline and structure

This thesis presents novel theoretical insights and progress towards comprehending and controlling the complex environment of a silicon-based solid-state qubit. The theoretical study of the electron – nuclear $\frac{1}{2}$ spin qubits coupling, initialization and coherent control in highly confined silicon environment, followed by numerical analysis, modeling and simulation of a new QIP concept based on the superfocusing effect [20] suitable for addressing the individual nuclear spins in isotopically purified nanocrystalline ^{29}Si as the physical qubits [21, 22] are presented. Guided by the anisotropic hyperfine interaction the two-qubit operations are for the first time performed on these physical qubits by controlling exchange coupling J as a function of superfocusing field. Logical qubits are encoded into a subspace of the physical qubits, so that the exchange coupling alone enables universal solid state quantum computation. The presented study employs the quantum communication protocol based on the transmission model of hyperchanneled protons and the quantum Monte Carlo simulations of spin system in silicon nanocrystal. Numerical solutions of equations of motion of protons correspond to hyperchanneled proton spatial and angular distributions in the phase space.

In this thesis the quantum electrodynamical nature of entanglement as an essential quantum property that establishes mutual predictable correlation of particles of energy/matter is investigated using the precisely guided proton beam through a ^{29}Si nanocrystal axial channel on a basis of screened Molière interaction potential. It is well known that information on the spin state of a particle in the quantum entanglement state — whether the given particle spin is oriented parallel or anti-parallel — allows simultaneous information about the spin of the other particle which belongs to entanglement pair. Quantum entanglement allows qubits to simultaneously interact and to transfer the quantum state information regardless to the distance between them, in the process of communication that is not limited by the speed of light. The correlated particles will retain the status of entanglement if they are in isolated environment. In

accordance with afore mentioned, the great potential of quantum entanglement can be exploited for quantum information storage and processing [10], development and implementation of chip integrated quantum protocols. In that context, the process of coupling of electron with $\frac{1}{2}$ nuclear quantum spin states [23] in silicon nanocrystal target, mediated by the polarized nuclear spin states of hyperchanneled protons through the quantum entanglement, allows the transfer of information originally deposited in the electrons to the spin state of the host ^{29}Si . The result is an extremely fast transfer of quantum information in long-lived quantum state (polarization) of a nuclear spin, further addressable to a photon, with corresponding polarization/frequency. Obtained results reveal a pathway for production of a new type of memory unit for quantum processing in silicon.

This thesis is organized in two main sections.

The theoretical background and mathematical formalism closely tight to the focus of this thesis are decidedly presented in the first part composed of three chapters. After introductory informations, chapter 2. describes general quantum concepts necessary for explanation of spin qubit quantum information processing. Upon formulation of pure and mixed quantum states it describes the correlation between quantum behavior and nonlocality of entanglement, further addressing discussion to special bipartite entangled states. Chapter 3. explains magnetic field effect on quantum states creation and manipulation, while chapter 4. provides the fundamentals of channeling theory in solids with special emphasis to Continuum model, axial confinement, hyperchanneling, and Molière approximation of Thomas-Fermi interaction potential, giving in such way the main theoretical preliminaries to results presented in next section.

Part II represents the exposition of my published research including results, discussion and concluding remarks. It is composed of three chapters. The chapter 5. is devoted to theoretical-semiclassical background and detail numerical study of the new ion channeling phenomena called the superfocusing effect [20], demonstrating the precision in spatial resolution beyond limits of the Bohr radius, while the sixth chapter illuminates the quantum theory of the superfocusing effect as a driving force for electron spin coherent control and precise manipulation and entanglement of nuclear spin quantum states in isotopically engineered ^{29}Si nanocrystal host [21, 22], described by extensive

analytical, numerical and simulation study. Finally, the chapter 7. gives concluding remarks and future prospective.

Chapter 2

Main concepts involving the spin qubit quantum information processing

2.1 Pure and mixed states

Pure quantum mechanical state is described by a state vector $|\Psi\rangle$ in the Hilbert space \mathcal{H} . Any state vector can be expanded as a linear combination of basis elements within chosen basis for the Hilbert space, like $|\Psi\rangle = \sum_i^d c_i |a_i\rangle$, where the c_i are complex coefficients, $|a_i\rangle$ denotes the selected basis and $d = \dim \mathcal{H}$. Appliance of the normalization on the state vectors gives: $\langle\Psi|\Psi\rangle = 1 \Leftrightarrow \sum_i^d |c_i|^2 = 1$.

The expectation value of an observable \hat{A} with respect to the state $|\Psi\rangle$ can be calculated by $\langle\hat{A}\rangle = \langle\hat{A}\rangle_\Psi = \langle\Psi|\hat{A}|\Psi\rangle$.

For a bipartite system, consisting of subsystems A and B , the total Hilbert space \mathcal{H} is divided into two subspaces: $\mathcal{H}_{(A)}$ and $\mathcal{H}_{(B)}$ with corresponding state vectors $|\psi_A\rangle$, and $|\psi_B\rangle$ representing the state of the subsystem A and B , respectively.

If the state of two qubits is factorized, as $|\Psi\rangle = |\psi_A\rangle \otimes |\psi_B\rangle$ ¹, the coefficients of the expansion $\langle a, b | \Psi \rangle$, are represented with respect to the basis states of the form $|a\rangle \otimes |b\rangle$ and depend on only one subspace each. In that case, due to the fact that \hat{A} acts only on $\mathcal{H}_{(A)}$, the expectation value of an operator $\hat{A}: \mathcal{H}_{(A)} \rightarrow \mathcal{H}_{(A)}$ is

¹ The above description in terms of state vectors is only valid for pure states.

$$\begin{aligned}
\langle \hat{A} \rangle &\equiv \langle \Psi | \hat{A} | \Psi \rangle = \sum_{a,a',b,b'} \langle \Psi | a', b' \rangle \langle a', b' | \hat{A} | a, b \rangle \langle a, b | \Psi \rangle \\
&= \sum_{a,a',b} \langle \Psi | a', b \rangle \langle a' | \hat{A} | a \rangle \langle a, b | \Psi \rangle,
\end{aligned} \tag{2.1}$$

where we have used a closure relation:

$$\sum_{a,b} |a, b\rangle \langle a, b| = I, \text{ and } \langle a, b | \hat{A} | a', b' \rangle = \langle a | \hat{A} | a' \rangle \langle b | b' \rangle = \langle a | \hat{A} | a' \rangle \delta_{bb'}. \tag{2.2}$$

Using the following density operator

$$\rho_{aa'} \equiv \sum_b \langle a, b | \Psi \rangle \langle \Psi | a', b \rangle, \tag{2.3}$$

we can express the expectation value of an observable \hat{A} by tracing over all states of the composite system: $\langle \hat{A} \rangle = \text{Tr}(\rho \hat{A})$.

Then, defining $c_a \equiv \langle a | \Psi_A \rangle$ and $c_b \equiv \langle b | \Psi_B \rangle$, from $\rho_{aa'}$ we obtain

$$\rho_{aa'} = \sum_b c_a c_b c_{a'}^* c_b^* = c_a c_{a'}^* \sum_b |c_b|^2 = c_a c_{a'}^*, \Rightarrow \rho = |\psi_A\rangle \langle \psi_A|, \tag{2.4}$$

that is, for given separable spaces, even if we do not have the information on c_b , the closure relation holds for the basis $\{|b\rangle\}$.

Such states, called the *pure states* possess the following important property of the density operator:

- the density operator corresponding to a pure state is a projector:

$$\rho = \rho^2 \Leftrightarrow |\psi_A\rangle \text{ is a pure state.}$$

- $\text{Tr}(\rho^2) = 1$ for a pure state.

To guarantee that ρ really describes a physical state it has to satisfy the following properties:

Hermitian: $\rho^\dagger = \rho$.

Positive semi-definite: $x^* \rho x \geq 0, \forall x \in \mathbb{C}^N$.

Normalization: $\text{Tr}(\rho) = 1$.

A *mixed state* is identified if the considered quantum mechanical system has a particular probability p_i to be in one state out of a whole set of states $|\Psi_i\rangle$. Then, a density operator is defined as a convex combination of pure state projectors weighted with a corresponding probability like: $\rho = \sum_i p_i |\Psi_i\rangle\langle\Psi_i| = \sum_i p_i \rho_i$, where $\sum_i p_i = 1, p_i \geq 0$.

For the mixed state the following properties hold:

- $\rho \neq \rho^2$.
- $\text{Tr}\rho^2 < 1$.

A mixed state is characterized by a measure of purity² or mixedness: $P = \text{Tr}\rho^2$, where the minimal amount of purity depends on the dimension of the state: $P = \frac{1}{d}, d = \dim(\mathcal{H})$.

The whole physical information of the statistical ensemble of the mixed state is expressed by the density operator ρ because of the lack of information in which ensemble $\{p_i, \rho_i\}$ the mixed state is precisely decomposed.

As a result, for an observable \hat{A} in case of a mixed state the expectation value can be presented as $\langle \hat{A} \rangle = \langle \hat{A} \rangle_\rho = \sum_i p_i \langle \Psi_i | \hat{A} | \Psi_i \rangle = \text{Tr} \rho \hat{A}$.

² For pure state the measure of purity is always equal to one, $P = 1$.

"If, without in any way disturbing a system, we can predict with certainty the value of a physical quantity, then there exists an element of physical reality corresponding to this physical quantity."

- Definition of physical reality from the EPR paper.

2.2 Entanglement

Entanglement was, historically, first recognized by Einstein, Podolsky and Rosen (EPR) [24] and by Schrödinger. Einstein called entanglement a "spukhafte Fernwirkung" or "spooky action at distance", while Schrödinger [25] stated that entanglement is the essence of quantum mechanics. By assigning an independent and objective reality to the physical properties of the separated subsystems of a composite system, they have imposed a description of fundamental differences between quantum and classical picture of nature called "local realism". The most significant consequence of later formalism are further revealed constraints on the predictions of spin correlations in the form of the so-called Bell's inequalities [26] which can be violated by certain quantum mechanical states. Those constraints have implied the quantum correlation aspect of inseparability and emphasized the feature of quantum mechanics called "nonlocality" which are one of the most apparent markers of entanglement.

2.2.1 Classical correlation versus quantum correlation & nonlocality

Entanglement represents more than a simple correlation between subsystems. For instance, subsystems A and B appear uncorrelated if $|\psi\rangle_{AB}$ is separable, although the two spins in separable state $|\psi\rangle_{AB} = |\uparrow\rangle_A \otimes |\uparrow\rangle_B = |\uparrow_A \uparrow_B\rangle = |00\rangle$,³ are definitely correlated in the manner they are both pointing in the same direction⁴. The former state can be prepared purely locally without allowing connection of spins A and B , by sending a classical message to two different, separated preparers requiring of both of them to prepare a spin pointing along the z -axis by applying local unitary transformations of the form $U_A \otimes U_B$.

On contrary, the only way to transform the former state into an entangled one like $\frac{1}{\sqrt{2}}(|\uparrow_A \uparrow_B\rangle + |\downarrow_A \downarrow_B\rangle)$ is to apply a collective unitary transformation to the state. To perform this unitary to entangle A and B means allowing for the two subsystems to directly interact with one another.

This is the reason that the correlations between A and B in an entangled state have a different character than those in a separable state. The crucial difference is that separable states correspond to the classically correlated ones, while entangled states are non-classically correlated and cannot be described as mixtures of direct products states, prepared locally.

³ Qubit state is represented in the Pauli basis, $\{|\uparrow\rangle, |\downarrow\rangle\}$ and in computational basis, $\{|0\rangle, |1\rangle\}$.

⁴ Two electrons with spin oriented towards positive z -axis will exhibit perfect correlation when are measured in the z basis (the outcome will always point to spin-up) but no correlation at all in the x or y bases.

If we consider a quantum correlation of a bipartite system whose Hilbert space is constructed by the tensor product of the Hilbert spaces of the two subsystems $\mathcal{H}=\mathcal{H}_{(A)} \otimes \mathcal{H}_{(B)}$, its density operators can not be written in such a product form like the Hilbert space.

If former is actually possible we call the state separated and can formulate the following definition.

2.2.2 Separability:

Conversely to entangled state, which is nonlocal and represents a global feature of the given Hilbert space, separable state [27] is not quantum correlated. It is produced solely ”classically” by local preparations of the subsystems.

If a state ρ can be written as the convex combination of product states like: $\rho = \sum_i p_i \rho_{i(A)} \otimes \rho_{i(B)}$, then ρ is called separable. Here $\rho_{(A)}$ and $\rho_{(B)}$ are density matrices of the subsystems and the weights satisfy conditions $p_i \geq 0$ and $\sum_i p_i = 1$.

The set of all separable states is convex. In general, any state can be expressed by $\rho = \sum_{i,j} p_{i,j} \rho_{i(A)} \otimes \rho_{j(B)}$.

A *pure state* $|\Psi\rangle$ is called *separable* (not entangled) iff it can be factorized and written as a tensor product of the subsystems state vectors: $|\Psi\rangle = |\psi_A\rangle \otimes |\psi_B\rangle$, otherwise it is entangled. An example for a pure separable state is: $|\psi\rangle_{AB} = |\uparrow\rangle_A \otimes |\uparrow\rangle_B = |\uparrow_A \uparrow_B\rangle = |00\rangle$ in logical (computational basis).

A *mixed state* ρ is called *separable* iff it can be written as a convex combination of pure product states:

$$\rho = \sum_i p_i |A_i\rangle\langle A_i| \otimes |B_i\rangle\langle B_i| = \sum_i p_i \rho_{i(A)} \otimes \rho_{i(B)}, \quad (2.5)$$

where $|A_i\rangle$ and $|B_i\rangle$ are state-vectors on the spaces $\mathcal{H}_{(A)}$ and $\mathcal{H}_{(B)}$ of subsystems A and B respectively and $0 \leq p_i \leq 1$, such that $\sum_i p_i = 1$ $\langle A_i | A_i \rangle \neq \delta_{i,j}$. In general $\langle A_i | A_i \rangle \neq \delta_{i,j}$, $\langle B_i | B_i \rangle \neq \delta_{i,j}$.

An example for a mixed separable state that contains classical correlations, but no quantum correlations, is $\rho = \frac{1}{2}(|\uparrow\uparrow\rangle\langle\uparrow\uparrow| + |\downarrow\downarrow\rangle\langle\downarrow\downarrow|)$.

2.3 Entangled states

If a state ρ is not separable then it is called entangled. Under local unitary operations any non-separable state stays entangled like $\rho \rightarrow \rho' = (U_A \otimes U_B) \rho (U_A \otimes U_B)^\dagger$ where both unitary operators, U , satisfy $U^\dagger U = U U^\dagger = 1$. The two entangled state density operators ρ and ρ' are equivalent.

Examples for pure entangled states are the Bell states. The singlet state is one of them:

$$|singlet\rangle = \frac{1}{\sqrt{2}} = (|\uparrow\downarrow\rangle - |\downarrow\uparrow\rangle) \text{ and we will use it later on.}$$

2.3.1 Bell state

Maximally entangled pure states are called the Bell states. The Bell states possess purity equal to 1. In a two-qubit system, where the Hilbert space is of the form $\mathbb{C}^2 \otimes \mathbb{C}^2$, a set of four Bell states builds a basis for all states. These states are represented in the Pauli basis $\{|\uparrow\uparrow\rangle, |\uparrow\downarrow\rangle, |\downarrow\uparrow\rangle, |\downarrow\downarrow\rangle\}$ and corresponding computational basis $\{|00\rangle, |01\rangle, |10\rangle, |11\rangle\}$ [28] as following:

$$\begin{aligned}
|\Psi^-\rangle &= \frac{1}{\sqrt{2}} |\uparrow\downarrow\rangle - |\downarrow\uparrow\rangle = \frac{1}{\sqrt{2}} |01\rangle - |10\rangle, \\
|\Psi^+\rangle &= \frac{1}{\sqrt{2}} |\uparrow\downarrow\rangle + |\downarrow\uparrow\rangle = \frac{1}{\sqrt{2}} |01\rangle + |10\rangle, \\
|\Phi^+\rangle &= \frac{1}{\sqrt{2}} |\uparrow\uparrow\rangle + |\downarrow\downarrow\rangle = \frac{1}{\sqrt{2}} |00\rangle + |11\rangle, \\
|\Phi^-\rangle &= \frac{1}{\sqrt{2}} |\uparrow\uparrow\rangle - |\downarrow\downarrow\rangle = \frac{1}{\sqrt{2}} |00\rangle - |11\rangle.
\end{aligned} \tag{2.6}$$

The corresponding density matrices in the computational basis are

$$|\Psi^\pm\rangle\langle\Psi^\pm| = \frac{1}{2} \begin{pmatrix} 0 & 0 & 0 & 0 \\ 0 & 1 & \pm 1 & 0 \\ 0 & \pm 1 & 1 & 0 \\ 0 & 0 & 0 & 0 \end{pmatrix}, \tag{2.6.1}$$

$$|\Phi^\pm\rangle\langle\Phi^\pm| = \frac{1}{2} \begin{pmatrix} 1 & 0 & 0 & \pm 1 \\ 0 & 0 & 0 & 0 \\ 0 & 0 & 0 & 0 \\ \pm 1 & 0 & 0 & 1 \end{pmatrix}. \tag{2.6.2}$$

If the degrees of freedom of the correlated systems are higher than 2, only one state is definitely a Bell state in the general Hilbert space $\mathbb{C}^d \otimes \mathbb{C}^d$, and it is given by

$$|\Phi^d\rangle = \frac{1}{\sqrt{d}} \sum_{s=0}^{d-1} |s\rangle \otimes |s\rangle. \tag{2.7}$$

For higher-dimensional systems these states do not form a complete basis of the system leading to construction of the so-called Bell-type states which are not necessarily maximally entangled.

An example for a mixed entangled state which includes a fraction of a singlet - Bell state is a Werner state. This state is invariant under the unitary transformation $U \otimes U$, i.e., it satisfies: $\rho = U_A \otimes U_B \rho U_A^\dagger \otimes U_B^\dagger$.

2.3.2 Werner state

A Werner state [29, 30] is a two dimensional bipartite quantum state that consists of both entangled (Bell state) and a separable (mixed state). Here, we consider a pair of $\frac{1}{2}$ -spin particles with inclusion of a Bell's state singlet fraction, p , and a random fraction, $1 - p$, for mixed state:

$$\rho^W = p |singlet\rangle\langle singlet| + \frac{1}{4}(1-p)I, \quad (2.8)$$

where I is the identity matrix.

By writing the density matrix elements explicitly, with all their indices:

$$\rho_{m\mu, n\nu} = \sum_r p_r (\rho_{rA})_{mn} (\rho_{rB}), \quad (2.8a)$$

where Latin indices refer to the first subsystem A , and Greek indices to the second one B ., eq. (2.8) becomes

$$\rho_{m\mu, n\nu}^W = p S_{m\mu, n\nu} + \frac{1}{4}(1-p)\delta_{m,n}\delta_{\mu,\nu}. \quad (2.8b)$$

The corresponding density matrix is given by

$$\rho^W = \frac{1}{4} \begin{pmatrix} 1-p & 0 & 0 & 0 \\ 0 & p+1 & -2p & 0 \\ 0 & -2p & p+1 & 0 \\ 0 & 0 & 0 & 1-p \end{pmatrix}. \quad (2.9)$$

The next step considers taking the partially transpose of the density matrix with respect to one of the subsystems. The state is defined by (4×4) matrix with (2×2) blocks.

Transposition with respect to B subsystem is done by transposing each one of the four blocks, when we get:

$$\left(\rho^W\right)^{T_B} = \frac{1}{4} \begin{pmatrix} 1-p & 0 & 0 & -2p \\ 0 & p+1 & 0 & 0 \\ 0 & 0 & p+1 & 0 \\ -2p & 0 & 0 & 1-p \end{pmatrix}. \quad (2.9.1)$$

$\left(\rho^W\right)^{T_B}$ is characterized by three eigenvalues equal to $(1+p)/4$ and the fourth - lowest eigenvalue equal to $(1-3p)/4$. p is a weight for obtaining a pure singlet state in domain $0 \leq p \leq 1$, while a $1-p$ denotes a weight for an inclusion of mixed state. The purity of the state is given by $P = \frac{1+3p^2}{4}$.

Starting from $p = 0$ we get a maximally mixed state: $\rho^W = \frac{1}{4} \mathbb{I}_4$ (where the \mathbb{I}_4 is the unit matrix), and crossing over whole domain at $p = 1$ we get the fully entangled (Bell) state.

For Werner state the weight of the singlet is p , and therefore in order to hold Bell's inequality it has to fulfill the condition: $2\sqrt{2}p \leq 2$. Namely, the violation of the Bell's inequality is known as a signature for entanglement in two qubits. If a state violates the Bell inequality then we know that entanglement is present. The reverse is not true [30]. As an example of such "irreversibility" the Werner state can be separable (not entangled) only for $p \leq 1/3$, but it does not violate the Bell inequality for $p > 1/3$ when it is entangled.

If the dimension, d , of the subsystems is higher than $d = 2$ such states are called isotropic [31]:

$\rho^{iso} = \frac{1}{d^2}(1-\alpha)\mathbb{I}_{d^2} + \alpha|\Phi^d\rangle\langle\Phi^d|$, where $0 \leq \alpha \leq 1$, and $|\Phi^d\rangle$ is a general Bell state denoted by eq. (2.7).

2.4 Tailoring entanglement over the four - dimensional space organized as a 2×2 tensor product space

According to [32] for any pure state over a (finite-dimensional) \mathcal{H} space, there always exist two associate algebras generated over su_2 by any representation of \mathbb{C}^d , $d \in \mathbb{N} \setminus \{0, 1\}$ that allow factorization of a state in order to create any possible amount of entanglement.

In order to demonstrate the former statement let us consider a state ρ in a space factorized with dimension $d \times d$. Its eigenvalues $\{\rho_i\}_{i=1}^{d^2}$ are represented in the following way:

$$1 \geq \rho_1 \geq \rho_2 \geq \dots \geq \rho_{d^2-2} \geq \rho_{d^2-1} \geq \rho_{d^2} \geq 0, \quad (2.10)$$

where the bounds are result of the properties of the density operators. We denote $|i\rangle$ as the eigenvector of ρ_i .

Next, consider the subspace: $\mathbb{E} \equiv \text{span}(|1\rangle, |d^2-2\rangle, |d^2-1\rangle, |d^2\rangle)$.

If $\rho_1 > \frac{3}{d^2}$, then a selection of factorization is always possible such that ρ become entangled in \mathbb{E} .

To proof above statement we will use the reselected basis $\{|i\rangle\}$. Over the $\{|i\rangle\}$ matrix ρ is diagonal:

$$\begin{pmatrix} \ddots & \vdots & \vdots & \vdots & \vdots \\ \cdots & \rho_1 & 0 & 0 & 0 \\ \cdots & 0 & \rho_{d^2-2} & 0 & 0 \\ \cdots & 0 & 0 & \rho_{d^2} & 0 \\ \cdots & 0 & 0 & 0 & \rho_{d^2-1} \end{pmatrix}. \quad (2.11)$$

The four-dimensional space \mathbb{E} can be factorized as a 2×2 dimensional tensor product space $\mathcal{E}_a \otimes \mathcal{E}_b = \mathcal{E}$, and in particular we choose the vectors $|1\rangle$ and $|d^2-1\rangle$ to be established as maximally entangled in the new factorization [33, 34]. We define $\mathcal{Q}: \mathbb{E} \rightarrow \mathcal{E}$, the unitary operator connecting the two factorizations, as following:

$$\mathcal{Q}|1\rangle \equiv \frac{|\uparrow a \uparrow b\rangle + |\downarrow a \downarrow b\rangle}{\sqrt{2}}, \quad (2.12)$$

$$\mathcal{Q}|d^2-2\rangle \equiv |\uparrow a \downarrow b\rangle, \quad (2.13)$$

$$\mathcal{Q}|d^2\rangle \equiv |\downarrow a \uparrow b\rangle, \quad (2.14)$$

$$\mathcal{Q}|d^2-1\rangle \equiv \frac{|\uparrow a \uparrow b\rangle - |\downarrow a \downarrow b\rangle}{\sqrt{2}}, \quad (2.15)$$

where $\{|\uparrow a\rangle, |\downarrow a\rangle\}$ and $\{|\uparrow b\rangle, |\downarrow b\rangle\}$ are bases of the two subspaces.

Represented with respect to the bases: $\{|\uparrow a \uparrow b\rangle, |\uparrow a \downarrow b\rangle, |\downarrow a \uparrow b\rangle, |\downarrow a \downarrow b\rangle\}$ of \mathbb{E}

and $\{|1\rangle, |d^2-2\rangle, |d^2\rangle, |d^2-1\rangle\}$ of \mathcal{E} ,

\mathcal{Q} assumes the form:

$$\begin{pmatrix} \frac{1}{\sqrt{2}} & 0 & 0 & \frac{1}{\sqrt{2}} \\ 0 & 1 & 0 & 0 \\ 0 & 0 & 1 & 0 \\ \frac{1}{\sqrt{2}} & 0 & 0 & -\frac{1}{\sqrt{2}} \end{pmatrix}, \quad (2.16)$$

so it is easy to see that $\rho_{\mathcal{Q}}$ can be written as:

$$\rho_{\mathcal{Q}} \equiv \mathcal{Q} \rho \mathcal{Q}^\dagger = \begin{pmatrix} \frac{1}{2}(\rho_1 + \rho_{d^2-1}) & 0 & 0 & \frac{1}{2}(\rho_1 - \rho_{d^2-1}) \\ 0 & \rho_{d^2-2} & 0 & 0 \\ 0 & 0 & \rho_{d^2} & 0 \\ \frac{1}{2}(\rho_1 - \rho_{d^2-1}) & 0 & 0 & \frac{1}{2}(\rho_1 + \rho_{d^2-1}) \end{pmatrix}. \quad (2.17)$$

Next step is to show that ρ_Q violates the Peres-Horodecki criterion [35, 36], i.e., it is entangled.

Consider the partial transpose of ρ_Q with respect to the subspace \mathcal{E}_b :

$$\rho_Q^{(b)} = \begin{pmatrix} \frac{1}{2}(\rho_1 + \rho_{d^2-1}) & 0 & 0 & 0 \\ 0 & \rho_{d^2-2} & \frac{1}{2}(\rho_1 - \rho_{d^2-1}) & 0 \\ 0 & \frac{1}{2}(\rho_1 - \rho_{d^2-1}) & \rho_{d^2} & 0 \\ 0 & 0 & 0 & \frac{1}{2}(\rho_1 + \rho_{d^2-1}) \end{pmatrix}. \quad (2.18)$$

Former includes searching of sufficient conditions for the coefficients ρ_i for one of the eigenvalues of $\rho_Q^{(b)}$ to be negative. Those eigenvalues are:

$$e_1 \equiv \frac{1}{2}(\rho_1 + \rho_{d^2-1}),$$

$$e_2^\pm \equiv \frac{1}{2}(\rho_{d^2-2} + \rho_{d^2}) \pm \sqrt{\frac{1}{4}(\rho_{d^2-2} + \rho_{d^2})^2 - \rho_{d^2-2} \cdot \rho_{d^2} + \frac{1}{4}(\rho_1 - \rho_{d^2-1})^2}.$$

e_2^- is the only eigenvalue which is not always non-negative. It becomes explicitly negative under the following condition:

$$\frac{1}{4}(\rho_{d^2-2} + \rho_{d^2})^2 - \rho_{d^2-2} \cdot \rho_{d^2} > 0 \iff \frac{1}{2}(\rho_1 - \rho_{d^2-1}) > \sqrt{\rho_{d^2-2} \cdot \rho_{d^2}}. \quad (2.19)$$

We consider that both terms of the first inequality are positive values, thus, the second term is a geometric mean, so it is always less than or equal to the arithmetic mean of the two coefficients.

Then, our condition can be expressed as:

$$\frac{\rho_1 - \rho_{d^2-1}}{2} > \frac{\rho_{d^2-2} + \rho_{d^2}}{2} \iff \rho_1 > \rho_{d^2-2} + \rho_{d^2-1} + \rho_{d^2}. \quad (2.20)$$

The sufficient condition for ρ_Q to be entangled can be further relaxed to $\rho_1 > 3\rho_{d^2-2}$.

Consider the trace of ρ :

$$\text{Tr}\rho = \sum_{i=1}^{d^2-2} \rho_i = 1 \Rightarrow 1 - \rho_1 = \sum_{i=2}^{d^2} \rho_i \geq \sum_{i=2}^{d^2-2} \rho_i. \quad (2.21)$$

The last sum is composed of $d^2 - 3$ terms, whose minimum is ρ_{d^2-2} ; so it must satisfy

$$1 - \rho_1 \geq \sum_{i=2}^{d^2-2} \rho_i \geq (d^2 - 3)\rho_{d^2-2} \Rightarrow \rho_{d^2-2} \leq \frac{1 - \rho_1}{d^2 - 3}. \quad (2.22)$$

Finally, we can express a sufficient condition for ρ_Q to be entangled as following

$$3 \frac{1 - \rho_1}{d^2 - 3} < \rho_1 \Leftrightarrow \rho_1 > \frac{3}{d^2}. \square \quad (2.23)$$

Obtained results allow construction of a factorization which parts the states into a maximally entangled state (the eigenstate of ρ_1 or ρ_{d^2-1}) and a separable state (the eigenstates ρ_{d^2-2} and ρ_{d^2}), i.e. to write a state in the form $\rho = \beta\mathcal{P} + (1 - \beta)\sigma$, where β is a real number, with $0 \leq \beta \leq 1$, \mathcal{P} is a projector to a maximally entangled pure state, and σ is state orthogonal to \mathcal{P} , i.e. $\langle \mathcal{P} | \sigma \rangle = 0$. Every state over a $d \times d$ dimensional Hilbert space which can be decomposed in above form has a maximum eigenvalue $\rho_{\max} = \{\max(\beta, 1 - \beta)\}$, and it is entangled if the condition $\rho_{\max} > \frac{1}{d}$, i.e., $\beta > \frac{1}{d}$, is satisfied.

Digression: For two $\frac{1}{2}$ -spins \vec{I}_a and \vec{I}_b , coupled by an interaction $\hat{H} = \frac{\omega}{\hbar} \vec{I}_a \cdot \vec{I}_b$, the

Hilbert space of particular system spanned by the four simultaneous eigenstates of $\hat{I}_{a,z}$

and $\hat{I}_{b,z}$ (where $\hat{I}_{a,z} |\uparrow\downarrow\rangle = \frac{\hbar}{2} |\uparrow\downarrow\rangle$ and $\hat{I}_{b,z} |\uparrow\downarrow\rangle = -\frac{\hbar}{2} |\uparrow\downarrow\rangle$), as follows:

$|\uparrow a\rangle \otimes |\downarrow b\rangle = |\uparrow a \uparrow b\rangle, |\uparrow a \downarrow b\rangle, |\downarrow a \uparrow b\rangle, |\downarrow a \downarrow b\rangle$, can be further organized in terms of 2×2 dimensional system of *singlet* and *triplet* states (which correspond to maximally entangled Bell states):

$$|\Psi^\pm\rangle = \frac{1}{\sqrt{2}} = (|\uparrow a \downarrow b\rangle \pm |\downarrow a \uparrow b\rangle), \quad |\Phi^\pm\rangle = \frac{1}{\sqrt{2}} = (|\uparrow a \uparrow b\rangle \pm |\downarrow a \downarrow b\rangle),$$

according to eq. (2.6), and we will use this later on.

2.5 The Qubit

The fundamental unit of classical information is represented via quantity called bit - the smallest piece of information which can take one of the two possible values $\{0, 1\}$. The corresponding unit of quantum information called the quantum bit or “qubit” represents an analog to a quantum system which has two levels, $|0\rangle$ and $|1\rangle$.

Consider an orthonormal basis for a two-dimensional vector space $\{|0\rangle, |1\rangle\}$ denoted in a two-dimensional Hilbert space. In this case the pure normalized qubit state can be expressed as

$$|\psi\rangle = a|0\rangle + b|1\rangle, \quad (2.24)$$

where a, b are complex numbers that satisfy $|a|^2 + |b|^2 = 1$ [37]. The simplest measurement of $|\psi\rangle$ yields 0 with probability $|a|^2$, and 1 with probability $|b|^2$.

If the normalization is written implicitly and the overall phase is neglected, eq. (5.1) can be expressed as

$$|\psi\rangle = \cos\left(\frac{\theta}{2}\right)|0\rangle + \sin\left(\frac{\theta}{2}\right)e^{i\varphi}|1\rangle, \quad (2.24a)$$

where the parameters θ and φ define a point on the surface of unit sphere in 3 dimensional space – the so called Bloch sphere⁵.

⁵Only the pure qubit state can be localized on the surface of the Bloch sphere, whereas the mixed state is located strictly inside of the Bloch sphere due to the positivity of the density

matrix: $\rho = \frac{1}{2}(1 + \vec{n} \cdot \vec{\sigma}) = \frac{1}{2} \begin{pmatrix} 1+n_3 & n_1 - in_2 \\ n_1 + in_2 & 1 - n_3 \end{pmatrix}$, $\vec{n} = (n_1, n_2, n_3)^T$, where the Bloch vector $n_i \in \mathbb{R}^3$ has to satisfy the condition: $|\vec{n}|^2 \leq 1$; if $|\vec{n}|^2 = 1$ that is a clear signature of existence of pure state (using the well known Pauli matrices: $\sigma_1 = \begin{pmatrix} 0 & 1 \\ 1 & 0 \end{pmatrix}$, $\sigma_2 = \begin{pmatrix} 0 & -i \\ i & 0 \end{pmatrix}$, $\sigma_3 = \begin{pmatrix} 1 & 0 \\ 0 & -1 \end{pmatrix}$ we can decompose in above form any arbitrary state expressed by a density matrix).

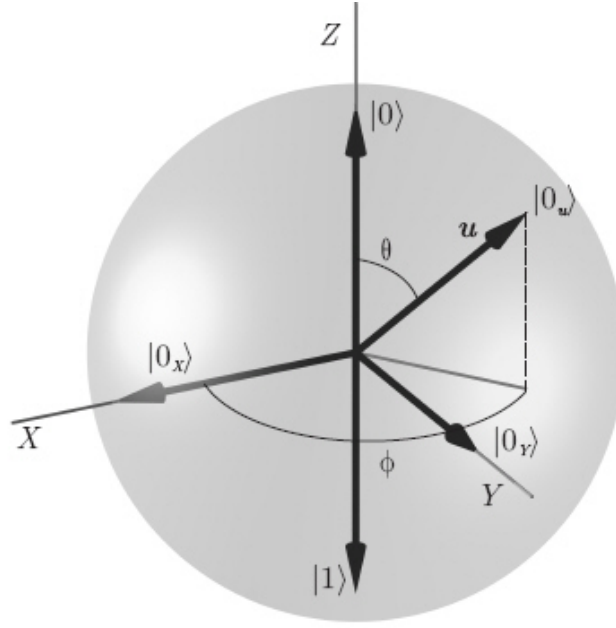


Figure 2: Qubit representation on the Bloch sphere, given by projection onto the $\{XYZ\}$ axes.

In addition to a qubit Bloch sphere representation, more precise information of the phase of quantum state can be obtained from measurement in different basis. For instance, if we consider in a standard basis the following quantum state

$$|\psi\rangle = \frac{1}{\sqrt{2}}|0\rangle + \frac{e^{i\theta}}{\sqrt{2}}|1\rangle, \quad (2.25)$$

the measurement outcome would be 0 with probability 1/2 and 1 with probability 1/2. In order to extract information about phase, let us consider a measurement in a basis other than the standard basis, for instance $\{|+\rangle, |-\rangle\}$, where

$$|+\rangle \equiv \frac{1}{\sqrt{2}}(|0\rangle + |1\rangle) \text{ and } |-\rangle \equiv \frac{1}{\sqrt{2}}(|0\rangle - |1\rangle). \quad (2.26)$$

We can elegantly estimate phase information of quantum state in the new basis by combining above relations into

$$|0\rangle = \frac{1}{\sqrt{2}}(|+\rangle + |-\rangle), |1\rangle = \frac{1}{\sqrt{2}}(|+\rangle - |-\rangle), \quad (2.27)$$

which results in following expression

$$\begin{aligned} |\psi\rangle &= \frac{1}{\sqrt{2}}|0\rangle + \frac{e^{i\theta}}{\sqrt{2}}|1\rangle \\ &= \frac{1}{2}(|+\rangle + |-\rangle) + \frac{e^{i\theta}}{2}(|+\rangle - |-\rangle) \\ &= \frac{1+e^{i\theta}}{2}|+\rangle + \frac{1-e^{i\theta}}{2}|-\rangle. \end{aligned} \tag{2.28}$$

From this point it is clear that information about the phase θ (recalling that $e^{i\theta} = \cos\theta + i\sin\theta$) can be extracted from the probability of measuring $|+\rangle$ and $|-\rangle$

state: $\frac{1}{4}((1+\cos\theta)^2 + \sin^2\theta) = \cos^2\left(\frac{\theta}{2}\right)$ and $\sin^2\left(\frac{\theta}{2}\right)$, respectively.

Chapter 3

Manipulation of semiconductor spin qubits

3.1 Introduction

The first spectroscopic technique used to demonstrate the implementation of quantum algorithms and construction of quantum gates [38-41], were nuclear magnetic resonance (NMR) techniques applied to nuclear spins in liquid state [42].

Further development of electron paramagnetic resonance (EPR) techniques [43] and electrical detection of magnetic resonance (EDMR) [44] have greatly facilitated the exploration toward electron spins with controllable exchange interactions in crystalline materials.

Thankfully to indispensable subatomic probes inside solids [45-47], the hybrid electron - nuclear spin qubits [48] are highlighted as the most prominent candidates referred to a robust quantum information resources for the next generation processor units and low dimensional memory elements [49, 50].

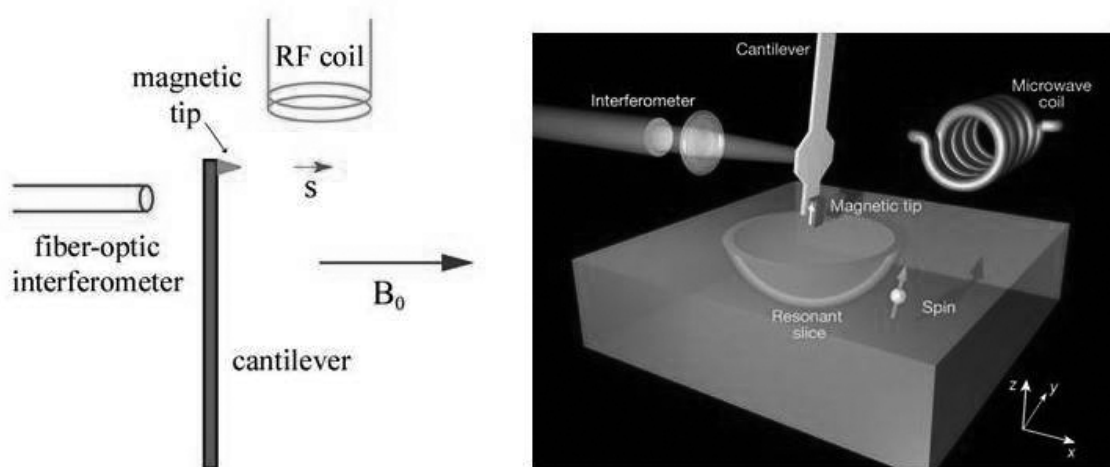


Figure 3.1: Single spin detection. Picture from [51].

Very recently, quantum entanglement between electron and nuclear spins has been experimentally confirmed [52] following the single electron spin detection [53] in solid state systems utilized in silicon. In this context, a featured approach to manipulate, measure and control nuclear spin correlation in a confined electronic system has been examined here as a special example of the spin-based solid state quantum computer.

In particular, following the [54] we will describe in this chapter the physical effect behind the implementation of alternating magnetic field which allows coherent control and coupling of a single electron and nuclear spin mediated via the hyperfine interaction inducing a specific superpositions, entanglement and transfer of quantum states encoded as a qubit of information between the two parties.

The key new feature of the hybrid spin system is the anisotropic hyperfine interaction, here exploited for universal coupling between highly polarized triplet electron spin state in the nuclear spin degrees of freedom using a controlled channeled proton beam as an actuator. The spin qubit is initialized in the nuclear spin space of the corresponding electron spin manifold. In this chapter it is discussed the underlying theory and background of the magnetic resonance and the hyperfine coupling effect utilized in this thesis.

3. 2 Manipulation of a single spin

3.2.1 Isolated spin in a static magnetic field

The motion of an isolated spin in a static magnetic field is presented by the Zeeman Hamiltonian as

$$\hat{\mathcal{H}} = -\hbar\gamma B_0 \hat{I}_z. \quad (3.1)$$

Using the commutation relations,

$$[\hat{I}_x, \hat{I}_y] = i\hat{I}_z,$$

$$\begin{aligned} [\hat{I}_y, \hat{I}_z] &= i\hat{I}_x, \\ [\hat{I}_z, \hat{I}_x] &= i\hat{I}_y, \end{aligned} \quad (3.2)$$

one can obtain the Heisenberg equations of motion as following:

$$\frac{d}{dt} \hat{I}_x = \frac{1}{i\hbar} [\hat{I}_x, \hat{\mathcal{H}}] = \gamma B_0 \hat{I}_y, \quad (3.3)$$

$$\frac{d}{dt} \hat{I}_y = \gamma B_0 \hat{I}_x, \quad (3.4)$$

$$\frac{d}{dt} \hat{I}_z = 0. \quad (3.5)$$

Straightforwardly from (3.3), (3.4) and (3.5), the operator torque equation is given by

$$\frac{d}{dt} \hat{I} = \vec{i} \frac{d\hat{I}_x}{dt} + \vec{j} \frac{d\hat{I}_y}{dt} + \vec{k} \frac{d\hat{I}_z}{dt} = \gamma B_0 \hat{I} \times \vec{k}, \quad (3.6)$$

with its equivalent:

$$\frac{d}{dt} \hat{\mu} = \gamma B_0 \hat{\mu} \times \vec{k}, \quad \hat{\mu} = \gamma \hbar \hat{I}, \quad (3.7)$$

where in both case $\vec{i}, \vec{j}, \vec{k}$ are the unit vectors along x, y, z directions and it is imposed condition that the spin precesses along a static magnetic field with right-handed circulation for $\gamma < 0$ or left-handed circulation for $\gamma > 0$. $\hat{\mu}$ is the magnetic moment operator.

3.2.2 Rotating reference frame

Assuming that an imaginary frame $(\vec{i}, \vec{j}, \vec{k})$ rotates along z-axis (or \vec{k}) with an angular frequency $\vec{\Omega}$, the rotational dynamics can be described by the following set of equations

$$\frac{d}{dt} \vec{i} = \vec{\Omega} \times \vec{i}, \quad (3.8a)$$

$$\frac{d}{dt} \vec{j} = \vec{\Omega} \times \vec{j}, \quad (3.8b)$$

$$\frac{d}{dt} \vec{k} = \vec{\Omega} \times \vec{k}. \quad (3.8c)$$

and by a dynamical variable $\vec{F} = \vec{i} F_x + \vec{j} F_y + \vec{k} F_z$, that follows the relation

$$\begin{aligned} \frac{d}{dt} \vec{F} &= \vec{i} \frac{F_x}{dt} + \vec{j} \frac{F_y}{dt} + \vec{k} \frac{F_z}{dt} + F_x \frac{d\vec{i}}{dt} + F_y \frac{d\vec{j}}{dt} + F_z \frac{d\vec{k}}{dt} \\ &= \frac{\partial \vec{F}}{\partial t} + \vec{\Omega} \times \vec{F}, \end{aligned} \quad (3.9)$$

where $\frac{d\vec{F}}{dt}$ and $\frac{\partial \vec{F}}{\partial t}$ denote the time rates of change of \vec{F} with respect to a (fixed)

laboratory frame and (rotating) imaginary frame $(\vec{i}, \vec{j}, \vec{k})$, respectively.

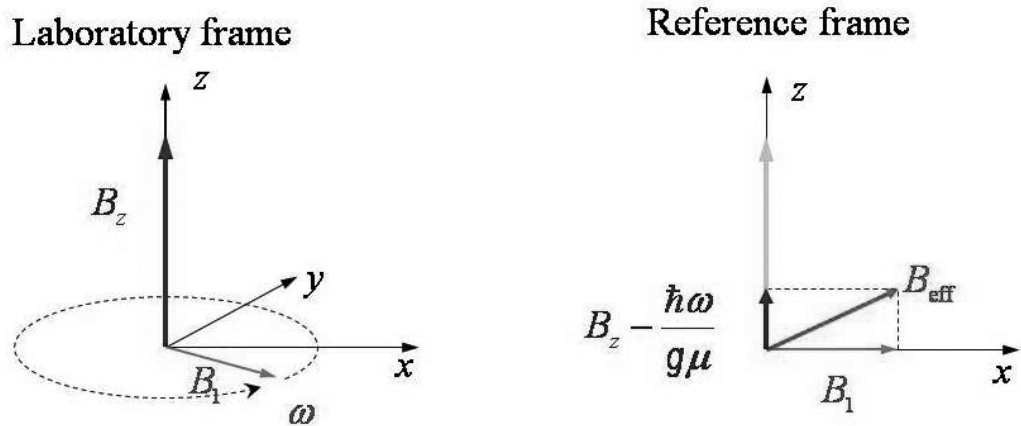


Figure 3.2: Schematic representation of the laboratory and reference frame (see text).

Upon substitution of $\vec{F} = \hat{\mu}$, using the eq. $\frac{d}{dt}\hat{\mu} = \gamma B_0 \hat{\mu} \times \vec{k}$, we obtained

$$\frac{d}{dt}\hat{\mu} = \frac{\partial \hat{\mu}}{\partial t} + \vec{\Omega} \times \hat{\mu} = \gamma B_0 \hat{\mu} \times \vec{k}. \quad (3.10)$$

Following above results the Heisenberg equation of motion for $\hat{\mu}$ in a rotating frame is:

$$\frac{\partial \hat{\mu}}{\partial t} = \hat{\mu} \times (\gamma B_0 \vec{k} + \vec{\Omega}) = \gamma B_{\text{eff}} \hat{\mu} \times \vec{k}, \quad (3.11)$$

where $B_{\text{eff}} \vec{k} = B_0 \vec{k} + \frac{\vec{\Omega}}{\gamma}$ represents an effective field. If the imaginary frame rotates with an angular frequency $\vec{\Omega} = -\gamma B_0 \vec{k}$ the effective field B_{eff} disappears and the spin remains fixed, $\frac{\partial \hat{\mu}}{\partial t} = 0$, in this rotating frame.

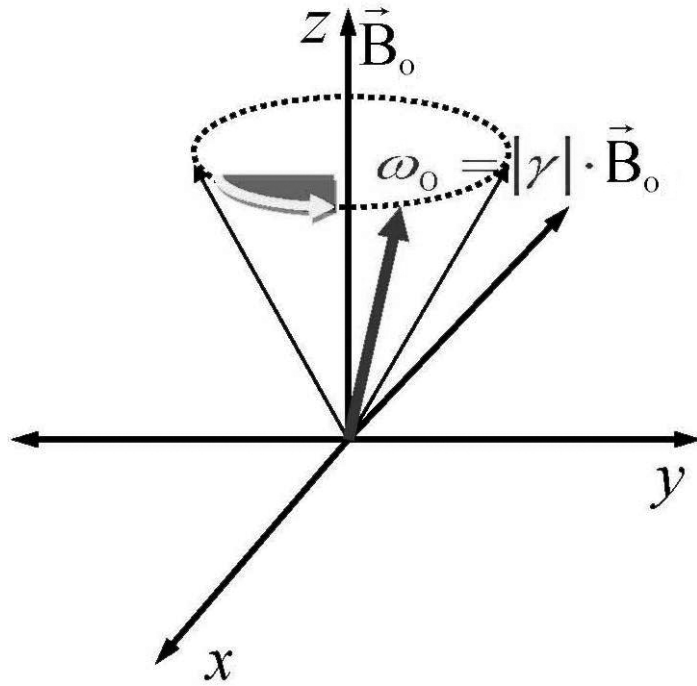


Figure 3.3: Larmor frequency. Schematic representation of the precession of the magnetic moment under applied external magnetic field.

Thus, the spin $\hat{\mu}$ rotates along a static field with an angular frequency $\vec{\Omega} = -\gamma B_0 \vec{k}$ in the laboratory frame. This oscillation frequency is called a Larmor frequency, $\omega_0 = |\gamma| B_0$.

3.3 Spin precession and magnetic resonance condition

If we consider a spin in dc magnetic field, B_0 along z axis, a magnetic interaction Hamiltonian is

$$\hat{\mathcal{H}} = -\hat{\mu} \cdot \vec{k} B_0 = -\hbar\gamma B_0 \hat{I}_z, \quad (3.12)$$

where, \vec{k} is a unit vector along z -axis.

A magnetic moment of electron (nucleus) is given by

$$\hat{\mu} = \hbar\gamma \hat{I}, \quad (3.13)$$

where γ is a gyromagnetic ratio and \hat{I} is a dimensionless angular momentum operator.

As the squared total angular momentum \hat{I}^2 and the z -component of the total angular momentum \hat{I}_z commute, $[\hat{I}^2, \hat{I}_z] = 0$, a simultaneous eigenstate of \hat{I}^2 and \hat{I}_z exists and can be expressed via

$$\hat{I}^2 |I, m\rangle = I(I+1) |I, m\rangle, \quad (3.14)$$

$$\hat{I}_z |I, m\rangle = m |I, m\rangle, \quad (3.15)$$

with eigenvalues $I = \frac{1}{2}, 1, \frac{3}{2}, \dots$ and $m = I, I-1, \dots, -1$, respectively. The eigenenergies corresponding to (3.2) for such eigenstates are given by

$$E = -\hbar\gamma B_0 m. \quad (3.16)$$

In addition to the static field B_0 , introduce of the superimposing alternating magnetic field, $B_1 \cos \omega t$, along a perpendicular direction, for instance x -axis, is governed by the new Hamiltonian

$$B_1 \cos \omega t \hat{I}_x \hat{\mathcal{H}}_I = -\hbar\gamma. \quad (3.17)$$

The x -component of the angular momentum operator, \hat{I}_x , is expressed as

$$\hat{I}_x = \frac{1}{2}(\hat{I}_+ + \hat{I}_-), \quad (3.18)$$

where \hat{I}_+ and \hat{I}_- are the raising and the lowering operator respectively, referring to the following recursion relations:

$$\hat{I}_+ |I, m\rangle = \sqrt{I(I+1) - m(m+1)} |I, m+1\rangle, \quad (3.19)$$

$$\hat{I}_- |I, m\rangle = \sqrt{I(I+1) - m(m-1)} |I, m-1\rangle. \quad (3.20)$$

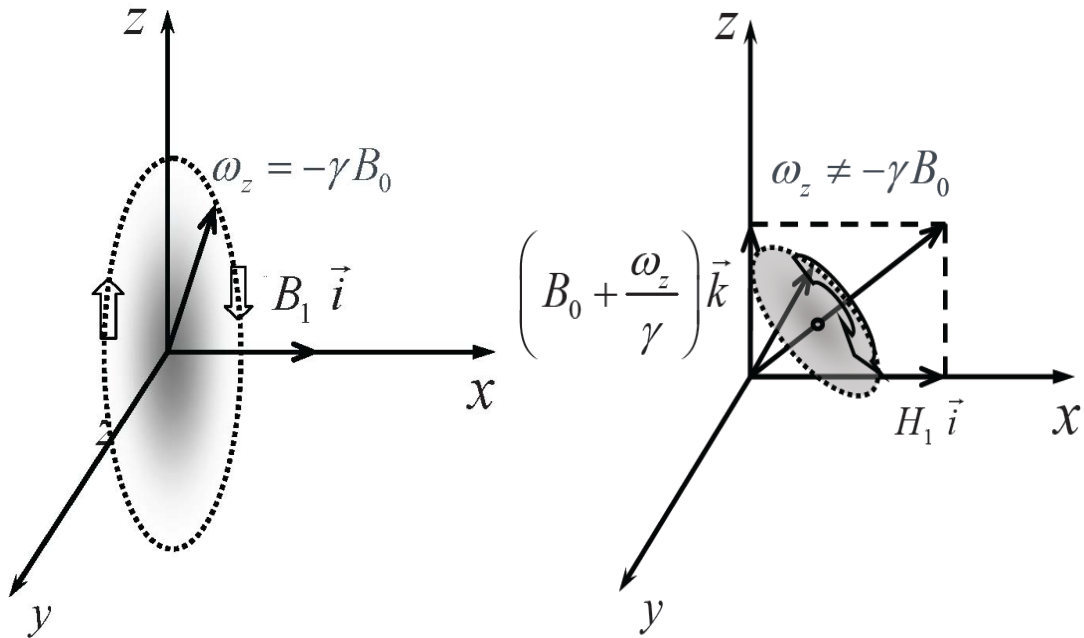


Figure 3.5: Spin precession at resonance condition, $\omega_z = -\gamma B_0$, $\gamma > 0$, left, and off-resonance condition $\omega_z \neq -\gamma B_0$, $\gamma > 0$, right.

If the frequency ω is close to the resonance with the Zeeman splitting,

$\omega \cong |\gamma| B_0$, the transverse magnetic field, $B_1 \cos \omega t$, allows change of the eigenvalue m by ± 1 . In order to comply with energy conservation law this process must be followed with the absorption or emission of a single photon at frequency ω .

3.4 Interaction between two electrons

If we consider a system of two electrons, according to Pauli's exclusion principle the spin wave function is symmetric if the two electron spins are parallel, i.e. in the triplet $S = 1$ state.

$$S = 1 \begin{cases} \beta_1^+ \beta_2^+ \equiv |1, +1\rangle \\ \frac{1}{\sqrt{2}} [\beta_1^+ \beta_2^- + \beta_1^- \beta_2^+] \equiv |1, 0\rangle \\ \beta_1^- \beta_2^- \equiv |1, -1\rangle, \end{cases} \quad (3.21)$$

where: +, -, correspond to up and down spin state of the electrons, respectively.

Conversely, the wave function, in coordination space, is antisymmetric when the two electron spins are antiparallel, i.e., when the overall spin is $S = 0$

$$S = 0 \left\{ \frac{1}{\sqrt{2}} [\beta_1^+ \beta_2^- - \beta_1^- \beta_2^+] \equiv |0, 0\rangle. \right. \quad (3.22)$$

The splitting in energy into singlet and triplet states is governed by the electron-exchange interaction as

$$\mathcal{H}_{exch} = \sum_{i,j} J_{i,j} S_{1i} \cdot S_{2j}, \quad (3.23)$$

where S_{1i} and S_{2j} are electron spin operators for electron 1 and 2, defined by spatial coordinates ($i, j = x, y, z$).

The main part of the exchange-energy operator is

$$(\mathcal{H}_{exch})_{iso} = J_0 S_1 \cdot S_2, \quad (3.24)$$

where $J_0 = \frac{\text{Tr}(J)}{3}$ is the isotropic-exchange coupling constant.

In the first approximation J_0 is presented via the exchange integral

$$J_0 = -2 \langle \psi_1(r_1) \psi_2(r_2) | \frac{e^2}{4\pi\epsilon_0 r} | \psi_1(r_2) \psi_2(r_1) \rangle, \quad (3.25)$$

where $\psi_1(r_1)$ and $\psi_2(r_2)$ denote the space wave function of two electrons in position space, r is the distance between two electrons and ϵ_0 is vacuum permittivity. The singlet and triplet states are separated by the energy modulus equal to $|J_0|$, where the sign of J_0 determines which state is lower scaled: the singlet or the triplet state.

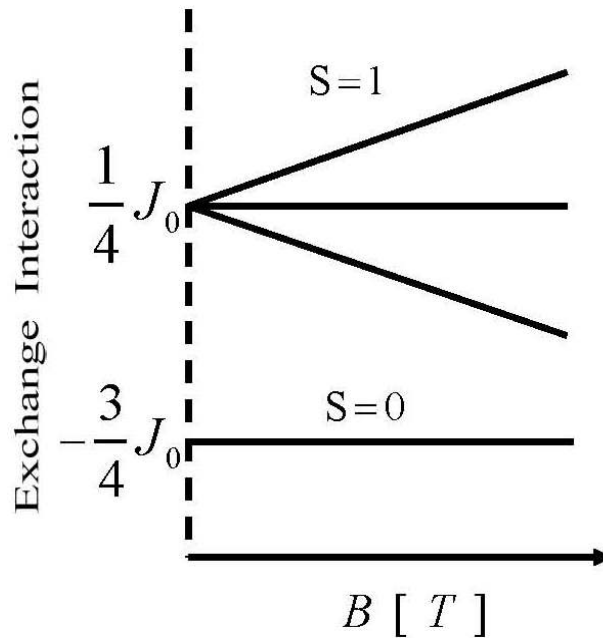


Figure 3.4: Exchange interaction between spins of two electron system.

In zero magnetic field the anisotropic magnetic dipole - dipole interaction lifts the three-fold degeneracy of the triplet state.

In case of two electrons the electron spin-spin dipolar interaction is given by

$$\mathcal{H}_{SS} = \hbar^2 \gamma_e^2 \left[\frac{\mathbf{S}_1 \cdot \mathbf{S}_2}{r^3} - \frac{3(\mathbf{S}_1 \cdot \mathbf{r})(\mathbf{S}_2 \cdot \mathbf{r})}{r^5} \right]. \quad (3.26)$$

Applying the total spin operator, $\mathbf{S} = \mathbf{S}_1 + \mathbf{S}_2$, with identity $r^2 = x^2 + y^2 + z^2$ on the former eq. gives

$$\mathcal{H}_{\text{SS}} = \frac{\hbar^2 \gamma_e^2}{2} \begin{bmatrix} S_x & S_y & S_z \end{bmatrix} \cdot \begin{bmatrix} \left\langle \frac{r^2 - 3x^2}{r^5} \right\rangle & \left\langle \frac{-3xy}{r^5} \right\rangle & \left\langle \frac{-3xz}{r^5} \right\rangle \\ \left\langle \frac{-3yx}{r^5} \right\rangle & \left\langle \frac{r^2 - 3y^2}{r^5} \right\rangle & \left\langle \frac{-3yz}{r^5} \right\rangle \\ \left\langle \frac{-3zx}{r^5} \right\rangle & \left\langle \frac{-3zy}{r^5} \right\rangle & \left\langle \frac{r^2 - 3z^2}{r^5} \right\rangle \end{bmatrix} \cdot \begin{bmatrix} S_x \\ S_y \\ S_z \end{bmatrix}. \quad (3.27)$$

The angular brackets denote averaging over the electron spatial wave function.

The Hamiltonian can be rewritten as $\mathcal{H}_{\text{SS}} = \mathbf{S} \cdot \mathbf{D} \cdot \mathbf{S}$, where \mathbf{D} represents the spin spin-spin dipolar coupling interaction tensor with $\text{Tr}(\mathbf{D}) = 0$.

After applying the diagonalization former eq. can be represented in the principle axis system (X,Y,Z) as

$$\mathcal{H}_{\text{SS}} = D_X S_X^2 + D_Y S_Y^2 + D_Z S_Z^2. \quad (3.28)$$

Introducing the zero field parameters: $D = \frac{3}{2} D_Z$ and $E = \frac{1}{2} (D_X - D_Y)$, the Hamiltonian is further expressed as

$$\mathcal{H}_{\text{SS}} = D \left(S_Z^2 - \frac{1}{2} S^2 \right) + E (S_X^2 + S_Y^2). \quad (3.29)$$

Finally, applying the external magnetic field the total Hamiltonian of the triplet state is

$$\mathcal{H}_e = \gamma_e \hbar \mathbf{B} \cdot \mathbf{S} + D \left(S_Z^2 - \frac{1}{2} S^2 \right) + E (S_X^2 + S_Y^2). \quad (3.30)$$

In the limit $\mathbf{B} \rightarrow 0$, with $\vec{\mathbf{B}}$ parallel to the z-axis the zero field, triplet eigenfunctions are

$$|T_X\rangle = \frac{1}{\sqrt{2}} |-1\rangle - |+1\rangle, \quad (3.31a)$$

$$|T_Y\rangle = \frac{i}{\sqrt{2}}|-1\rangle + | +1\rangle, \quad (3.31b)$$

$$|T_Z\rangle = |0\rangle. \quad (3.31c)$$

3.5 A magnetic coupling between nuclear spin and electron spin

For a nucleus with a magnetic moment μ_n at $\vec{r} = 0$ and a finite radius ρ_0 , there exist two kinds of magnetic fields: uniform internal field B_i inside the nucleus and external dipole field B_e outside the nucleus, which cancel with each other out as a result of magnetic flux continuity as following:

$$\phi_{int}(\rho_0) + \phi_{ext}(\rho_0) = 0. \quad (3.32)$$

The internal flux is $\phi_{int}(\rho_0) = \pi\rho_0^2 B_i$, while the external flux is

$$\phi_{ext}(\rho_0) = 2\pi \int_{\rho_0}^{\infty} \left(-\frac{\mu_n}{r^3} \right) r dr = -\mu_n \frac{2\pi}{\rho_0}. \quad (3.33)$$

As a result, the internal field can be expressed as

$$B_i = \frac{2\mu_n}{\rho_0^2}. \quad (3.34)$$

3.5.1 Isotropic and anisotropic hyperfine interaction

Assuming that electron wavefunction and a nuclear wavefunction overlap, the effective nuclear magnetic field which an electron spin feels is

$$B_z = B_i \left(\frac{4}{3} \pi \rho_0^3 \right) |u_e(0)|^2, \quad (3.35)$$

where $|u_e(0)|^2$ is the electron density at $\vec{r} = 0$ and $\frac{4}{3} \pi \rho_0^3$ is the probability of finding an electron inside the nucleus. In particular, when the electron wavefunction occupies

isotropically much larger space compared to the nuclear wavefunction, the magnetic interaction between the nucleus and the electron outside the nucleus is identically zero, as for an s -wave symmetry electron wavefunction. In particular, the space integration cancels out due to the continuity of magnetic flux. Thus, from (3.34) and (3.35), the effective interaction Hamiltonian is given by:

$$\hat{H}_{eff} = -\mu_e B_z = \frac{8\pi}{3} \hat{\mu}_e \cdot \hat{\mu}_n |u_e(0)|^2 = \frac{8\pi}{3} \gamma_e \gamma_n \hbar^2 \hat{I} \cdot \hat{S} |u_e(0)|^2, \quad (3.36)$$

where $\hat{\mu}_e = -\hbar\gamma_e \hat{S}$ and $\hat{\mu}_n = \hbar\gamma_n \hat{I}$. The Hamiltonian (3.36) represents a Fermi contact interaction, establishable only for the case when the electron and nucleus wavefunctions overlap. Conversely, when the overlapping does not exist, or the electron wavefunction is a p -wave, d -wave or other symmetries with non-zero angular momentum, the space integration for an external dipole field B_e is non-zero, giving the anisotropic hyperfine interaction Hamiltonian [55]:

$$\hat{H}_{eff} = \frac{\hat{\mu}_e \cdot \hat{\mu}_n}{r^3} - \frac{3(\hat{\mu}_e \cdot \vec{r})(\hat{\mu}_n \cdot \vec{r})}{r^5} = \frac{\gamma_e \gamma_n}{r^3} \hbar^2 \left[\frac{3(\hat{S} \cdot \vec{r})(\hat{I} \cdot \vec{r})}{r^2} - \hat{S} \cdot \hat{I} \right], \quad (3.37)$$

with \vec{r} as the vector connecting the electron and the nuclear spin.

Now, the Hamiltonian is characterized by the terms $-\frac{\gamma_e \gamma_n}{r^3} \hbar^2 \hat{S}_x \hat{I}_x$ and $\frac{\gamma_e \gamma_n}{r^5} \hbar^2 \hat{S}_x \hat{I}_y xy$.

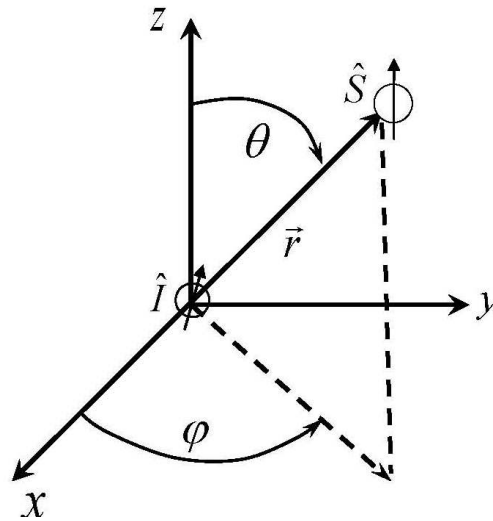


Figure 3.5: Schematic view of the magnetic coupling between nuclear and electron spin represented in polar coordinate system (see text).

If $\hat{I}_x = \frac{1}{2}(\hat{I}_+ + \hat{I}_-)$ and $\hat{I}_y = \frac{1}{2i}(\hat{I}_+ - \hat{I}_-)$ and similar expressions for \hat{S}_x and \hat{S}_y are used in (3.37) and we introduce a polar coordinate (r, θ, φ) , we have the new expression:

$$\hat{H}_{eff} = -\frac{\gamma_e \gamma_n}{r^3} \hbar^2 (A + B + C + D + E + F), \text{ where}$$

$$A = \hat{S}_z \hat{I}_z (1 - 3 \cos^2 \theta), \quad (3.38a)$$

$$B = -\frac{1}{4} (\hat{S}_+ \hat{I}_- + \hat{S}_- \hat{I}_+) (1 - 3 \cos^2 \theta), \quad (3.38b)$$

$$C = -\frac{3}{2} (\hat{S}_+ \hat{I}_z + \hat{S}_z \hat{I}_+) \sin \theta \cos \theta e^{-i\phi}, \quad (3.38c)$$

$$D = -\frac{3}{2} (\hat{S}_- \hat{I}_z + \hat{S}_z \hat{I}_-) \sin \theta \cos \theta e^{-i\phi}, \quad (3.38d)$$

$$E = -\frac{3}{4} \hat{S}_+ \hat{I}_+ \sin^2 \theta e^{-2i\phi}, \quad (3.38e)$$

$$F = -\frac{3}{4} \hat{S}_- \hat{I}_- \sin^2 \theta e^{2i\phi}. \quad (3.38f)$$

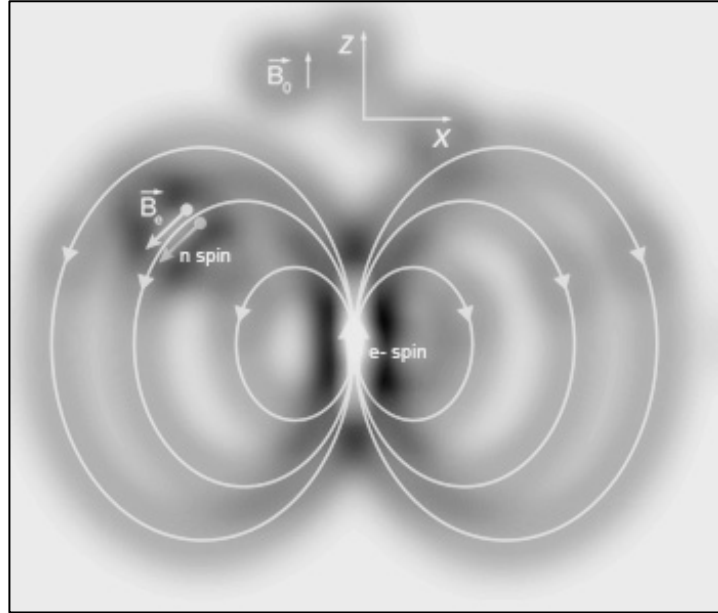


Figure 3.6: External dipole field \vec{B}_e outside the nucleus spin, created by the strong static magnetic field \vec{B}_0 in the electron spin manifold, a schematic representation.

For the system where the spin density of the unpaired electron in orbitals with angular momentum $l \neq 0$ generates a purely anisotropic coupling, this “active” part of the hyperfine interaction can be described by a dipolar coupling of the magnetic moment of the electron to a nucleus, see figure 3.5.

In the principal axis system the dipolar (anisotropic) hyperfine coupling Hamiltonian is given by

$$\mathbf{T} = \frac{\mu_0 \gamma_e \gamma_n}{4\pi r^3} \begin{pmatrix} -1 & 0 & 0 \\ 0 & -1 & 0 \\ 0 & 0 & 2 \end{pmatrix} = \begin{pmatrix} -T & 0 & 0 \\ 0 & -T & 0 \\ 0 & 0 & 2T \end{pmatrix}. \quad (3.39)$$

As a result, the complete hyperfine tensor \mathbf{A} given by:

$$\begin{aligned} \hat{H}_{\text{HF}} &= \hat{H}_{\text{HF}}^{\text{iso}} + \hat{H}_{\text{HF}}^{\text{aniso}} = \vec{S} \mathbf{A} \vec{I} \\ &= a_{\text{iso}} \vec{S} \vec{I} + \vec{S} \mathbf{T} \vec{I}, \end{aligned} \quad (3.40)$$

can be rewritten as a sum of the isotropic and the anisotropic part eq. (3.39):

$$\mathbf{A} = \begin{pmatrix} A_{xx} & 0 & 0 \\ 0 & A_{yy} & 0 \\ 0 & 0 & A_{zz} \end{pmatrix} = \begin{pmatrix} a_{\text{iso}} - T & 0 & 0 \\ 0 & a_{\text{iso}} - T & 0 \\ 0 & 0 & a_{\text{iso}} + 2T \end{pmatrix}. \quad (3.41)$$

In general case of an axially symmetric hyperfine tensor ($A_{xx} = A_{yy}$) the principal values are $[A_{xx}, A_{yy}, A_{zz}] = [A_{\perp}, A_{\perp}, A_{\parallel}]$, where A_{\parallel} denotes the component of the hyperfine tensor when the magnetic field is parallel to the vector connecting the two dipoles and A_{\perp} denotes the component when the field is perpendicular to this vector.

The anisotropic component can be extracted from the trace of the hyperfine tensor \mathbf{A} as:

$$a_{\text{iso}} = \frac{1}{3} \text{Tr}(\mathbf{A}). \quad (3.42)$$

Under the circumstances of a strong static field \mathbf{B}_0 along z-axis, the Zeeman Hamiltonian:

$$\hat{H}_Z = \gamma_n \hbar H_0 \hat{I}_z + \gamma_e \hbar H_0 \hat{S}_z, \quad (3.43)$$

has dominant influence over the hyperfine interaction Hamiltonian.

In this case we can solve the Zeeman problem first and then treat the hyperfine coupling as a perturbation. The eigenenergy of the unperturbed state is

$$E_z = -\gamma_n \hbar B_0 m_I + \gamma_e \hbar B_0 m_s, \quad (3.44)$$

where m_I and m_s are the eigenvalues of \hat{I}_z and \hat{S}_z . The energy level diagram for $m_I = \pm \frac{1}{2}$ and $m_s = \pm \frac{1}{2}$, in figure 3.7, shows how the matrix elements A to F, given in eq (3.38), connect these Zeeman eigenstates.

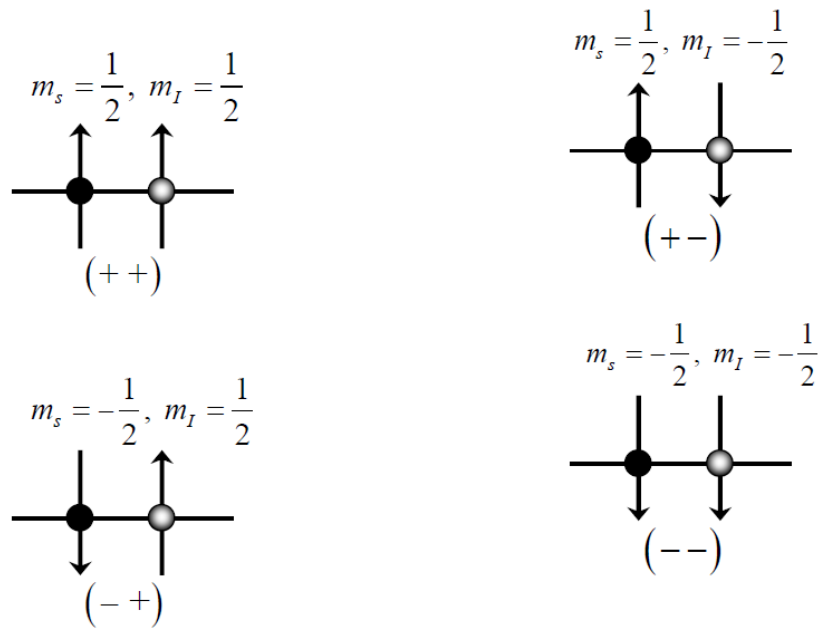


Figure 3.7: Schematic representation of the Zeeman energy eigenstate levels for a nuclear and electron spin ($m_I = \pm \frac{1}{2}, m_s = \pm \frac{1}{2}$).

3.6 Electron – nuclear spin interaction

For the following discussion a coupled spin system $\left(S = \frac{1}{2}, I = \frac{1}{2}\right)$ is assumed.

3.6.1 Static Hamiltonian

For an electron ($S = \frac{1}{2}$) coupled to a nucleus ($I = \frac{1}{2}$) the static Hamiltonian essentially reduces to a sum of electron Zeeman, nuclear Zeeman and hyperfine interaction term, respectively:

$$\hat{H}_0 = \hat{H}_{\text{EZ}} + \hat{H}_{\text{NZ}} + \hat{H}_{\text{HF}} = \omega_S \vec{\hat{S}} - \omega_I \vec{\hat{I}} + \vec{\hat{S}} \mathbf{A} \vec{\hat{I}}. \quad (3.45)$$

If we assume the high-field approximation all terms including the spin operators \hat{S}_x and \hat{S}_y can be neglected, consequently the relation (3.45) is further reduced to

$$\hat{H}_0 = \omega_S \hat{S}_Z - \omega_I \hat{I}_Z + A \hat{S}_Z \hat{I}_Z + B_X \hat{S}_Z \hat{I}_X + B_Y \hat{S}_Z \hat{I}_Y, \quad (3.46)$$

with $A = A_{ZZ}$, $B_X = A_{ZX}$, and $B_Y = A_{ZY}$ denoting the secular and pseudo-secular parts of the hyperfine coupling, respectively. Using the $U_1 = e^{-i\phi \hat{I}_Z}$, the hyperfine part of the Hamiltonian \hat{H}_0 can be further transformed in a unitary transformation

$$\begin{aligned} U_1 \cdot \hat{H}_{\text{HF}} \cdot U_1^{-1} &= U_1 \left(A \hat{S}_Z \hat{I}_Z + B_X \hat{S}_Z \hat{I}_X + B_Y \hat{S}_Z \hat{I}_Y \right) U_1^{-1} \\ &= A \hat{S}_Z \hat{I}_Z + U_1 \left(B_X \hat{S}_Z \hat{I}_X + B_Y \hat{S}_Z \hat{I}_Y \right) U_1^{-1} \\ &= A \hat{S}_Z \hat{I}_Z + B \hat{S}_Z \hat{I}_X. \end{aligned} \quad (3.47)$$

In combination to eq. (3.46), former relation gives the final reduction of the static Hamiltonian:

$$\hat{H}_0 = \omega_S \hat{S}_Z - \omega_I \hat{I}_Z + A \hat{S}_Z \hat{I}_Z + B \hat{S}_Z \hat{I}_X, \quad (3.48)$$

where $B = \left(B_X^2 + B_Y^2\right)^{\frac{1}{2}}$, $\phi = \arctan\left(-\frac{B_Y}{B_X}\right)$ an angle which defines a rotation of the laboratory frame around the z -axis by \hat{I}_Z .

The matrix representation of \hat{H}_0 in case of the eigenbasis defined by $|\alpha, \beta\rangle, |\alpha, \alpha\rangle, |\beta, \beta\rangle, |\beta, \alpha\rangle$ or, $|+, -\rangle, |+, +\rangle, |-, -\rangle, |-, +\rangle$ is given by:

$$\hat{H}_0 = \begin{pmatrix} \frac{\omega_s}{2} - \frac{\omega_l}{2} + \frac{A}{4} & +\frac{B}{4} & 0 & 0 \\ +\frac{B}{4} & \frac{\omega_s}{2} + \frac{\omega_l}{2} - \frac{A}{4} & 0 & 0 \\ 0 & 0 & -\frac{\omega_s}{2} - \frac{\omega_l}{2} - \frac{A}{4} & -\frac{B}{4} \\ 0 & 0 & -\frac{B}{4} & -\frac{\omega_s}{2} + \frac{\omega_l}{2} + \frac{A}{4} \end{pmatrix}. \quad (3.49)$$

The anisotropic hyperfine interaction consequences the non-diagonal form of the Hamiltonian.

3.6.2 Exact diagonalization of the static Hamiltonian

Because the Hamiltonian is given by a 2×2 block-diagonal form, the two subspaces can be separated and diagonalized using the polarization operators \hat{S}^α and \hat{S}^β :

$$\hat{S}^\alpha = \frac{1}{2}\mathbb{E} + \hat{S}_z = \begin{pmatrix} 1 & 0 \\ 0 & 0 \end{pmatrix}, \hat{S}^\beta = \frac{1}{2}\mathbb{E} - \hat{S}_z = \begin{pmatrix} 0 & 0 \\ 0 & 1 \end{pmatrix}, \quad (3.50)$$

where $(\hat{S}^\alpha + \hat{S}^\beta) = \mathbb{E}$ and $\frac{1}{2}(\hat{S}^\alpha - \hat{S}^\beta) = \hat{S}_z$.

Combining the relations (3.7) and (3.8) the Hamiltonian \hat{H}_0 reads

$$\begin{aligned} \hat{H}_0 &= \omega_s \hat{S}_z - \omega_l \hat{I}_z + \frac{1}{2}A(\hat{S}^\alpha - \hat{S}^\beta)\hat{I}_z + \frac{1}{2}B(\hat{S}^\alpha - \hat{S}^\beta)\hat{I}_x \\ &= \omega_s \hat{S}_z - \omega_l (\hat{S}^\alpha + \hat{S}^\beta)\hat{I}_z \\ &\quad + \frac{1}{2}A(\hat{S}^\alpha - \hat{S}^\beta)\hat{I}_z + \frac{1}{2}B(\hat{S}^\alpha - \hat{S}^\beta)\hat{I}_x. \end{aligned} \quad (3.51)$$

This relation can be further expressed as:

$$\begin{aligned}
\hat{H}_0 &= \omega_s \hat{S}_Z - \omega_l \hat{S}^\alpha \hat{I}_Z - \omega_l \hat{S}^\beta \hat{I}_Z \\
&\quad + \frac{A}{2} \hat{S}^\alpha \hat{I}_Z - \frac{A}{2} \hat{S}^\beta \hat{I}_Z + \frac{B}{2} \hat{S}^\alpha \hat{I}_X - \frac{B}{2} \hat{S}^\beta \hat{I}_X \\
&= \omega_s \hat{S}_Z + \left(-\omega_l + \frac{A}{2} \right) \hat{S}^\alpha \hat{I}_Z + \left(-\omega_l - \frac{A}{2} \right) \hat{S}^\beta \hat{I}_Z \\
&\quad + \frac{B}{2} \hat{S}^\alpha \hat{I}_X - \frac{B}{2} \hat{S}^\beta \hat{I}_X,
\end{aligned} \tag{3.52}$$

$$\hat{H}_0 = \omega_s \hat{S}_Z - \underbrace{\left(\omega_l - \frac{A}{2} \right) \hat{S}^\alpha \hat{I}_Z + \frac{B}{2} \hat{S}^\alpha \hat{I}_X}_{\hat{H}_0^\alpha} - \underbrace{\left(\omega_l + \frac{A}{2} \right) \hat{S}^\beta \hat{I}_Z - \frac{B}{2} \hat{S}^\beta \hat{I}_X}_{\hat{H}_0^\beta} \Rightarrow \tag{3.53}$$

$$\hat{H}_0 = \omega_s \hat{S}_Z - \hat{H}_0^\alpha - \hat{H}_0^\beta.$$

The anisotropic part of the hyperfine coupling obtained in the final relation for \hat{H}_0 describes the transition moment and the level of mixing between allowed and forbidden state transitions.

Former equation can be diagonalized by applying the commutator:

$$\begin{aligned}
U_2 &= e^{-i \left(\eta_\alpha \hat{S}^\alpha \hat{I}_Y + \eta_\beta \hat{S}^\beta \hat{I}_Y \right)} \\
&= \underbrace{e^{-i \left(\eta_\alpha \hat{S}^\alpha \hat{I}_Y \right)}}_{U^\alpha} \underbrace{e^{i \left(\eta_\beta \hat{S}^\beta \hat{I}_Y \right)}}_{U^\beta} \\
&= U_2^\alpha \cdot U_2^\beta,
\end{aligned} \tag{3.54}$$

where the subspaces \hat{H}_0^α and H_0^β can be found with

$$\left[\hat{S}^\alpha \hat{I}_Y, \hat{S}^\alpha \hat{I}_Z \right] = -i \hat{S}^\alpha \hat{I}_X, \tag{3.55a}$$

$$\left[\hat{S}^\beta \hat{I}_Y, \hat{S}^\beta \hat{I}_Z \right] = -i \hat{S}^\beta \hat{I}_X. \tag{3.55b}$$

In the first transformation, $\hat{H}_0^\alpha \xrightarrow{U_2^\alpha} \hat{H}_0^{D(\alpha)}$, we get the following diagonal and off-diagonal elements

$$\begin{aligned}
\left(\omega_l - \frac{A}{2}\right) \hat{S}^\alpha \hat{I}_Z &\xrightarrow{\eta_\alpha \hat{S}^\alpha \hat{I}_Y} \left(\omega_l - \frac{A}{2}\right) \hat{S}^\alpha \hat{I}_Z \cos(\eta_\alpha) \\
&\quad - i \left[\hat{S}^\alpha \hat{I}_Y, \hat{S}^\alpha \hat{I}_Z \right] \left(\omega_l - \frac{A}{2}\right) \sin(\eta_\alpha) \\
&= \left(\omega_l - \frac{A}{2}\right) \hat{S}^\alpha \hat{I}_Z \cos(\eta_\alpha) \\
&\quad - i \left(-i \hat{S}^\alpha \hat{I}_X\right) \left(\omega_l - \frac{A}{2}\right) \sin(\eta_\alpha) \\
&= \underbrace{\left(\omega_l - \frac{A}{2}\right) \hat{S}^\alpha \hat{I}_Z \cos(\eta_\alpha)}_{\text{diagonal}} \\
&\quad - \underbrace{\hat{S}^\alpha \hat{I}_X \left(\omega_l - \frac{A}{2}\right) \sin(\eta_\alpha)}_{\text{off-diagonal}}, \tag{3.56}
\end{aligned}$$

and likewise

$$\begin{aligned}
\frac{B}{2} \hat{S}^\alpha \hat{I}_X &\xrightarrow{\eta_\alpha \hat{S}^\alpha \hat{I}_Y} \frac{B}{2} \hat{S}^\alpha \hat{I}_X \cos(\eta_\alpha) - i \left[\hat{S}^\alpha \hat{I}_Y, \hat{S}^\alpha \hat{I}_X \right] \frac{B}{2} \sin(\eta_\alpha) \\
&= \frac{B}{2} \hat{S}^\alpha \hat{I}_X \cos(\eta_\alpha) - i \left(-i \hat{S}^\alpha \hat{I}_Z\right) \frac{B}{2} \sin(\eta_\alpha) \\
&= \underbrace{\frac{B}{2} \hat{S}^\alpha \hat{I}_X \cos(\eta_\alpha)}_{\text{off-diagonal}} - \underbrace{\hat{S}^\alpha \hat{I}_Z \frac{B}{2} \sin(\eta_\alpha)}_{\text{diagonal}}. \tag{3.57}
\end{aligned}$$

Then, the off-diagonal and on-diagonal terms of the so transformed Hamiltonian read

$$\hat{H}_0^{D(\alpha), \text{diag}} = \left[\frac{-B}{2} \sin(\eta_\alpha) + \left(\omega_l - \frac{A}{2}\right) \cos(\eta_\alpha) \right] \cdot \hat{S}^\alpha \hat{I}_Z, \tag{3.58a}$$

$$\hat{H}_0^{D(\alpha), \text{off-diag}} = \left[\frac{B}{2} \cos(\eta_\alpha) - \left(\omega_l - \frac{A}{2}\right) \sin(\eta_\alpha) \right] \cdot \hat{S}^\alpha \hat{I}_X. \tag{3.58b}$$

The off-diagonal elements (eq. (3.57)) vanish at zero,

$$0 = \left[\frac{B}{2} \cos(\eta_\alpha) - \left(\omega_l - \frac{A}{2}\right) \sin(\eta_\alpha) \right] \cdot \hat{S}^\alpha \hat{I}_X, \tag{3.59}$$

$$\frac{B}{2} \cos(\eta_\alpha) = \left(\omega_l - \frac{A}{2} \right) \sin(\eta_\alpha), \quad (3.60)$$

$$\frac{\frac{B}{2}}{\left(\omega_l - \frac{A}{2} \right)} = \frac{\sin(\eta_\alpha)}{\cos(\eta_\alpha)}, \quad (3.61)$$

$$\boxed{\frac{B}{2\omega_l - A} = \tan(\eta_\alpha)}, \quad (3.62)$$

which represents the condition for the vanishing off-diagonal elements in α subspace.

In the second transformation, likewise, following the same method H_0^β can be diagonalized in the β subspace, when we get as the vanishing point for the off-diagonal elements:

$$\frac{-B}{2} \cos(\eta_\beta) = \left(\omega_l + \frac{A}{2} \right) \sin(\eta_\beta), \quad (3.63)$$

$$\frac{-\frac{B}{2}}{\left(\omega_l + \frac{A}{2} \right)} = \frac{\sin(\eta_\beta)}{\cos(\eta_\beta)}, \quad (3.64)$$

$$\boxed{\frac{-B}{2\omega_l + A} = \tan(\eta_\beta)}. \quad (3.65)$$

The Hamiltonian in final, diagonalized form, \hat{H}_0^D , is given as a sum of on-diagonal terms from α and β subspace:

$$\begin{aligned} \hat{H}_0^D &= \omega_s \hat{S}_z - \hat{H}_0^{D(\alpha),diag} - \hat{H}_0^{D(\beta),diag} \\ &= \omega_s \hat{S}_z + \left[\underbrace{\frac{B}{2} \sin(\eta_\alpha) - \left(\omega_l - \frac{A}{2} \right) \cos(\eta_\alpha)}_{\omega_{12}} \right] \cdot \hat{S}^\alpha \hat{I}_z \\ &\quad + \left[\underbrace{\frac{-B}{2} \sin(\eta_\beta) + \left(\omega_l + \frac{A}{2} \right) \cos(\eta_\beta)}_{\omega_{34}} \right] \cdot \hat{S}^\beta \hat{I}_z = \omega_s \hat{S}_z + \omega_{12} \hat{S}^\alpha \hat{I}_z + \omega_{34} \hat{S}^\beta \hat{I}_z, \end{aligned} \quad (3.66)$$

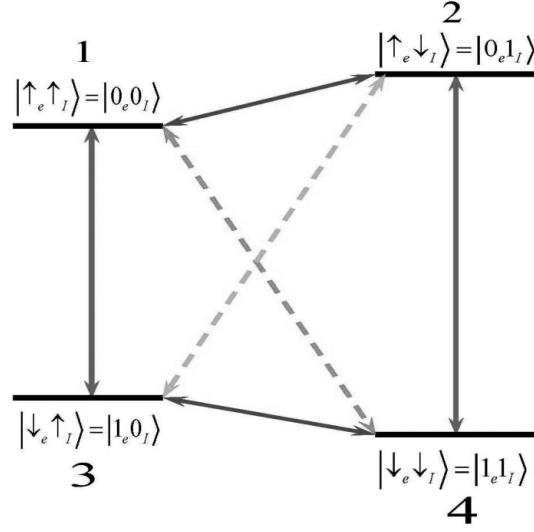


Figure 3.7: Quantum correlations scheme of the hyperfine coupled electron ($S = \frac{1}{2}$) to nuclear ($I = \frac{1}{2}$) spin in two two-level systems. Activated transition frequencies, ω_{14} and ω_{23} , associated with application of electromagnetic radiation pulse are marked via dashed line.

3.7 Interaction of electron-nuclear spin system with electromagnetic radiation

The rotating frame spin Hamiltonian for a two-spin particle is given by

$$\mathcal{H}_0 = \Omega_s S_z + \omega_I I_z + \mathbf{IAS}, \quad (3.71)$$

where $\Omega_s = \omega_s - \omega_{em}$, \mathbf{A} is the hyperfine coupling tensor, $\omega_s = \gamma_e B_0$ and $\omega_I = \gamma_I B_0$.

The two allowed electron – nuclear spin transition frequencies are $\Delta m_s = \pm 1, \Delta m_I = 0$, and the two forbidden are $\Delta m_s = \pm 1, \Delta m_I = \pm 1$. In the rotating frame they can be expressed as

$$\omega_{13} = \Omega_s + \frac{1}{2}(\omega_{12} - \omega_{34}), \quad \omega_{24} = \Omega_s - \frac{1}{2}(\omega_{12} - \omega_{34}), \quad (3.72a)$$

$$\text{and } \omega_{14} = \Omega_s + \frac{1}{2}(\omega_{12} + \omega_{34}), \quad \omega_{23} = \Omega_s - \frac{1}{2}(\omega_{12} + \omega_{34}), \text{ respectively.} \quad (3.72b)$$

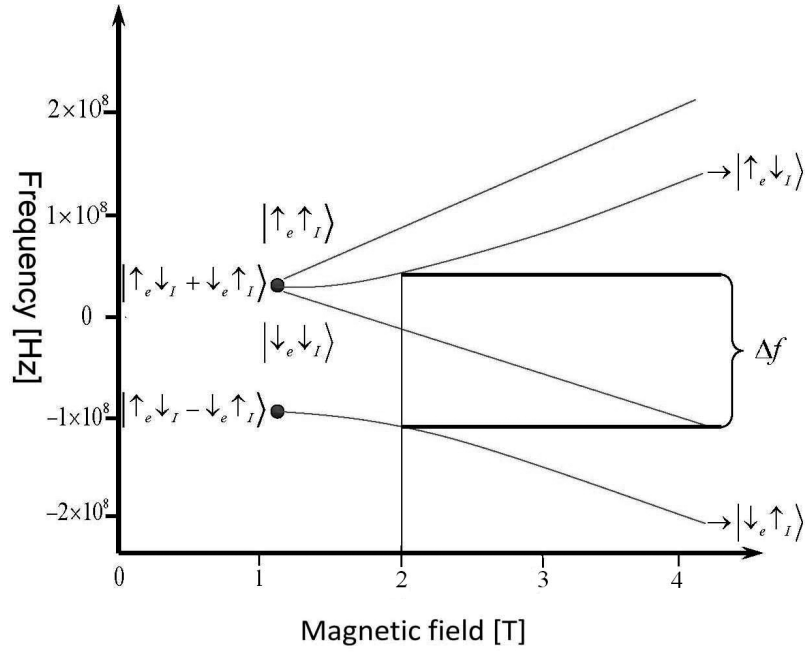


Figure 3.8: Schematic representation of hyperfine field induced frequency variation, Δf , needed for logical qubit state transfer between electron and nucleus: $\uparrow e \downarrow n \leftrightarrow \uparrow e \uparrow n$.

For a nucleus at $\vec{r} = 0$ and an arbitrary positioned electron wavefunction, $\varphi(r)$, the total electron-nuclear interaction Hamiltonian includes contact as well as dipolar hyperfine coupling terms:

$$\begin{aligned}
 \hat{B}_{IS} &= \int |\psi(r)|^2 \left\{ \frac{8\pi}{3} \gamma_e \gamma_n \hbar^2 \hat{I} \cdot \hat{S} \delta(r) + \frac{\gamma_e \gamma_n}{r^3} \hbar^2 \right. \\
 &\quad \times \left[3 \frac{(\hat{I} \cdot \vec{r})(\hat{S} \cdot \vec{r})}{r^2} - \hat{I} \cdot \hat{S} \right] \left. \right\} \\
 &= A_x \hat{S}_x \hat{I}_x + A_y \hat{S}_y \hat{I}_y + A_z \hat{S}_z \hat{I}_z.
 \end{aligned} \tag{3.73}$$

If the electron Zeeman energy $\gamma_e \hbar B_0$ is much larger than the hyperfine interaction energy A_x, A_y, A_z , the z-component of the electron spin operator commutes with the spin Hamiltonian:

$$[\hat{\mathcal{H}}, \hat{S}_z] \cong 0. \tag{3.74}$$

Consequently, a reduced spin Hamiltonian can be represented as following:

$$\hat{\mathcal{H}} = \gamma_n \hbar B_0 \hat{I}_z + \gamma_e \hbar B_0 \hat{S}_z + A_z \hat{S}_z \hat{I}_z, \quad (3.75)$$

where eigenstates are $|m_s\rangle|m_I\rangle$, $m_s = \pm\frac{1}{2}$, $m_I = \pm\frac{1}{2}$ with corresponding eigenenergies:

$$E = -\gamma_n \hbar B_0 m_I + \gamma_e \hbar B_0 m_s + A_z m_s m_I. \quad (3.76)$$

Assuming that $A_z > 0$, the hyperfine energy levels corresponding to $\gamma_n \hbar B_0 > A_z$ (a high field), and $\gamma_n \hbar B_0 < A_z$ (a low field) are shown in figure 3.9.

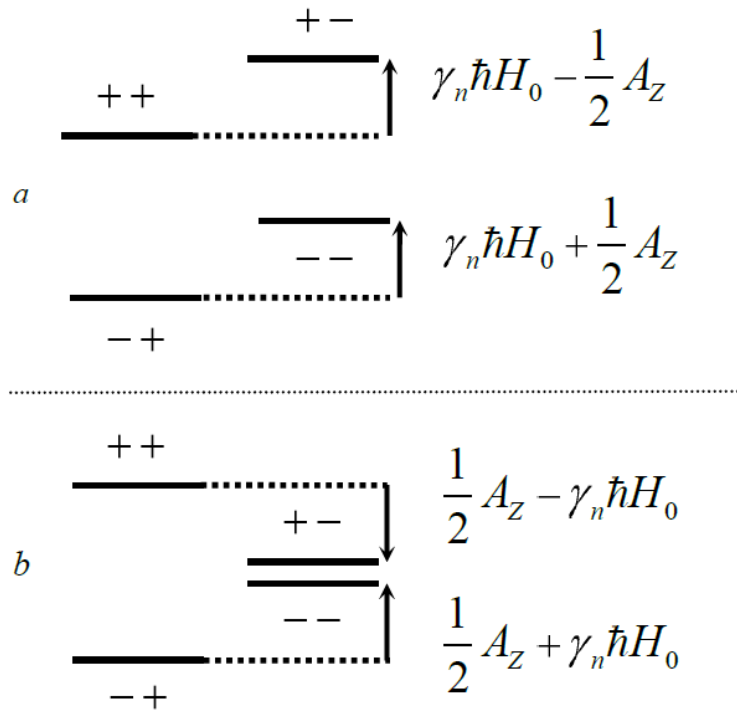


Figure 3.9: Hyperfine energy levels for coupled electron-nuclear spin pair $\left(S = \frac{1}{2}, I = \frac{1}{2}\right)$ in case of: (a) $\gamma_n \hbar B_0 > A_z$ and (b) $\gamma_n \hbar B_0 < A_z$, a schematic representation.

Chapter 4

Ion channeling in crystals

4.1 Introduction

The channeling of positively charged particles through a crystalline target is wide studied and experimentally utilized effect [56, 57] characterized by the confinement to a specific impact parameter area larger than the closest distance approach, r_{\min} , see figure 4.1.

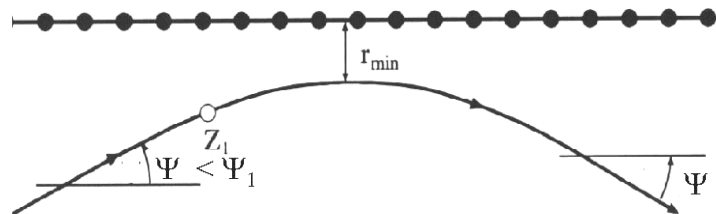


Figure 4.1: General scheme for channeling in crystalline target (scaling is exaggerated).

The steered motion of charged particle is established for incident angles $\psi < \psi_1$.

If the charged particle impinges upon the crystal under impact parameter close to a major crystal direction, the particle will experience a series of small-angle collisions as it passes through the collection of atomic strings parallel to the crystal axis. Depending on the primary orientation of entrance crystal plane it is possible to separate two different channeling regimes: the planar and the axial.

Under the planar channeling a particle performs a finite transverse motion localized between two adjacent crystallographic planes, while for the axial channeling a charged particle impinges a crystal with small angle to one of the main crystallographic axes.

So far, the channeling effect, theory, numerous experiments and their various applications have been described in detail in several review articles of Morgan [58], Gemmel [59], Beloshitsky [60].

Two modes of axial channeling founded by Robinson and Oen [61] refer to a hyperchanneling and doughnut mode respectively. First case is established when the particle trajectory is confined to one axial channel during transmission through a crystal [62]. In general, hyperchanneling mode can be established only in very thin perfect crystalline targets (due to small percentage of energy losses) for very small angles of incidence and negligible beam divergence. A second mode is obtained when the particle with a sufficient transverse energy passes the potential barrier entering into the lattice of atomic strings while it changes its transverse momentum direction in collisions with the strings [63].

Lindhard [64] has laid the theoretical foundations of channeling by introducing the so-called axial and planar continuum models and critical angle dependencies of the charged particle oscillatory motion guided by the harmonic potential in the crystal. These items are concisely described in the following section.

4.2 Continuum Model

Continuum Model represents the approximation of the actual periodic potential of atomic string (plane) with a collective potential averaged over all single ion-atom potentials $V(R)$.

The continuum approximation is valid only for large impact parameters and small angles of incidence. The approximation breaks down for a particle entrance at a distance to atomic string - less than the critical approach, r_{crit} . This restriction further implies a critical value E_{crit} for the transverse energy and the critical angle, ψ_{crit} , for angle of incidence, ψ , as following

$$U(r_{crit}) = E_{crit} = E\psi_{crit}^2. \quad (4.1)$$

Hence, the continuum approximation in the axial channeling is valid until the angle of incidence of the particle upon a main crystal axis is less than the critical angle for channeling:

$$\psi_1 = \sqrt{\frac{2Z_1Z_2e^2}{Ed}}, \quad (4.2)$$

where E is the energy of the incident particle and d is in interatomic distance.

Correspondingly, for the planar channeling the critical angle is

$$\psi_2 = \sqrt{\frac{2\pi Z_1Z_2e^2aN_{at}d_p}{Ed}}, \quad (4.3)$$

where d_p is the interplanar distance, N_{at} is the atomic density, and $a = \frac{0.8853 a_0}{\sqrt{Z_1^{2/3} + Z_2^{2/3}}}$ is

the Thomas-Fermi screening length.

Thus, as long as the following condition is satisfied:

$$2 \left[\left(\frac{M}{m_e} \right) Z_1 Z_2^{1/3} (a_0/d) \right]^{1/2} \gg 1, \quad (4.5)$$

where $a_0 = 0.53 \text{ \AA}$ is the Bohr radius, Z_1 and M are the projectile atomic number and mass, respectively, and m_e is the electron mass; the close encounter process leading to the nuclear reaction, does not occur.

4.3 Thomas-Fermi interaction potential in continuum approximation

For the system of one atomic row, the continuum potential at distance r from a string of atomic nuclei is given by the following relation

$$U(r) = \frac{1}{d} \int_{-\infty}^{+\infty} V \sqrt{z^2 + r^2} dz, \quad (4.6)$$

where d is the interatomic distance between the crystal atoms composing one string and $\sqrt{z^2 + r^2}$ is the distance between the channeled particle and the nuclei measured along the string in the channeling direction.

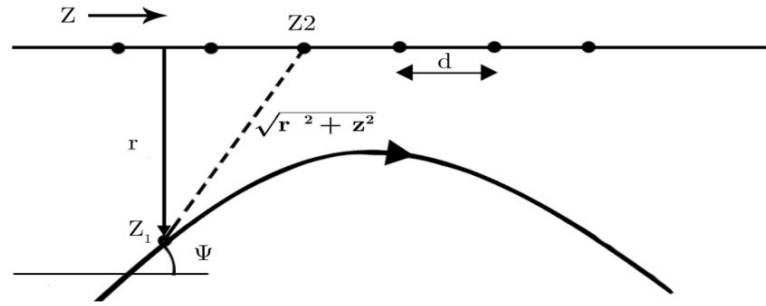


Figure 4.2: Trajectory schematics of channeled particle close encounter with atomic string in continuum model, scaling is idealized.

In the axial channeling regime the former relation is given by

$$V(r) = \frac{2Z_1Z_2e^2}{d} \chi\left(\frac{r}{a}\right) = E\psi_1^2 \chi\left(\frac{r}{a}\right), \quad (4.7)$$

where r is the distance between channeled ion and lattice atom and $\chi\left(\frac{r}{a}\right)$ is the Thomas-Fermi (TF) screening function obtained as the solution of Thomas-Fermi differential equation (see next subsection):

$$\left(\frac{r}{a}\right)^{1/2} \frac{d^2}{d\left(\frac{r}{a}\right)^2} \chi\left(\frac{r}{a}\right) = \chi\left(\frac{r}{a}\right)^{3/2}. \quad (4.8)$$

For the TF screening function the most commonly used approximation in the case of ion channeling are the Lindhard [64] and Molière [65]. In this thesis it is included the Molière screening function approximation of the Thomas-Fermi interaction potential:

$$\chi\left(\frac{r}{a}\right) = \sum_{i=1}^3 \alpha_i \exp\left(-\frac{\beta_i r}{a}\right), \quad (4.9)$$

where $\chi(\xi) = \sum_{i=1}^3 \alpha_i K_0(\beta_i \xi)$, K_0 is the zero-order modified Bessel function of the second kind [66], with $\{\alpha_i\} = \{0.10; 0.55; 0.35\}$ and $\{\beta_i\} = \{6.0; 1.2; 0.3\}$.

From figure 4.3 it is clear that Molière screening function has an excellent agreement with the Thomas-Fermi screening function for all values of the variables that are less than ten. By inserting equation for ion-atomic interaction potential (2.4) and (2.6) in the expression for the continuous potential (2.3) we get the expression for the Thomas-Fermi interaction potential in Molière approximation:

$$U(r) = \frac{2Z_1 Z_2 e^2}{d} \sum_{i=1}^3 \alpha_i K_0\left(\beta_i \frac{r}{a}\right) \Rightarrow$$

$$\Rightarrow U(r) = \frac{2Z_1 Z_2 e^2}{d} \left[0.1K_0\left(\frac{6r}{a}\right) + 0.55K_0\left(\frac{1.22r}{a}\right) + 0.35K_0\left(\frac{0.3r}{a}\right) \right]. \quad (4.10)$$

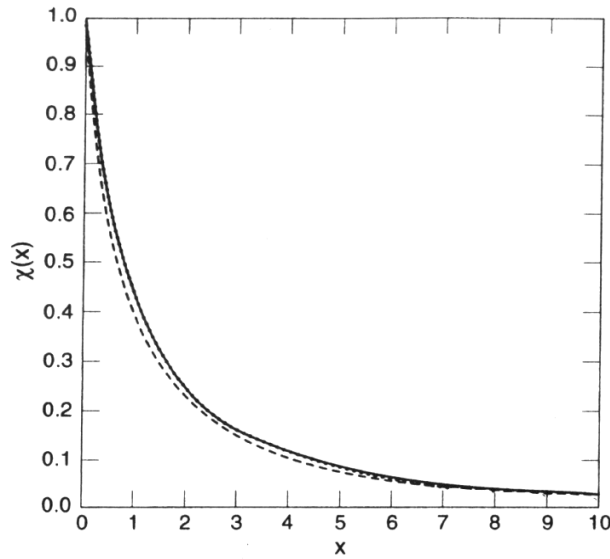


Figure 4.3: Thomas-Fermi potential dependence on parameter $x = r/a$, a full line, and Thomas-Fermi interaction potential in Molière approximation, a dashed line.

It is possible to include the effect of thermal vibrations of the lattice atoms [66] assuming that the channeled ions have high enough speed, so that can "see" the atoms as fixed in space and shifted from their equilibrium positions. Also, these small thermal

shifts are mutually independent, and can be described by a Gaussian distribution [68], whose standard deviation, σ_{th} , is equal to the one-dimensional amplitude of thermal vibrations of atoms. As a result, the total potential of the continuous interaction of ions and the i -th atomic string, including the effects of thermal vibrations of lattice atoms, is given by following

$$U_i^{th} = U_i + \frac{\sigma_{th}^2}{2} \left(\frac{\partial^2}{\partial x^2} U_i + \frac{\partial^2}{\partial y^2} U_i \right). \quad (4.11)$$

II

RESULTS

Chapter 5

Superfocusing of channeled protons in a $\langle 100 \rangle$ Si thin crystal

Introduction 5.1

As a first step toward manipulation at subatomic level precision in condensed matter systems under ion channeling regime this chapter elucidates semiclassical theory behind superfocusing effect. The obtained results pave a way for utilization of a picometer resolution solid-state manipulation technique – applicable for the subatomic microscopy as well as nuclear quantum state engineering. Here we demonstrate that it is possible to measure the cross-section for the process of proton induced X-ray emission as a function of the proton impact parameter within the foreign atom, giving the transverse projection of the electron density within the atom. This dependence would have several points, corresponding to the numbers of values of incident angle, φ . Such a measurement technique, named the subatomic microscopy, can be successfully implemented in the quantum information processing as a method for quantum state read out. It could be also used to measure, e.g., the cross-section for a (p, α) nuclear reaction as a function of the proton impact parameter within the foreign atom.

In the following it is presented a theoretical route for explaining the subatomic confinement of the proton beam of the initial energy of 2 MeV channeled along the $\langle 100 \rangle$ axis of a Si thin crystal for different values of the proton beam incident angle. It is demonstrated that the half-width of the proton beam can be made much smaller than the Bohr radius, i.e., the average radius of a hydrogen atom in its ground state. This effect is called the effect of superfocusing of channeled ions [69]. Obtain results show that it is possible to use such a proton beam to probe the interior of a foreign atom inserted in the channel by changing gradually the proton beam incident angle. In

particular, the superfocusing effect of protons channeled in a $\langle 100 \rangle$ Si thin crystal is analyzed in detail.

The initial proton energy is 2 MeV and the proton beam incident angle is increased gradually from zero up to 20 % of the critical angle for channeling. The reduced crystal thickness is varied between 0.20 and 0.30, the corresponding range of crystal thickness being between 66.1 and 99.2 nm. The spatial distributions of channeled protons, obtained by the numerical solution of the proton equations of motion in the transverse plane and a realistic Monte Carlo computer simulation code, are presented as functions of the proton beam incident angle and reduced crystal thickness. They are analyzed via the corresponding mappings of the impact parameter plane to the transverse position plane, which is dominated by the rainbow effect. The performed analysis shows that it is possible to focus the proton beam within the region of the radius considerably below the Bohr radius for all the considered values of the proton beam incident angle.

In recent years, as the characteristic dimensions of devices made of advanced materials have approached the atomic scale, obtaining the information on their structure-properties relationships around this limit is emerging as a fundamental request in materials and devices engineering [70-73]. On the other hand, one of the major driving forces in the field of ion channeling is the requirement to guide and focus the beam to nanometer sized regions [74, 75].

The possibility of superfocusing of channeled ions was first observed by Demkov and Meyer [69]. Following the theoretical studies of Miletić et al. [76, 77] and Živković et al. [78], they analyzed the axial focusing of 1 MeV protons in the $\langle 100 \rangle$ channel of a Si thin crystal assuming that the continuum proton-crystal interaction potential was dominantly cylindrically symmetric and harmonic. The effect was also considered by Nešković et al. [79], who treated it as the crystal rainbow effect [80, 81], whose occurrence had been confirmed experimentally by Krause et al. [82, 83]. The continuum proton-crystal interaction potential was of the Thomas-Fermi type, having both the harmonic and anharmonic components.

Here we describe an approach aimed at achieving the picometer measurement resolution. It is based on using the superfocused proton beam, in the crystal channel, for

scanning the interior of a foreign atom, being localized near the superfocusing point. The approach has the potential for a breakthrough in the field of subatomic microscopy.

In order to outline the main features of the superfocusing effect, the spatial distributions of channeled protons, i.e., their distributions in the transverse position plane, for different values of the proton beam incident angle and reduced crystal thickness are analyzed in detail.

5.2 Semiclassical model of the superfocusing effect induced by proton channeling

The system considers a proton moving through an axial channel of a thin Si crystal. We employ the classical model of ion channeling assuming that the interaction between the proton and crystal's atoms is elastic [64]. In the proton trajectory calculations we use the Thomas-Fermi proton-atom interaction potential [59] in the Molière approximation [64, 65], which is

$$V(r') = \frac{Z_1 Z_2 e^2}{r'} [0.35 \exp(-br') + 0.55 \exp(-4br') + 0.10 \exp(-20br')], \quad (5.1)$$

where Z_1 and Z_2 are the atomic numbers of the hydrogen and silicon atoms, respectively, e is the elementary charge, r' is the distance between the proton and atom, $b = 0.3/a$, $a = [9\pi^2 / (128Z_2)]^{1/3} a_0$ is the screening radius of the atom, and $a_0 = 52.9$ pm is the Bohr radius [85]. The z axis is taken to be parallel to the $\langle 100 \rangle$ Si crystallographic axis with the origin lying in the entrance plane of the crystal. The proton beam axis lies in the xz plane and makes angle φ with the z axis, being the proton beam incident angle. We further apply the continuum approximation [64]. As a result, the continuum interaction potential of the proton and crystal is obtained as a sum of the continuum interaction potentials of the proton and crystal's atomic strings,

$$U^{th}(x, y) = \sum_{i=1}^M U_i^{th}(x, y), \quad (5.2)$$

where x and y are the transverse components of the proton position and M is the number of atomic strings. This expression includes the thermal vibrations of the atoms.

The continuum interaction potential of the proton and i th atomic string is [59]

$$U_i^{th}(x, y) = U_i(x, y) + \frac{\sigma_{th}^2}{2} [\partial_{xx} U_i(x, y) + \partial_{yy} U_i(x, y)], \quad (5.3)$$

where $U_i(x, y)$ is the continuum interaction potential of the proton and i th atomic string without the effect of thermal vibrations taken into account, and σ_{th} the one-dimensional thermal vibration amplitude of the atoms.

We include in the calculations of the spatial distributions of channeled protons the effects of their collisions with the crystal's electrons. The specific (electronic) energy loss of the proton in the channel is taken into account via relation

$$-\frac{dE}{dz} = \frac{4\pi Z_1^2 e^4}{m_e v^2} n_e \ln \frac{2m_e v^2}{\hbar \omega_e}, \quad (5.4)$$

where m_e is the electron mass, v the proton velocity, $n_e = \Delta U^{th}(x, y)/(4\pi)$ the density of the crystal's electron gas averaged along the z axis, $\Delta = \partial_{xx} + \partial_{yy}$, \hbar the reduced Planck constant, and $\omega_e = (4\pi e^2 n_e / m_e)^{1/2}$ the angular frequency of the oscillations of the electron gas induced by the proton [59]. The specific change of the dispersion of the proton scattering angle caused by its collisions with the electrons is included in the form

$$\frac{d\Omega^2}{dz} = \frac{m_e}{m_p^2 v^2} \left(-\frac{dE}{dz} \right), \quad (5.5)$$

where m_p is the proton mass [59]. The corresponding dispersions of the components of the proton scattering angle are $\Omega_x^2 = \Omega_y^2 = \Omega^2 / 2$.

Our calculations are based on the theory of crystal rainbows, and are focused on the appearance of rainbows in the proton transmission through the $\langle 100 \rangle$ Si thin crystal

when the proton beam does not coincide with the crystallographic axis, i.e., when the crystal is tilted relative to the plane perpendicular to the proton beam. This theory enables us to analyze the spatial distributions of channeled protons via the corresponding rainbow patterns. These distributions are generated using the numerical solution of the proton equations of motion in the transverse position plane and a realistic Monte Carlo computer simulation code.

The analysis of the proton scattering process in question is carried out via the mapping of the impact parameter plane to the transverse position plane [86, 87] in accordance with the chosen values of φ and the reduced crystal thickness, Λ . The Jacobean of this mapping, i.e., the ratio of the infinitesimal surfaces in the transverse position plane and impact parameter plane, reads

$$J_r(x_0, y_0, \varphi, \Lambda) = \frac{\partial x}{\partial x_0} \frac{\partial y}{\partial y_0} - \frac{\partial x}{\partial y_0} \frac{\partial y}{\partial x_0}, \quad (5.6)$$

where x_0 and y_0 are the components of the proton impact parameter, i.e., the components of its initial position in the transverse position plane. Thus, equation $J_r(x_0, y_0, \varphi, \Lambda) = 0$ determines the lines in the impact parameter plane along which the proton yield in the transverse position plane is singular.

5.3 Results and Discussion

This section discusses the effect of superfocusing of protons channeled in the $\langle 100 \rangle$ Si thin crystal for various proton beam incident angles. The initial proton energy, E_0 , is 2 MeV and the crystal thickness, L , is changed from 66.1 nm to 99.2 nm.

The corresponding values of the reduced crystal thickness, $\Lambda = f_r L / v_0$, where $f_r = 5.94 \times 10^{13}$ Hz is the average frequency of the transverse proton motion close to the channel axis and v_0 the initial proton velocity [88], are between 0.20 and 0.30. The proton beam incident angle is varied in the range between 0 and $\pm 0.20\psi_c$, where

$\psi_c = [2Z_1Z_2e^2/(dE_0)]^{1/2} = 6.09$ mrad is the critical angle for channeling, with d being the distance between the crystal's atoms within the atomic strings [64]. The one-dimensional thermal vibration amplitude of the atoms is $\sigma_{th} = 7.4$ pm [67].

It is assumed that the crystal's atomic strings defining the channel intersect the x and y axes. The number of atomic strings is 36, i.e., we take into account the atomic strings lying on the three nearest square coordination lines [88]. The proton equations of motion in the transverse position plane are solved numerically using the Runge Kutta method of the fourth order [66]. The components of the proton impact parameter, x_0 and y_0 , are chosen randomly from the uniform distributions within the region of the channel. The initial number of protons was 4,294,967.

Figure 5.1 presents the spatial distributions of channeled protons along the x axis for nine values of the proton beam incident angle, $\varphi = 0, \pm 0.05\psi_c, \pm 0.10\psi_c, \pm 0.15\psi_c$ and $\pm 0.20\psi_c$, and $A = 0.25$, corresponding to $L = 82.6$ nm. Each of these distributions contains one maximum. As one would expect, for $\varphi = 0$ the maximum lies at the origin, for positive values of φ on the positive part of the x axis, and for the negative values of φ on the negative part of the x axis. The larger the modulus of φ , the larger the displacement of the maximum from the origin. Also, when the modulus of φ is larger, the maximum is weaker and broader. These maxima are due to the effect of superfocusing of channeled protons, which is explained by the dominance of the harmonic component of the continuum proton-crystal interaction potential, given by eq. (5.2), over its anharmonic component in the region close to the channel axis [69, 79].

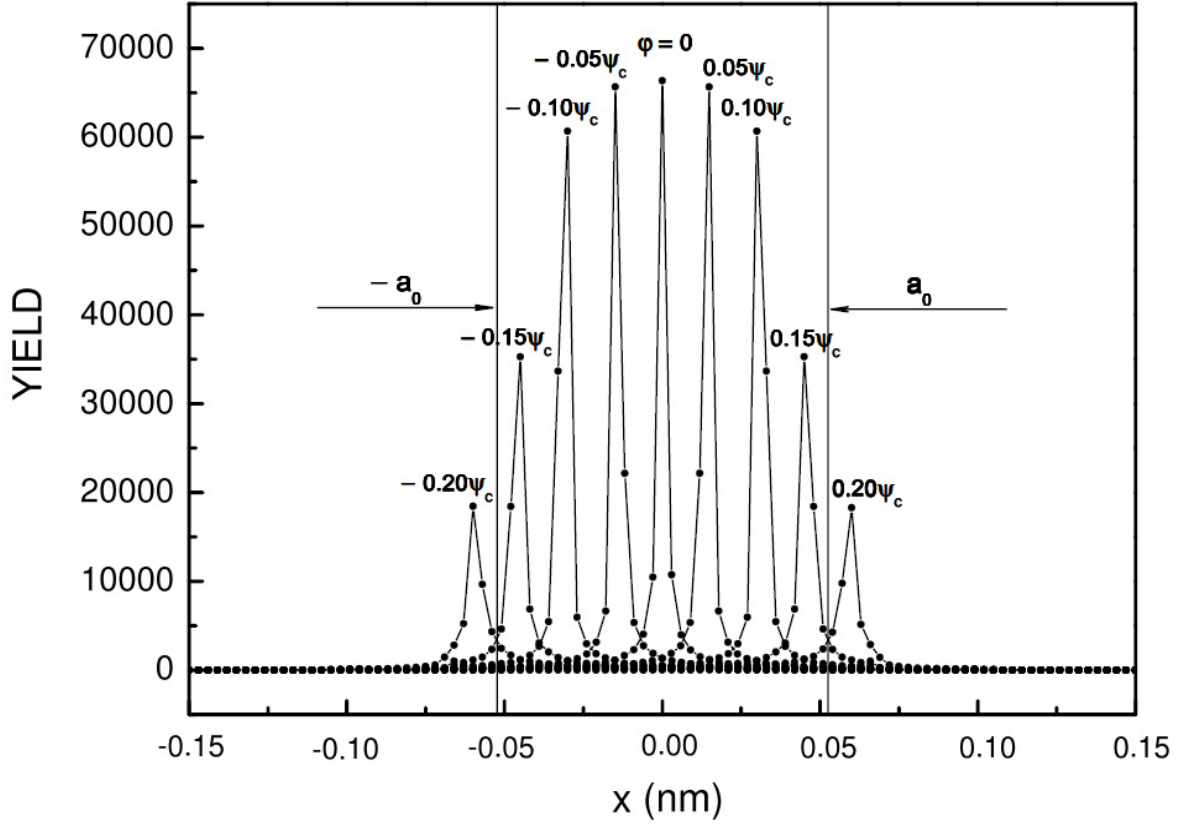


Figure 5.1: The yields of channeled protons along the x axis in the transverse position plane for the proton beam incident angles $\varphi = 0, \pm 0.05\psi_c, \pm 0.10\psi_c, \pm 0.15\psi_c$ and $\pm 0.20\psi_c$ and the reduced crystal thickness $\Lambda = 0.25$, corresponding to the crystal thickness $L = 82.6$ nm.

The heights of the maxima for $\varphi = \pm 0.05\psi_c, \pm 0.10\psi_c, \pm 0.15\psi_c$ and $\pm 0.20\psi_c$ are 99, 92, 53 and 28 % of the height of the maximum for $\varphi = 0$, respectively. The displacements of the maxima for $\varphi = \pm 0.05\psi_c, \pm 0.10\psi_c$ and $\pm 0.15\psi_c$ from the origin are below a_0 , and one can say that these maxima are strong and narrow. For $\varphi = \pm 0.20\psi_c$ the displacement of the maxima from the origin is above a_0 , and the maximum is weak and broad.

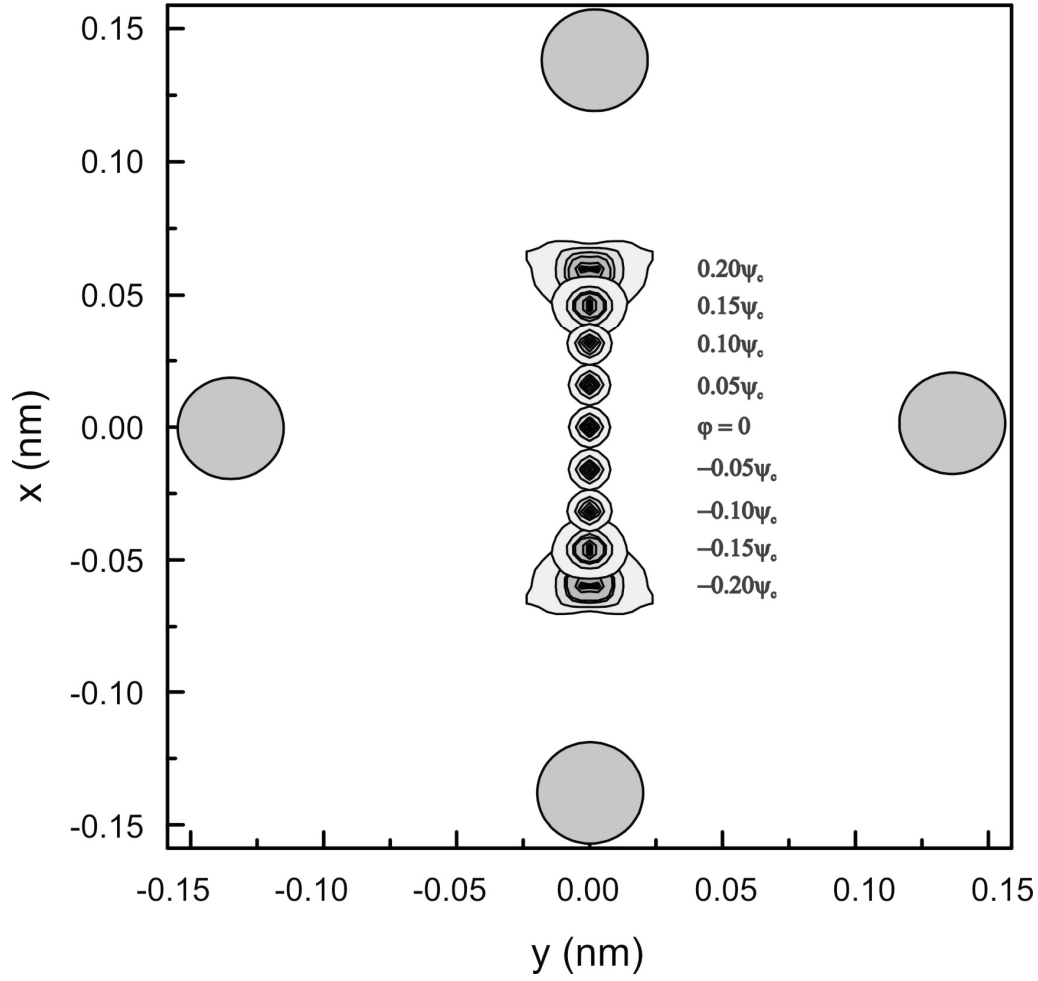


Figure 5.2: The yields of channeled protons in the transverse position plane in the two-dimensional representation for the proton beam incident angles $\varphi = 0, \pm 0.05\psi_c, \pm 0.10\psi_c, \pm 0.15\psi_c$ and $\pm 0.20\psi_c$ and the reduced crystal thickness $\Lambda = 0.25$, corresponding to the crystal thickness $L = 82.6$ nm. The area in which the yield of channeled protons is below 5 % is designated by white color, the areas in which the yields are between 5 and 10 %, 10 and 15 %, 15 and 20 %, 20 and 50 %, and 50 and 80 % by the increasing tones of gray color, respectively, and the area in which the yield is above 80 % by black color. The atomic strings defining the channel are represented by the four circles lying on the x and y axes.

This suggests that, by varying φ from 0 to $\pm 0.15\psi_c$, one could probe the interior of a foreign atom inserted in the channel at the depth of $\Lambda = 0.25$, i.e., at the superfocusing point in the first rainbow cycle [79]. The weakening of the superfocusing effect for $\varphi =$

$\pm 0.20\psi_c$ can be attributed to the fact that in these cases the proton beam is displaced considerably from the channel axis toward the upper or lower channel wall, and moves through the region of the channel in which the anharmonic component of the interaction potential is more pronounced than its harmonic component [69, 79].

The spatial distributions of channeled protons in the two-dimensional representation for $\varphi = 0, \pm 0.05\psi_c, \pm 0.10\psi_c, \pm 0.15\psi_c$ and $\pm 0.20\psi_c$ and $A = 0.25$ are shown in figure 5.2. It is evident that for $\varphi = 0, \pm 0.05\psi_c, \pm 0.10\psi_c$ and $\pm 0.15\psi_c$ each of the distributions has one strong and narrow maximum. The shapes of the areas of the distributions for $\varphi = 0, \pm 0.05\psi_c$ and $\pm 0.10\psi_c$ representing the constant proton yields are circular, while the shapes of the areas of the distributions for $\varphi = \pm 0.15\psi_c$ are ellipsoidal. For $\varphi = \pm 0.20\psi_c$ the distributions become broader and each of them contains two maxima displaced symmetrically along the positive and negative parts of the y axis, and the shapes of their areas representing the constant proton yields deviate from the ellipsoidal ones.

It is clear that for these values of φ the superfocusing effect is considerably attenuated and dissolved. Thus, as it has been suggested above, the possibility to use the proton beam for probing the interior of a foreign atom inserted in the channel at the superfocusing point exists only for the values of the modulus of φ below $0.15\psi_c$. Figures 5.3(a) and 5.3(b) give the distributions for $\varphi = 0.10\psi_c$ and $0.20\psi_c$ in the three-dimensional representation. Note that the scales of the yield axes in the two figures coincide. These two distributions show clearly the splitting of the superfocusing maximum for the larger value of φ .

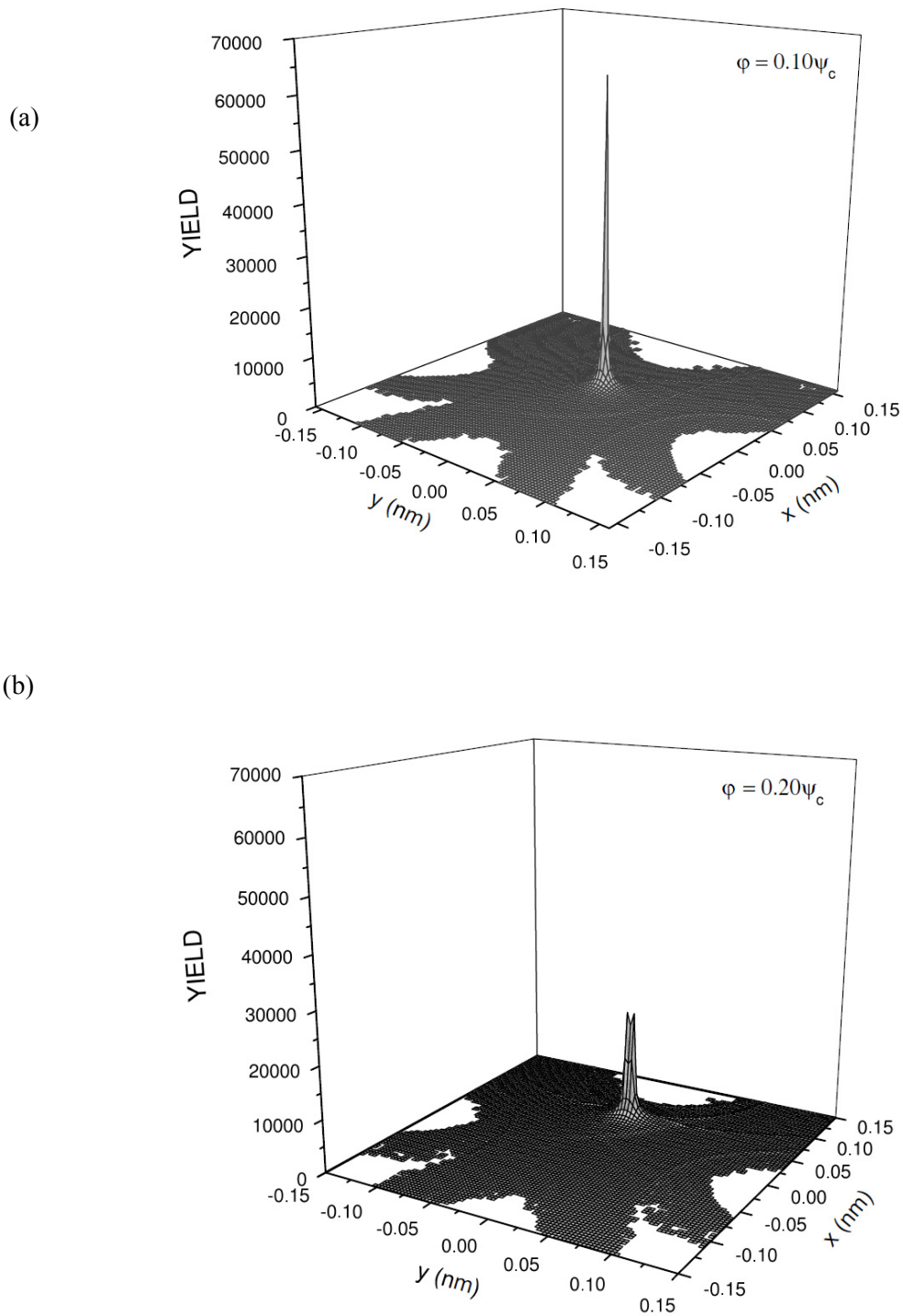


Figure 5.3 (a, b): The yields of channeled protons in the transverse position plane in the three-dimensional representation for the proton beam incident angles (a) $\phi = 0.10\psi_c$ and (b) $\phi = 0.20\psi_c$ and the reduced crystal thickness $\Lambda = 0.25$, corresponding to the crystal thickness $L = 82.6$ nm.

Figures 5.4(a) and 5.4(b) give the rainbow lines in the transverse position plane for $\varphi = 0.05\psi_c$, $0.10\psi_c$, $0.15\psi_c$ and $0.20\psi_c$ and $\mathcal{A} = 0.25$, which correspond to the spatial distributions of channeled protons in the upper part of the transverse position plane shown in figure 5.2.

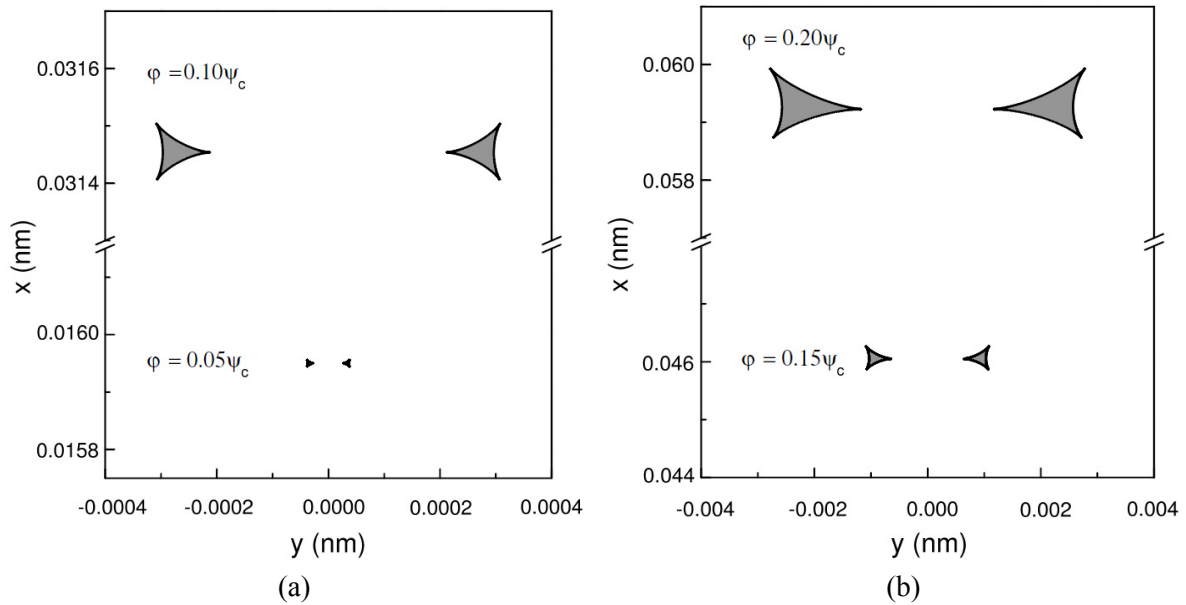


Figure 5.4 (a, b): The evolution of the rainbow pattern in the transverse position plane with the proton beam incident angle, for (a) $\varphi = 0.05\psi_c$ and $0.10\psi_c$ and (b) $\varphi = 0.15\psi_c$ and $0.20\psi_c$, for the reduced crystal thickness $\mathcal{A} = 0.25$, corresponding to the crystal thickness $L = 82.6$ nm.

The rainbow patterns for $\varphi = -0.05\psi_c$, $-0.10\psi_c$, $-0.15\psi_c$ and $-0.20\psi_c$ and the same value of \mathcal{A} lie in the transverse position plane symmetrically with respect to the y axis to the corresponding patterns shown in this figure. It has been already established that for $\varphi = 0$ the rainbow line comes to a point, when the effect of superfocusing of channeled protons is most pronounced [79]. Note that the scale of the x and y axes in the former figure is 10 times smaller than the corresponding scales in the latter figure. As φ increases, the pattern shifts along the x axis.

However, this shift decreases as the pattern approaches the atomic string intersecting the x axis. Also, with the increase of φ , the two patterns become larger and more separated from each other.

Comparison of these figures with figures 5.2 and 5.3 demonstrates that, in spite of the fact that rainbow patterns for $\varphi = 0.05\psi_c$, $0.10\psi_c$ and $0.15\psi_c$ is composed of two parts, each of the corresponding spatial distributions of channeled protons contains only one maximum.

The two rainbows for $\varphi = 0.20\psi_c$ are responsible for the two maxima appearing in the corresponding spatial distribution. However, one should note that for each of the considered values of φ , rainbow pattern lies within a circle of the radius much smaller than a_0 .

In the analysis presented in figures 5.1-5.4, direction of the incident proton beam is changed along the x axis, i.e., toward the atomic strings defining the channel that intersects this axis. We have also explored the spatial distributions of channeled protons for the reduced crystal thickness $\Lambda = 0.25$ and direction of the incident proton beam changing along line $y = x$, i.e., between the atomic strings defining the channel. The obtained results are similar to the ones presented in these figures, including the splitting of the superfocusing maximum for the larger values of the proton beam incident angle.

In next step it is considered a foreign atom inserted in the channel near the superfocusing point and exposed to the proton beam. The insertion of the atom can be performed by the technique of ion implantation. One of results of the proton-foreign atom interaction can be an inner-shell ionization of the atom resulting in the emission of a characteristic X-ray. This process is called proton induced X-ray emission (PIXE). It is illustrated in figure 5.5.

The distance between the channel walls is 271.5 pm, the half-width of the proton beam is $R_m = 5.0$ pm [69], and the radius of the foreign atom is $R_a = 100$ pm, corresponding to a sulfur atom [89]. The half-width of the proton beam is taken to be constant in the interaction region since the length of the superfocusing region, which is the region

around the superfocusing point, is much larger than R_a [69]. For $\varphi = 0$, the protons propagate through the foreign atom along its diameter coinciding with the z axis, and for $\varphi = 0.05\psi_c$, $0.10\psi_c$, $0.15\psi_c$ and $0.20\psi_c$ they propagate through the atom along its chords being practically parallel to the z axis. The larger the value of φ , the smaller the length of the chord. The proton beam shown in the figure corresponds to $\varphi = 0.05\psi_c$.

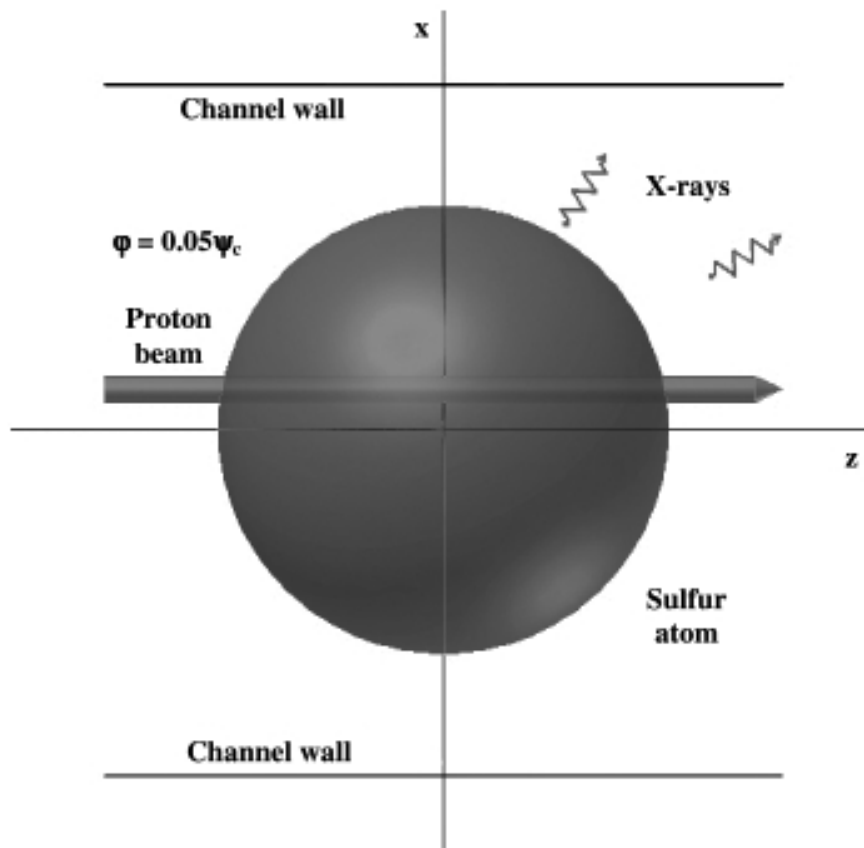


Figure 5.5: An illustration of the interaction of the proton beam with the inner-shell electrons of a sulfur atom inserted in the channel near the superfocusing point resulting in the emission of characteristic X-rays.

This simple geometrical analysis demonstrates the possibility for measuring the cross-section for PIXE as a function of the proton impact parameter within the foreign atom. Thus, one could measure the electron density within the foreign atom. Such a probing of the interior of the foreign atom can be named the rainbow subatomic microscopy.

Another result of the proton-foreign atom interaction can be the excitation of the atom's nucleus resulting in the emission of an α -particle, i.e., a (p, α) nuclear reaction.

In this case one could measure the cross-section for this nuclear reaction as a function of the proton impact parameter within the foreign atom [69].

The realization of the idea of subatomic microscopy depends crucially on the possibility to localize foreign atom near the superfocusing point, i.e., to make it practically coincide with the proton beam neck. Displacement of the foreign atom from the proton beam neck can be compensated by varying the initial proton energy upward or downward to move the neck forward or backward, respectively, and make "the two objects" coincide. However, the effect of thermal vibrations of the foreign atom makes its position uncertain. Since the corresponding one-dimensional thermal vibration amplitude is comparable with R_m [67], one should cool the crystal to a temperature well below room temperature to make the effect less pronounced. Resolution of the microscopy is determined by the ratio of the diameter of foreign atom and the full-width of the proton beam. In the above described example this ratio is 20. Thus, in accordance with the above given simple geometrical analysis, one can choose the seven values of φ , 0, $\pm 0.05\psi_c$, $\pm 0.10\psi_c$ and $\pm 0.15\psi_c$, and obtain seven well-separated measurement points. If the cross-section for PIXE is measured, the final result of the experiment would be the transverse projection of the electron density within the foreign atom. In this case the sensitivity of the microscopy is determined by the way the cross-section depends on the electron density.

Figure 5.6 shows the dependences of the yields of channeled protons around the centers of their spatial distributions on A in the region between 0 and 0.3 for $\varphi = 0$ and $0.10\psi_c$. For the region in the transverse position plane around this center we take the circular region around it having the radius smaller than $r_c = 0.1a_0 = 5.3$ pm. The value of r_c is chosen to be close to the half-width of the proton beam at the superfocusing point ($R_m = 5.0$ pm). The maxima of these dependences are attributed to the superfocusing effect. Their positions for the two values of φ are 0.246 and 0.245, the corresponding values of L being 81.3 and 81.0 nm, respectively.

The height of the maximum for $\varphi = 0.10\psi_c$ amounts to 98 % of the height of the maximum $\varphi = 0$. The full-widths of the two maxima are 0.084 and 0.083, respectively, and the corresponding values of ΔL are 27.8 and 27.5 nm, respectively. It is evident that these values are much larger than R_a . The small downward shifts of the positions of the two maxima away from the superfocusing point can be attributed to the presence of the small but not negligible anharmonic component of the continuum proton-crystal interaction potential. The fact that values of the position, height and full-width of the two maxima do not deviate much from each other is in accordance with the previously drawn conclusion that for $\varphi = 0.10\psi_c$ the superfocusing effect is still very pronounced.

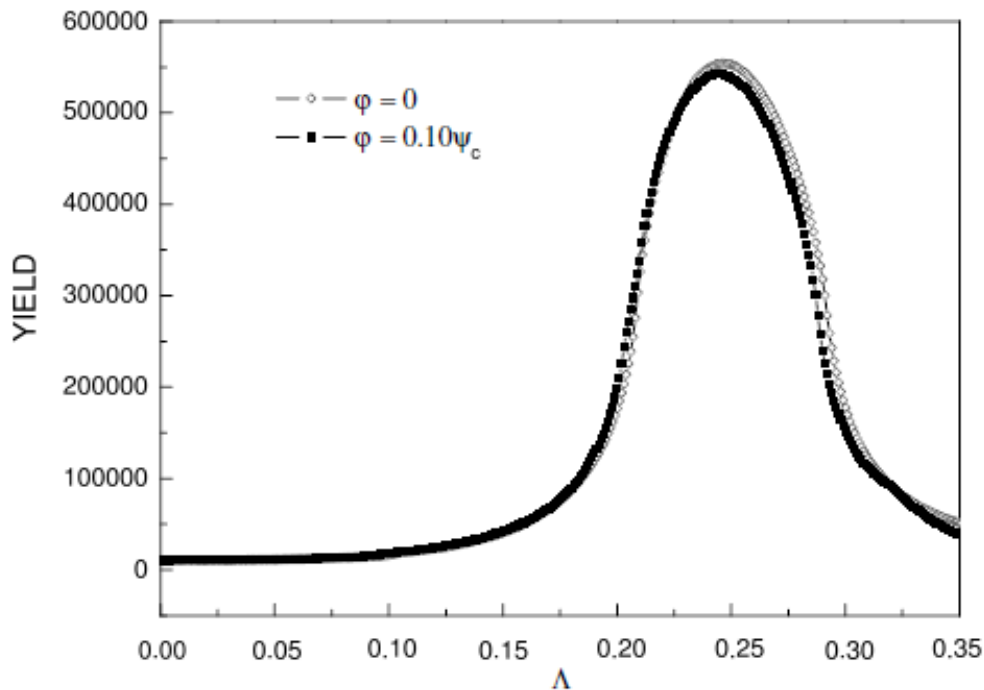


Figure 5.6: The yields of channeled protons around the centers of their spatial distributions as functions of the reduced crystal thickness in the vicinity of the superfocusing point for the proton beam incident angles $\varphi = 0$ and $0.10\psi_c$.

We shall also analyze the evolution of the rainbow pattern in the transverse position plane with Λ in the vicinity of the superfocusing point for $\varphi = 0.10\psi_c$.

The patterns for $\mathcal{A} = 0.200, 0.220$ and 0.240 consist of a cusped rectangular line with the cusps directed between the atomic strings defining the channel.

The evolution of the rainbow patterns [90-92] with \mathcal{A} in the region between 0.240 and 0.260 is displayed in figure 5.7. For $\mathcal{A} = 0.245$ the pattern is composed of two cusped triangular lines, each of them with two cusps directed between the atomic strings defining the channel and one cusp directed along the y axis and toward the third cusp of the other line. Thus, the increase of \mathcal{A} toward the value of 0.250 induces the splitting of the cusped rectangular rainbow line. The rainbow pattern for $\mathcal{A} = 0.250$, which is also shown in figure 5.4, consists of two cusped triangular lines, as the rainbow pattern for $\mathcal{A} = 0.245$. These two rainbows are separated from each other less than the two rainbows occurring for $\mathcal{A} = 0.245$. For $\mathcal{A} = 0.255$, the rainbow pattern contains two cusped triangular line. These two rainbows are larger than the two rainbows occurring for $\mathcal{A} = 0.250$ and they overlap. The rainbow pattern for $\mathcal{A} = 0.260$ consists of a deltoidal line with two joints of its sides having the form of a swallow-tail directed along the x axis and the other two joints of its sides having the form of a cusp directed along the y axis. The rainbow patterns for $\mathcal{A} = 0.280$ and 0.300 , which are not shown in figure 5.7, contain a cusped deltoidal line with the cusps directed toward rather than between the atomic strings defining the channel. Thus, the increase of \mathcal{A} away from the value of 0.250 induces the joining of the two cusped triangular rainbow lines into the cusped deltoidal line (with the cusps directed toward rather than between the atomic strings defining the channel). As in figure 5.4, the inner sides of all these lines are the bright sides of the rainbows while their outer sides are the dark sides of the rainbows.

If the evolution of the rainbow pattern in the transverse position plane with \mathcal{A} given in figure 5.7 is compared with the corresponding evolution for $\varphi = 0$ presented in [79], one can see that the cusped rectangular line, the two cusped triangular lines and the cusped deltoidal line appearing in the former case for $\mathcal{A} = 0.20, 0.25$ and 0.30 correspond to a cusped square line, a point and a cusped square line in the latter case, respectively. Also, in the case when $\varphi = 0.10\psi_c$, centers of the rainbow patterns are displaced from the origin, the displacement increasing with \mathcal{A} , and in the case when φ

$= 0$, they coincide with the origin. This is in accordance with the corresponding dependences shown in figure 5.6.

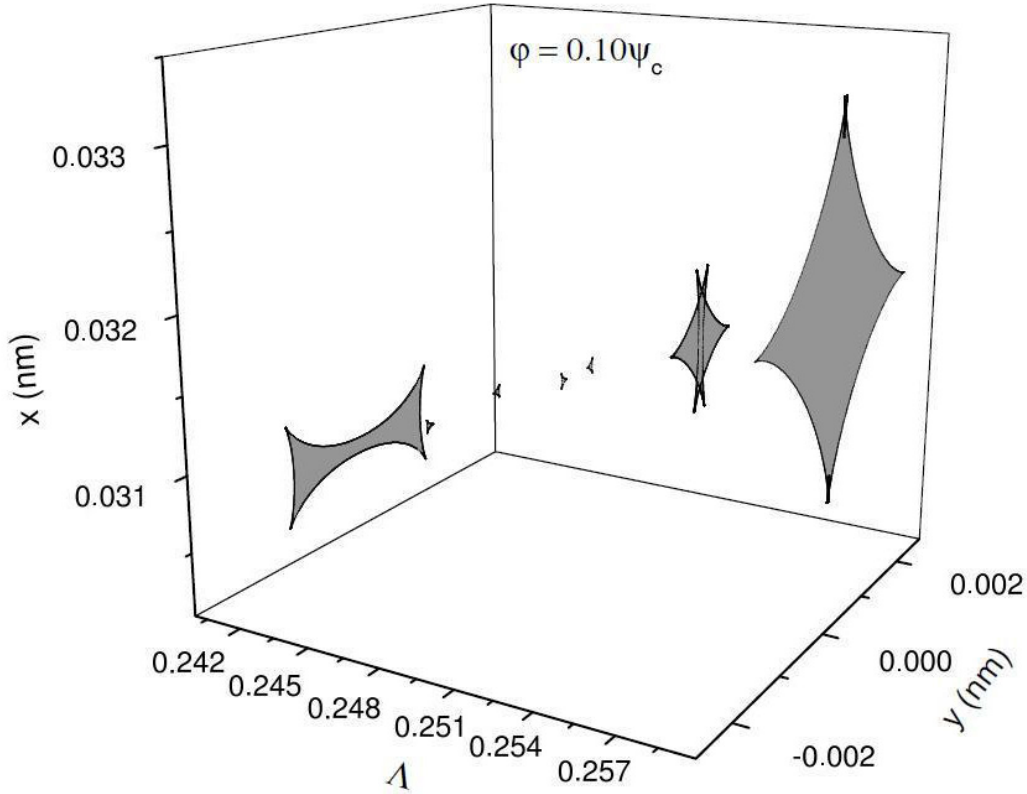


Figure 5.7: The evolution of the rainbow pattern in the transverse position plane with the reduced crystal thickness in the vicinity of the superfocusing point, for $A = 0.240, 0.245, 0.250, 0.255$ and 0.260 , corresponding to the crystal thicknesses $L = 79.3, 81.0, 82.6, 84.3$ and 85.9 nm, for the proton beam incident angle $\varphi = 0.10\psi_c$, see text above.

To summarize, this chapter presents theoretical analysis of the superfocusing effect of 2 MeV protons in a $\langle 100 \rangle$ Si crystal channel. The considered range of the reduced crystal thickness, A , is around 0.25, i.e., in the vicinity of the superfocusing point. The corresponding value of the crystal thickness is 82.6 nm. The superfocusing effect has been analyzed for the proton beam incident angles, φ , between 0 and $\pm 0.20\psi_c$, with ψ_c being the critical angle for channeling.

It has been shown that each of the spatial distributions of channeled protons for $\varphi = 0$, $\pm 0.05\psi_c$, $\pm 0.10\psi_c$ and $\pm 0.15\psi_c$ and $\mathcal{A} = 0.25$ has one strong and narrow maximum. These maxima are due to the superfocusing effect, which is explained by the dominance of the harmonic component of the continuum proton-crystal interaction potential over its anharmonic component in the region close to the channel axis. The displacements of these maxima from the origin are below a_0 . Each of the distributions for $\varphi = \pm 0.20\psi_c$ has two maxima, whose displacements from the origin are above a_0 . The rainbow patterns corresponding to all these distributions consist of two cusped triangular lines. For $\varphi = 0$ these two rainbow lines come to a point.

Also, we have elaborated further the idea to employ the superfocusing effect for subatomic microscopy. The system under consideration has been a foreign atom, being a sulfur atom, inserted in the channel near the superfocusing point and exposed to the proton beam.

Chapter 6

Quantum entanglement and spin control in silicon nanocrystal

In this chapter selective coherence control and electrically mediated exchange coupling of single electron spin between triplet and singlet states using numerically-derived optimal control of proton pulses is demonstrated. Spatial confinement below size of the Bohr radius for proton spin chain FWHM is obtained. Precise manipulation of individual spins and polarization of electron spin states are analyzed via proton induced emission and controlled population of energy shells in pure ^{29}Si nanocrystal. Entangled quantum states of channeled proton trajectories are mapped in transverse and angular phase space of ^{29}Si $\langle 100 \rangle$ axial channel alignment in order to avoid transversal excitations. Proton density and proton energy as impact parameter functions are characterized in single particle density matrix via discretization of diagonal and nearest off-diagonal elements. We combined high field and low densities (1 MeV/92 nm) to create inseparable quantum state by superimposing the hyperpolarized proton spin chain with electron spin of ^{29}Si . Quantum discretization of density of states (DOS) was performed by the Monte Carlo simulation method using numerical solutions of proton equations of motion. Distribution of gaussian coherent states is obtained by continuous modulation of individual spin phase and amplitude. Obtained results allow precise engineering and faithful mapping of spin states, which can provide the effective quantum key distribution (QKD) and transmission of quantum information over remote distances between quantum memory centers for scalable quantum communication network. Furthermore, obtained results give insights in application of channeled protons subatomic microscopy as a complete versatile scanning-probe system capable of both quantum engineering of charged particle states and characterization of quantum states below diffraction limit linear and in-depth resolution.

6.1 Introduction

Major progress of experimental techniques as well as theoretical models during the last few decades, has made possible the comprehensive analysis of the ion beams collision dynamics [64, 93]. Obtained results have facilitated development of versatile analytical instruments which can provide material characterization, modification and analyses [72, 94] over a wide range of scientific disciplines. In addition, focused ion beam techniques beyond sub-nanometer scale [71, 74, 95-97] have gained an important role as silicon based nano-domain engineering [98-100] has become one of the most important tool in materials research, low dimensional system electronics, semiconductor manufacturing and nanotechnology overall. Recent experimental investigations of quantum information processing via single electron devices in gate defined quantum dots [101, 102] confirm silicon based spin quantum-information processor as a promising candidate for future quantum computer architectures [10]. In that context series of investigations of electrically [103-105] and optically [106] induced ion kinetics in solid state quantum systems reveal that focusing of coherent ions through oriented crystal, may enhance precise confinement and manipulation of individual spins in quantum information processing [37, 107]. The most prominent recent results relating the spin dynamics control to ion channeling techniques in thin crystals presented in series of theoretical studies [20, 79, 108, 109] when the ion differential cross section is singular [110] give opportunity for precise manipulation of intrinsic properties of charged particles.

6.2 The logarithmic singularity under continuum approximation

For transverse energy $E_{\perp} < E\varphi$ and the ion beam incident angle $\varphi \ll \psi_c$, φ and ψ_c denote critical angle for channeling and effective ion atom potential, respectively.

The effective potential area $\gamma(A_0(E_{\perp}))$ which corresponds to maximal enhancement in ion flux density includes strictly harmonic terms under continuum approximation

$$\gamma(A_{i_0}) \approx \int_{A_{\min}}^{A_{\max}} \frac{dA}{A_{i_0} - (\pi E \varphi^2)/k} \approx \ln \left| \frac{A_0}{A_{i_0} - (\pi E \varphi^2)/k} \right|, \quad (6.1)$$

where A_{i_0} denotes the equipotential surface closed by field contour in the central part of the axial channel. The corresponding integration boundaries are:

$$A_{\min} = A_{i_0} - \frac{\pi E \varphi^2}{k} \text{ and } A_{\max} = A_0 - A_{i_0} - \frac{\pi E \varphi^2}{k}. \quad (6.2)$$

$A_0 = \pi S_0^2 \alpha^{-1}$ and $A_i = \pi \rho_{cm}^2 \alpha^{-1}$ denote demarcation line of the channel cross-section area. The central part of the axial channel is then represented by the annulus of inner

$$\text{radius } S_0 = (\pi N d)^{-1} = \sqrt{\left(\frac{d}{2}\right)^2 + \alpha \rho_c^2}, \quad (6.3)$$

where d , ρ_c and α represent the mean spacing between the atomic rows, ion impact parameter and the ratio of total axial channels number versus number of atomic rows forming the channel, respectively.

Accordingly to equations (1.31), when the ion beam incident angle is close to zero $\varphi \cong 0$, the anisotropy for central part of axial channel is induced only by harmonic component of the interaction potential. This implies that first equipotential circle represents dominant effective potential area for ion flux density denoted as $\gamma(A_{i_0}(E_{\perp}))$.

Hence, the area of maximal enhancement in ion flux density is confined to central equipotential curve of axial channel $\gamma(A_{i_0}) \approx \ln \left| \frac{A_0 k}{\pi E \varphi^2} \right|$ and further converges to zero

as $A_{i_0} \rightarrow 0$ if the incident angle, i.e. the tilt angle of the beam, corresponds to condition

$\varphi = \sqrt{(A_{i_0} k / \pi E)}$. The results obtained for MeV proton beam energies show the nonequilibrium density of states across central part of the channel as nonuniform flux redistribution. This reveals the strong effect of anharmonic components in effective continuum interaction potential even in vicinity of low index crystal axis for $\langle 100 \rangle$ Si.

In this part of the thesis I present theoretical study of localization and coherent control by superfocused channeled protons, CP beam induced polarization of individual electron spins in pure ^{29}Si nanocrystal. We analyze precise control of entangled proton trajectories and discrete quantum states of phase space in connection to selective spin manipulation. The harmonic motion of highly correlated channeled protons is tuned by external RF field, by varying the CP energy and tilt angle relative to main $\langle 100 \rangle$ crystal axis. The calculations include the quasiharmonic approximation as well as the effect of multiple scattering by valence electrons and assume the anharmonicity of the interaction potential [110, 111]. Quantum entanglement of focused ion trajectories in final states corresponds to central part of the $\langle 100 \rangle$ Si axial channel. It is analyzed in phase space by convoluted transfer matrix method [112].

According to Liouville's theorem [113], the ensemble of channeled particles (for large impact parameters) experiences series of correlated, small angle collisions in initial stage of elastic interaction with atoms of the crystal lattice. Therefore, a proton flux distribution can be calculated via probability function of quantum trajectory reversibility, i.e., the probability for appearing of backscattered particles along initial propagation direction. The resultant flux distribution further considers unnormalized probability map of trajectories of channeled particles in phase space. We have analyzed the nonequilibrium state of channeled protons density profiles in configuration and scattering angle plane in connection to anharmonic expansion terms of proton - crystal effective potential. Calculation assumes the initial state of static equilibrium, considering 92 nm crystal's length and channeling conditions which correspond to infinitesimal crystal tilt angles, from zero up to 20% of critical angle for channeling. Degree of correlation between separate trajectories of channeled protons was calculated by two separate mapping procedures between configuration and angular phase plane. Thus, the nonharmonic-higher order terms of continuum interaction potential were analyzed via distribution function of channeled protons in transverse position plane and scattering angle plane.

The subsequent chapters are organized as follows.

Section 6.3 following the recent experimental attempts to realize electron spin processor in silicon capable of quantum information processing introduces quantum model for excitation and coherent control of electron spin states via entangled proton trajectories. Exchange coupling is analyzed under quasiharmonic approximation of interaction potential taking into account the constraint of singular proton flux density. The theoretical model is further explained by Molière approximation of the Thomas-Fermi interaction potential. This formalism comprises Liouville's theorem to give simple explanation for mapping procedures for proton beam transformation matrix in configuration and angular phase space. Section 6.4 explains numerical model and simulation parameters. Section 6.5 compares and discusses profiles of proton density distributions for transverse position plane (configuration space) and scattering exit-angle plane (angular space), gives the evolution of proton fluxes with various tilt angles and further illustrates comparative analysis of proton trajectories mapped in six dimensional phase space considering several Λ and φ variables in effective ion - crystal anharmonic potential. Mapping procedure for entangled proton trajectories is further obtained considering localization, selective excitation and unitary transformations of singlet/triplet spin states in quantum phase space.

6.3 Quantum model of the superfocusing effect for excitation and coherent control of electron and nuclear spin states

Coherent manipulation and precise control of single electron spin rotation represents first step toward quantum information processing (QIP) [37, 114]. In order to achieve high level of precision of single electron spin unitary rotations we propose highly correlated spin chain of superfocused protons as a direct probe method for induction of local electron spin excitations in silicon. In this context propagation of the single spin excitation as a procedure for quantum state entanglement [115] can be intermediated via mixed quantum state between channeled protons (CP) spin system and induced coherent oscillations of electron spin system in silicon. In spin-lattice system, the condition of conservation of transverse energy when CP have equal probability to access any point of physical area corresponding to the channeling conditions, i.e., reaching the state of

statistical equilibrium, has been modified by Barrett factor [116]. This constraint explains simultaneous existence of equilibrium particle distribution and population enhancement in different fractions of the phase space volume in process of ion transmission through media of sufficient small length. As a result, phase space distributions of CP in separate non-equipotential areas of the channel exhibit fractal characteristics over total phase space volume. We have investigated the proton flux profile in scattering angle plane and transverse position plane. The boundary conditions of nonuniform density distributions are analyzed in case of small impact parameters along main $\langle 100 \rangle$ Si crystal axis. The obtained results show that enhancement effect of channeled protons flux bijectively corresponds to flux maxima in coordination space. In that sense we have analyzed degree of anisotropy including the anharmonic, higher order terms, k^i , $i \leq 4$, in effective continuum interaction potential. As a result, the channeled proton (CP) induced transition frequency ω between two electronic states includes higher order contributions

$$\hbar\omega = \hbar\omega - \frac{1}{2}|E_{\perp}(r, \varphi, \Lambda)|^2 (\alpha_2(\lambda, \varphi) - \alpha_1(\lambda, \varphi)) + O^{n \leq 4} \quad (6.21)$$

E_{\perp} represents the effective transverse energy of induced CP - electron system interaction.

(a)

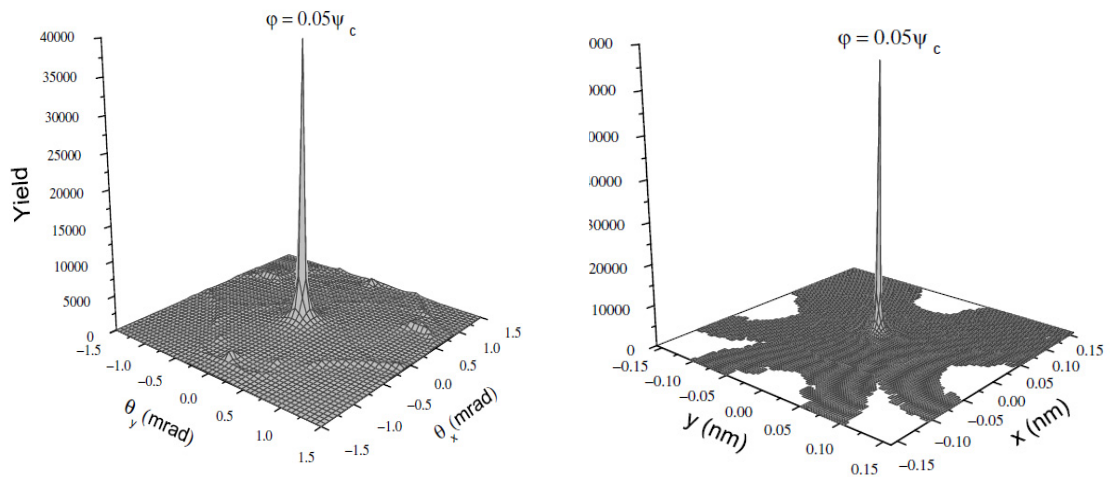
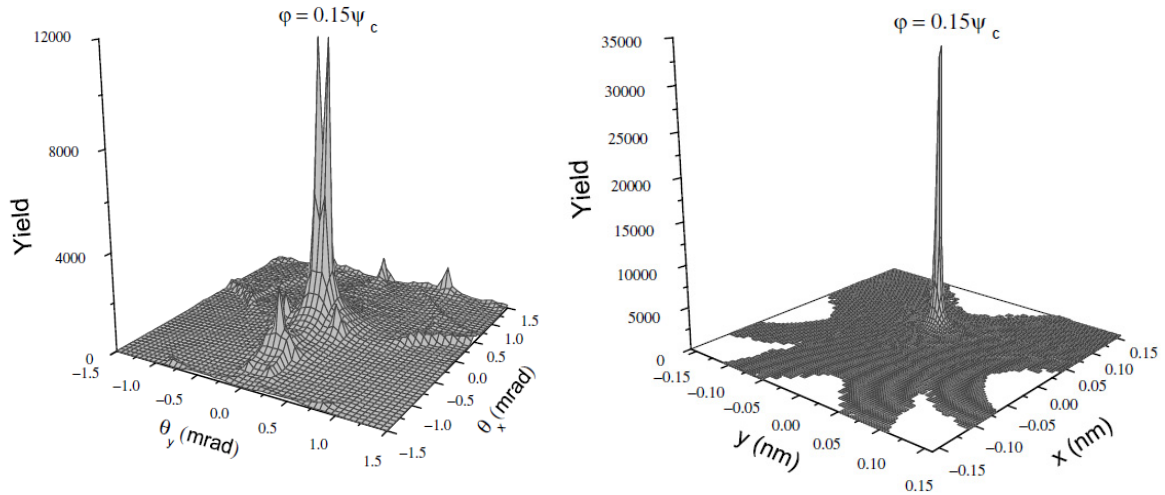


Figure 6.1: (a) 3-d density distribution profiles of channeled protons. The quantum trajectories are compared in angular scattering plane (left), $L = 286$ nm and transverse position plane (right), $L = 82.6$ nm. The chosen tilt angle is $\varphi = 0.05\psi_c$ (a).

(b)



(c)

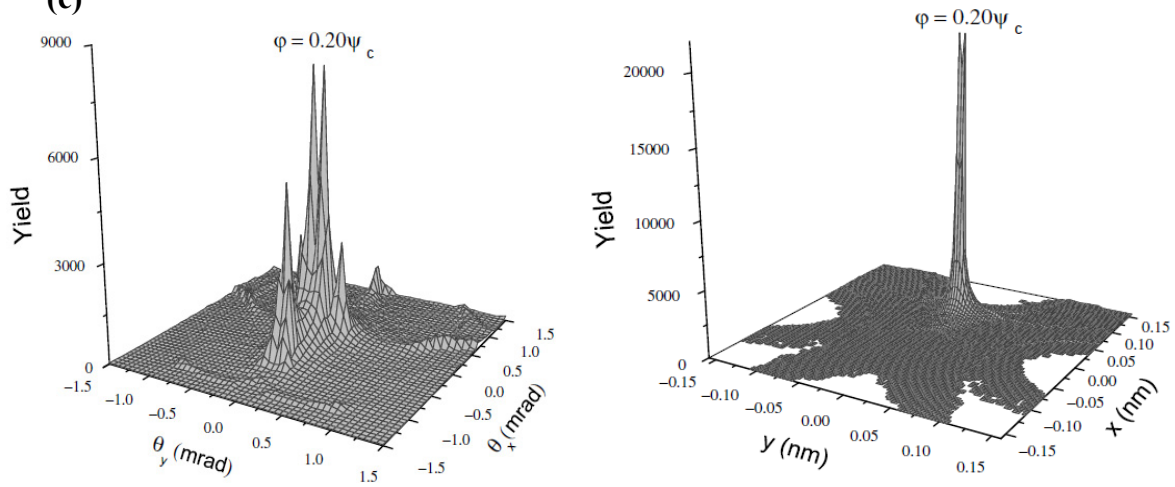


Figure 6.1: (b, c) 3-d density distribution profiles of channeled protons. The quantum trajectories are compared in angular scattering plane (left), $L = 286$ nm and transverse position plane (right), $L = 82.6$ nm. The chosen tilt angles are $\varphi = 0.15\psi_c$ (b) and $\varphi = 0.20\psi_c$ (c).

The corresponding Hamiltonian of rotating frame system [31] is

$$\begin{aligned} H_s &= \Omega S_z + \omega_l I_z + A S_z I_z + B S_z I_z, \\ \Omega &= \omega_s - \omega, \quad \omega_s = g \beta_e B_o / \hbar, \quad \omega_l = -g_n \beta_n B_o / \hbar. \end{aligned} \quad (6.22)$$

Ω represents CP perturbed electron Zeeman frequency, β_e and β_n denote the Bohr and nuclear magneton respectively, S_z and I_z are electron and nuclear spin operators, g and g_n are electron and nuclear effective g factors, ω_s and ω_l denote electron and nuclear Zeeman frequency respectively (nuclear frequency for spin up polarization $\omega_{l\uparrow} = 11.99$ and nuclear frequency for spin down polarization $\omega_{l\downarrow} = 36.35$), A and B are secular and pseudosecular hyperfine couplings terms, respectively, \hbar is reduced Planck constant, B_o is static magnetic field along z-axis. Under static magnetic field the singlet $|S\rangle$ and polarized triplet $|T_{0,\pm}\rangle$ are degenerate, nearly independent. As a result, the quantum state of system ρ in rotating frame corresponds to position of spin down polarized axis (bottom half of the Bloch sphere) as $\rho \otimes |0\rangle\langle 0| \otimes U$, likewise the polarized spin up axis position (top half of the Bloch sphere) denotes $\rho \otimes |1\rangle\langle 1| \otimes U$, where U (eq. (6.30)) couples additional degrees of freedom to initial quantum state, i.e. it represents the transformation matrix of mixed quantum state under CP polarization. In finite magnetic field, the CP perturbed electron Zeeman frequency for external field up to 1 MeV allows decorrelation of longitudinal Overhauser field B_z and shifts the level of singlet spin-down configuration from the ground into the excited $S|T_0\rangle$ and $S|T_+\rangle$ state. This coherent superposition of system energy levels (1, 0) and (0, 1) with triplet state (1, 1) is consistent with dipole-dipole mediated nuclear diffusion and leads to periodic superposition of spin states with precession period on a 1s time scale assuming that Overhauser fields $B = (\Delta B_x, \Delta B_y, B_z)$ are Gaussian distributed on long time scales. Thus, the external field close to 1 MeV is large enough to cause the strong spin dependency of tunneling effect. Large field produces strong asymmetry for spin up and spin down charge energy. It is important first to establish a non-zero external magnetic field B so that each of nuclear spin principle axis orientations can be effectively

optimized. This produces efficient coupling of longitudinal component of electron spins to quantized transverse component of nuclear spins. Thus, the quantized nuclear spin states are mediated via anisotropic part of the hyperfine interaction, i. e. the universal control of the nuclear spin state is achieved via unitarily transformed term, $BS_z I_z$ [117].

Namely, up to 1 MeV the external field induces coupling of nonparallel nuclear spin quantization axis to electron spin states and it allows the anisotropic pseudosecular term for universal control, otherwise the pseudosecular term is suppressed. Hence, adding a stronger external field to the quartic potential (eq. (6.21)), alters the potential minima and changes confinement energies of orbital wave states which in turn induces a DOS transition from absolute equilibria to saddle point in phase space.

Instead of applying the oscillating RF field to spatially resolve and manipulate spin resonance frequencies (or in order to measure response of the quantum dot by current flowing through the dot or by near quantum point), the induced transition can be generated upon CP excitation of the spin system. Thus, excited spin system displaces the center of the electron wavefunction along the oscillating superfocused CP field direction and change its potential depth. As a result the electron wavefunction frequency can be spatially distorted in order to coincides/shifts with applied CP field.

A single spin excitation is then polarized along z axis coinciding with proton beam alignment. In addition, the resultant mixed state conserves the total angular momentum of the exchange Hamiltonian along z axis:

$$[H_{ech}; Z] = 0, \quad Z = \sum_{j=1}^n \sigma_z^j \quad (6.23)$$

This allows diagonalization of the system Hamiltonian into subspaces of excited spins, i.e. the spin ensemble along σ_z basis, corresponds to degenerate Z eigenvalues. The effective single spin read out [118] can be further realized by electrical detection of spin recharge events in tunneling proximity to a metal by adjustment of the Fermi level between two initially split electron eigenstates (corresponding to spin-up and spin-down orientation). Excitations of electron spin localized below Fermi threshold causes

electron tunneling and leaving of initially occupied eigenstate. Discharged, empty spin state below Fermi level is further filled by an electron with oppositely oriented spin.

In present case, numerical solutions of entangled proton trajectories, for different reduced crystal thicknesses and tilt angles, correspond to short range correlated proton - lattice interaction potential in vicinity of $\langle 100 \rangle$ Si axis.

6.4 Mapping of quantum states, transformation matrix and mixed coupling induced by superimposed CP field

The interaction between the proton and the crystal's atoms includes elastic collisions, assuming classical, small-angles model of channeling [59, 64]. For the zero φ angles, the z -axis coincides with $\langle 100 \rangle$ Si crystallographic axis, while the atomic strings which define the channel cover the x and y axis. The initial proton velocity vector \mathbf{v}_0 is collinear with the z axis.

We have modeled the system considering the Lindhard continuum approximation for axial channeling [64]. The crystal interaction potential comprises the continuum potentials of separate atomic strings. Hence, we have included the thermal vibrations of the crystal's atoms:

$$U_i^{th}(x, y) = U_i(x, y) + \frac{\sigma_{th}^2}{2} [\partial_{xx} U_i(x, y) + \partial_{yy} U_i(x, y)], \quad (6.24)$$

where $U_i(x, y)$ represents the continuum potential of the i th atomic string, xy are transverse components of the proton position, and σ_{th} is the one-dimensional thermal vibration amplitude.

The specific electronic energy loss is determined by equation

$$-\frac{dE}{dz} = \frac{4\pi Z_1^2 e^4}{m_e v^2} n_e \ln \frac{2m_e v^2}{\hbar \omega_e}, \quad (6.25)$$

where v is the proton velocity, m_e is the electron mass, $n_e = \frac{\Delta U^{th}}{4\pi}$ is the density of the crystal's electrons averaged along the z axis and $\Delta \equiv \partial_{xx} + \partial_{yy}$.

The angular frequency of the electron oscillation induced by the channeled proton is

$$\omega_e = \left(\frac{4\pi e^2 n_e}{m_e} \right)^{\frac{1}{2}} \quad (6.26)$$

The mean-square angular deviation of the proton scattering angle caused by its collision with the electrons is included as

$$\frac{d\Omega}{dz} = \frac{m_e}{2m_p E} \left(-\frac{dE}{dz} \right) \quad (6.27)$$

In the above equation m_p denotes the proton mass and E is the proton energy.

Further calculations take into account the proton beam divergence before its interaction with the crystal [20, 79].

The quantum Monte Carlo simulation method has been used for parameterization of entangled proton trajectories. Obtained numerical solutions of channeled protons equations of motion correspond to their angular and spatial distributions. The phase space density, according to the Liouville's theorem, cannot be changed in conservative system, but one can manipulate with the form and position of the phase space elements. We can use the phase space transformations to improve the channeling efficiency.

Discrete map of quantum states of channeled proton trajectories, their point transformation in the spatial (transverse) and angular phase space are presented in the following vector basis

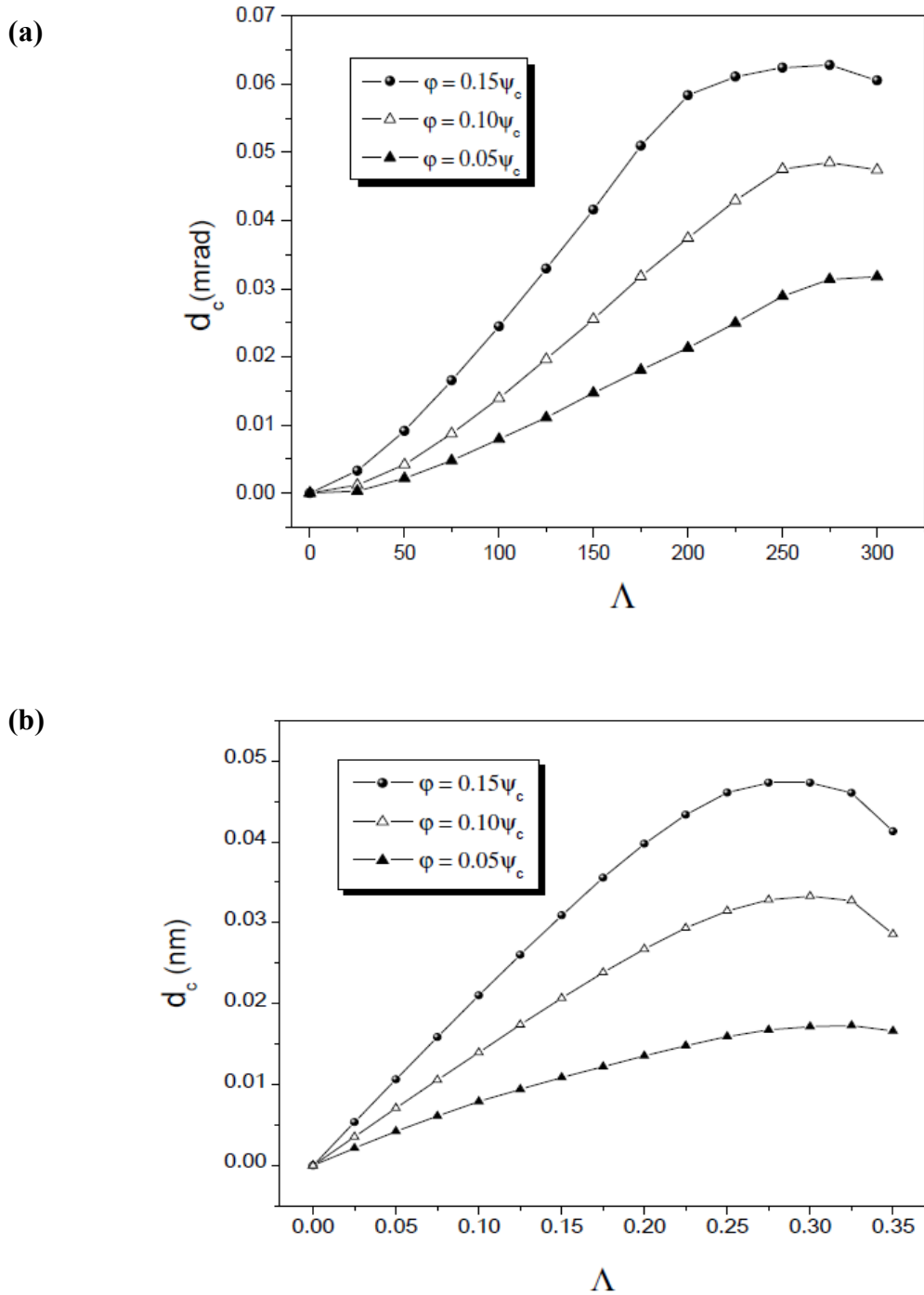


Figure 6.2: (a, b) The calculated positions of channeled protons yield maxima. Angular and spatial yield dependences correspond to area of reduced crystal thicknesses between 0.00 and 300.0, $L = 1.69 \mu\text{m}$ (a) and 0.00 and 0.300, $L = 99.2 \text{ nm}$ (b), respectively. The chosen tilt angles relative to Si $\langle 100 \rangle$ axis are $\varphi = 0.05\psi_c$, $\varphi = 0.10\psi_c$ and $\varphi = 0.15\psi_c$.

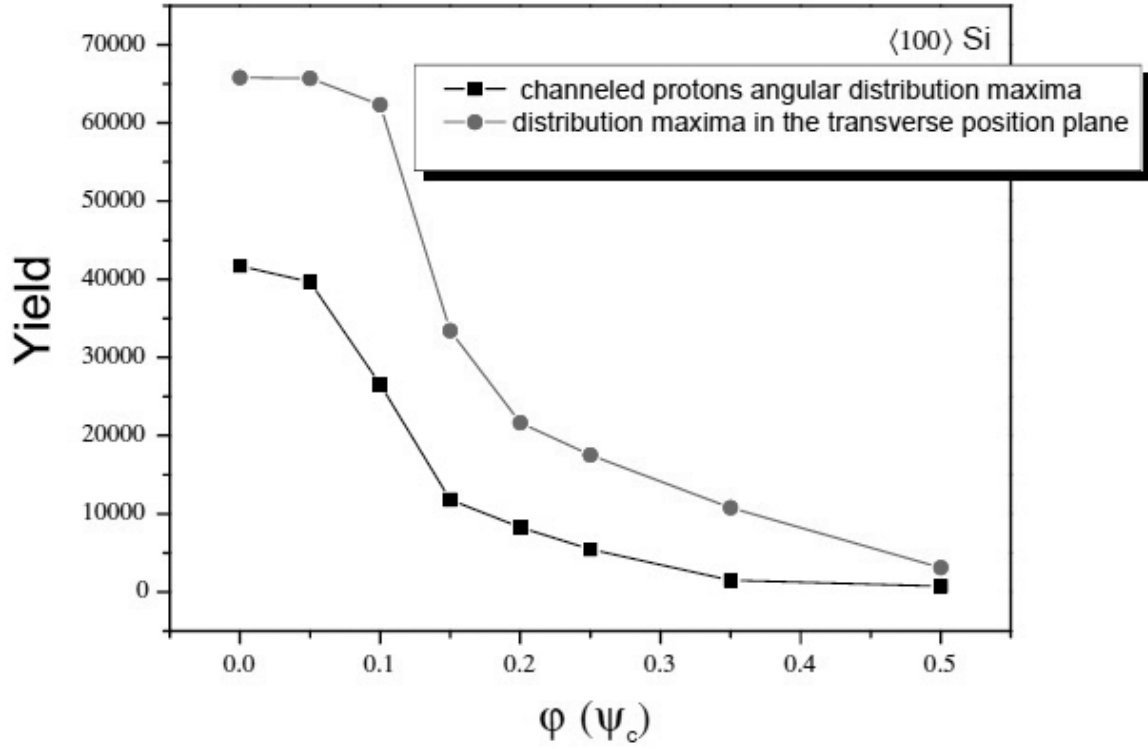


Figure 6.3: Numerical simulation of proton quantum trajectories (axial yields) and calculated slope of coupling energy $J(\varepsilon)$. The dependence of exchange coupling energy $J(\varepsilon)$ is compared in angular phase plane (designated by solid squares) and transverse position phase plane (marked by solid circles). The chosen tilt angles correspond to range between $\phi = 0.00$ and $\phi = 0.5\psi_c$. The value of reduced crystal thicknesses is fixed to $\Lambda = 0.25$ in configuration space, i.e. $\Lambda = 0.50$ in angular space.

$$\begin{pmatrix} x \\ y \\ x' \\ y' \\ \Lambda \\ \varphi \end{pmatrix} \rightarrow \begin{pmatrix} x \\ y \\ \theta_x \\ \theta_y \\ \Lambda \\ \varphi \end{pmatrix} \quad (6.28)$$

Here Λ and φ denote the crystal reduced length and tilt angle of CP beam.

Although the phase space is six dimensional we consider four subspaces of the transverse and angular phase space.

Correspondingly, the mapping of beam parameters and quantum discretization of entangled states is conformally rescaled through phase space transfer matrix \mathbf{M} (4x4): $\mathbf{M} \rightarrow \tilde{\mathbf{M}}$. In that sense we consider local symplectic condition for the realizable transfer matrix of the Hamiltonian system

$$\tilde{\mathbf{M}}\mathbf{M} = \mathbf{M}\tilde{\mathbf{M}} = J, J = \begin{pmatrix} J_{2D} & 0 \\ 0 & J_{2D} \end{pmatrix}, J_{2D} = \begin{pmatrix} 0 & 1 \\ -1 & 0 \end{pmatrix}. \quad (6.29)$$

Tilde sign denotes the transpose operation over transfer matrices and \mathbf{J}_{2D} refers to unit symplectic matrix in 2-d phase space volume.

According to the Liouville's theorem the conservation of the phase space volume results from the statement: $\det \mathbf{M}=1$, following the equation (6.29).

Complete characterization of the phase space volume is achieved over the second order moments of transfer beam matrices:

$$\Sigma(X) = \langle X\tilde{X} \rangle = \begin{pmatrix} \langle x^2 \rangle & \langle x'x \rangle \cdots & \langle \varphi x \rangle \\ \langle xx' \rangle \ddots & & \vdots \\ \vdots & \ddots & \\ \langle x\varphi \rangle \cdots \cdots & & \langle \varphi^2 \rangle \end{pmatrix}, \Sigma(\mathcal{G}_X) = \langle \mathcal{G}_X \tilde{\mathcal{G}}_X \rangle = \begin{pmatrix} \langle x^2 \rangle & \langle \theta_x x \rangle \cdots & \langle \varphi x \rangle \\ \langle x\theta_x \rangle \ddots & & \vdots \\ \vdots & \ddots & \\ \langle \theta_x \varphi \rangle \cdots \cdots & & \langle \varphi^2 \rangle \end{pmatrix}, \quad (6.29a)$$

$$\Sigma(Y) = \langle Y\tilde{Y} \rangle = \begin{pmatrix} \langle y^2 \rangle & \langle y'y \rangle \cdots & \langle \varphi y \rangle \\ \langle yy' \rangle \ddots & & \vdots \\ \vdots & \ddots & \\ \langle y\varphi \rangle \cdots \cdots & & \langle \varphi^2 \rangle \end{pmatrix}, \Sigma(\mathcal{G}_Y) = \langle \mathcal{G}_Y \tilde{\mathcal{G}}_Y \rangle = \begin{pmatrix} \langle y^2 \rangle & \langle \theta_y y \rangle \cdots & \langle \varphi y \rangle \\ \langle y\theta_y \rangle \ddots & & \vdots \\ \vdots & \ddots & \\ \langle \theta_y \varphi \rangle \cdots \cdots & & \langle \varphi^2 \rangle \end{pmatrix}. \quad (6.29b)$$

The beam matrix transform as

$$\Sigma \rightarrow M\Sigma\tilde{M}, \quad (6.29c)$$

$$I' = -1/2Tr(\Sigma J \Sigma J), \sigma_4 = \det(\Sigma), \quad (6.29d)$$

where matrix trace, Tr and value σ_4 , i.e. the phase space volume occupied with the proton beam, determines the two invariants of the transfer beam matrix. We reduce

system dimensionality by decoupling the 4-d phase space on 2-d: configurational ($x-y$) and angular, $(\theta_x - \theta_y)$ phase space. The transformation matrix describing the mixed quantum ensemble then couple a diagonal S_X basis of electron spin system to diagonal S_Z basis [119] of fully polarized superfocused CP beam and forms a nonorthonormal basis

$$U = \sum_r |\Sigma^r\rangle \langle a^r|. \quad (6.30)$$

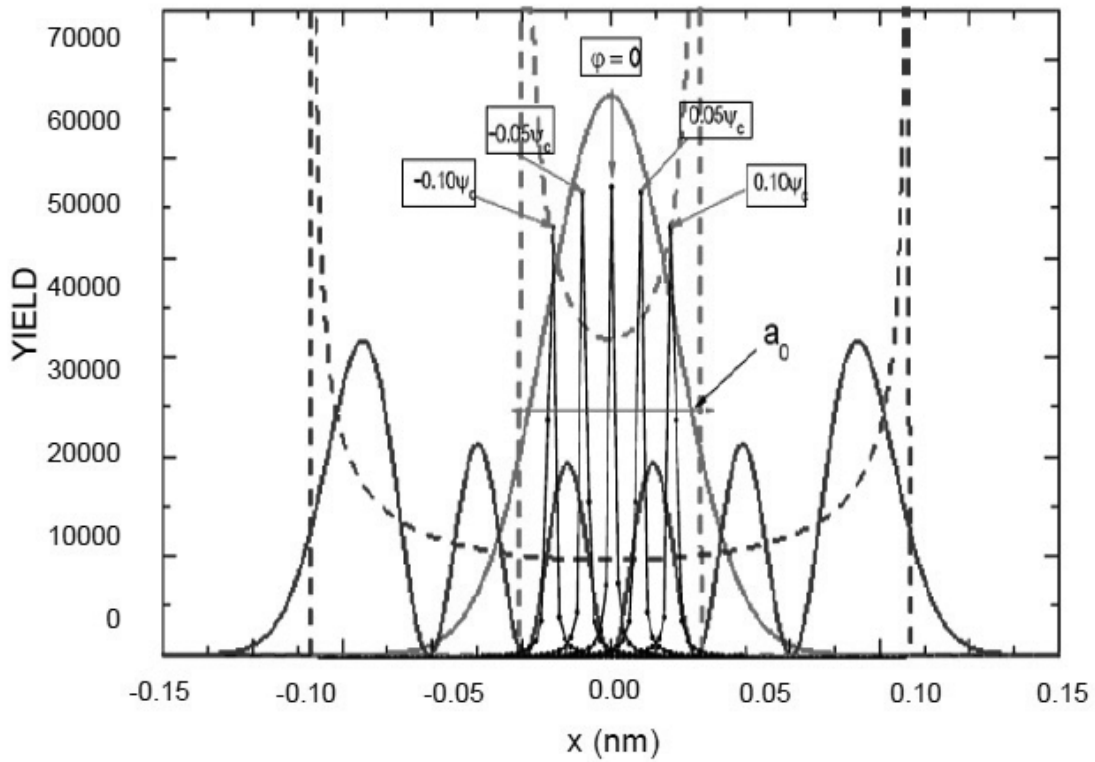


Figure 6.4: Quantum localization of single electron wave functions inside area of hydrogen ground state induced by CP field. The chosen tilt angles are $\phi = 0.05 \psi_c$, $\phi = 0.10 \psi_c$ and $\phi = 0.15 \psi_c$ for $L = 57.82$ nm in Si nanocrystal. The effect of quartic anharmonic terms in the exchange interaction initiates transition to triplet states.

Basis $|\Sigma^r\rangle = \sum_{nm} \alpha_{nm} e^{-i\epsilon_{nm}t} |nm\rangle$ denotes the stationary, $|nm\rangle$ quantum state of electron system with amplitude α_{nm} , energy ϵ_{nm} and quantum numbers n, m .

Under CP interaction $i\rho(\alpha_{nm}) = \sum_{n'm'} \langle nm|U|n'm'\rangle e^{i(\epsilon_{nm}-\epsilon_{n'm'})t} \alpha_{n'm'}$ denotes energy splitting between ground and excited electron states, $|n'm'\rangle$, of the target and the projectile.

In order to determine the matrix elements of CP - lattice confinement potential for singlet and triplet functions we use two single electron eigenstates denoted by spatial electron-wave functions $|X\rangle$ and $|X'\rangle$ as

$$|S\rangle = |\uparrow\downarrow\rangle - |\downarrow\uparrow\rangle \otimes \begin{pmatrix} 1/\sqrt{2}(|XX'\rangle) \\ 1/2(|XX'\rangle + |X'X'\rangle) \end{pmatrix}, \quad |T_{0,\pm 1}\rangle = \begin{cases} 1/2(|XX'\rangle - |X'X'\rangle) \otimes |\uparrow\downarrow\rangle + |\downarrow\uparrow\rangle \\ 1/\sqrt{2}(|XX'\rangle - |X'X'\rangle) \otimes |\uparrow\uparrow\rangle \\ 1/\sqrt{2}(|XX'\rangle - |X'X'\rangle) \otimes |\downarrow\downarrow\rangle. \end{cases}$$

The energy splitting between triplet, $|T_0\rangle$ and ground singlet state, $|S\rangle$ is denoted by exchange interaction, $J = \langle T_0|i\rho(\alpha_{nm})|T_0\rangle - \langle S|i\rho(\alpha_{nm})|S\rangle$. (6.31)

The Hamiltonian is further diagonalized in singlet and triplet subspaces. In order to overcome high level truncation of the basis, where linear combinations of two electron states tends to infinity, we use constraint that singlet state refers to ground state according to Lieb Mattis theorem [120] in zero magnetic field.

Applying the inhomogeneous CP field along main crystal axis, i.e., involving x and y phase space components of tilted CP beam, if the energy difference of triplet and singlet electron states is close, they became strongly mixed. The triplet $|T_0\rangle$ can evolve into the singlet state $|S\rangle$ as

$$1/2(|XX'\rangle - |X'X'\rangle) \otimes |\uparrow\downarrow\rangle + |\downarrow\uparrow\rangle \rightarrow |\uparrow\downarrow\rangle - |\downarrow\uparrow\rangle \otimes 1/2(|XX'\rangle + |X'X'\rangle). \quad (6.32)$$

Likewise, $|T_+\rangle$ and $|T_-\rangle$ evolve into singlet state. As explained in the main text the mechanism of spin excitation and energy separation scheme, (illustrated in figure 6.5), between the ground singlet state and the polarized triplet state is controlled by a combination of a CP initial energy E (φ , Λ) and tilt angle φ . Upon the excitation energy is applied to the quantum dot inside the Bohr radius, it is shown that spin system energy cost for adding an extra electron starts from state S (0, 1), as indicated by dotted black

line, where (n, m) $J(\varepsilon)$ and E_{ST} denote the charge state with n and m electrons, exchange and splitting energy, respectively. The energy cost for reaching $(1, 1)$ is (nearly) independent of the spin configuration.

However, the energy cost for forming a singlet state $S(0, 2)$ is much lower than that for forming a triplet state (not shown in the diagram). This difference can be further exploited for spin initialization and detection.

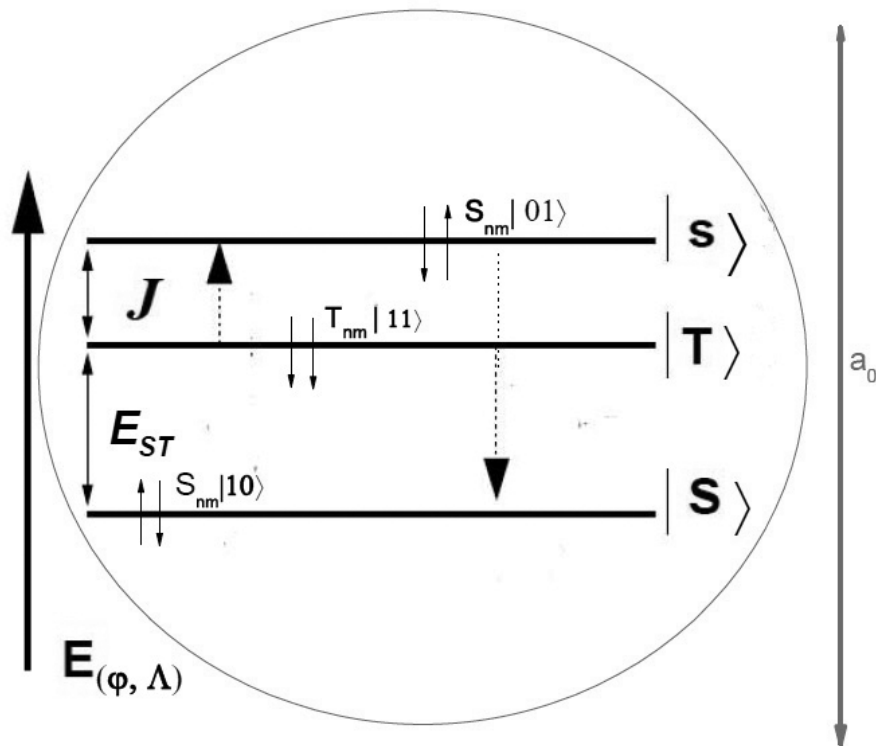


Figure 6.5: Scheme of excitation/splitting energy and exchange couplings inside area of Bohr radius. Energy diagram shows tunneling effect between ground singlet state and $|T\rangle$ polarized, triplet state, so that different superposition states can be realized.

6.5 Numerical methods and simulation model

Simulation model considers cubic unit cell representation of the isotopically pure ^{29}Si nanocrystal. It includes atomic strings on three nearest square coordination lines of

the $\langle 100 \rangle$ axial channel [20, 79, 83, 85]. According to diamond lattice symmetry, the orthogonal mesh is projected across the channel, mapping two layers of 2×2 triangular areas of $\langle 100 \rangle$ unit cell.

The proton trajectories are generated from the sequences of binary collisions via the quantum Monte Carlo simulation method using the screened Molière interaction potential. Considering 2 T magnetic field, the crystal is tilted in angular space along the axis $\theta_x = 0$ ($x = 0$), where the value of the tilt angle ranges up to 20% of the critical angle for channeling, $\psi_c = [2Z_1Z_2e^2/(dE)]^{1/2} = 6.09$ mrad. Numerical calculations consider the continuum model in the impulse approximation.

The motion of ions in the continuum model is determined by the Hamiltonian

$$H = (1/2)m(p_{\perp}^2 + U(r)) = E(\psi_x^2 + \psi_y^2) + U(r), \quad (6.33)$$

$$E_{\perp} = E\psi^2 + U(r), \quad (6.34)$$

where ψ_x and ψ_y denote x and y projection of scattering small angle with respect to the $\langle 100 \rangle$ axis. The systems ion-atom interaction potential is obtained by integration of the Molière approximation of the Thomas-Fermi interaction potential [59].

$$U_i(r) = \frac{2Z_1Z_2e^2}{d} \sum_{i=1}^3 \alpha_i K_0 \left(\beta_i \frac{r}{a} \right). \quad (6.35)$$

Z_1 and Z_2 denote the atomic numbers of the proton and the atom, respectively, e is the electron charge, d measures quantum displacement of single particle wave function relative to harmonic oscillator central position in ground state, r is distance between the

proton and separate atomic strings, a_0 is the Bohr radius and $a = \left[\frac{9\pi^2}{128Z_2} \right]^{1/3} a_0$ gives the

atom screening radius; K_0 denotes the zero order modified Bessel function of the second kind, with the fitting parameters: $(\alpha_i) = (0.35, 0.55, 0.10)$,

$(\beta_i) = (0.30, 1.20, 6.00)$.

Correspondingly, the potential between two i, j sites is

$$\Phi_{i,j} = U_i(r) + \frac{B}{r_{ij}^n}. \quad (6.36)$$

n is Born exponent. Coefficients B and n are experimental fitting parameters determined from ion compressibility measurements [121], likewise, the exponential repulsion between the overlapping electron orbitals within the channel is described

$$\text{by } B \exp\left(\frac{-\rho}{r_{i,j}}\right).$$

$$\text{The measure of the orbitals overlap corresponds to } l = \exp\left(d^2/a^2 \left((1/b) - 2b\right)\right), \quad (6.37)$$

where

$$b = \sqrt{(1 + \omega_s/\Omega)}, \quad \varepsilon = (d/a) f \hbar \omega_e, \quad (6.38)$$

denote degree of confinement field and discretized energy, respectively.

Eq. (6.37) includes the variation of charge density of the overlapping area due to different valence electron contribution to interaction: lattice - induced potential (across the channel) [122, 123]. The overlap $l = \exp(d^2/a^2)$ stands only for zero external field.

The one electron energies [124] for neutral Si: $(1s)^2 (2s)^2 (2p)^6 (3s)^2 (3p)^2$ are calculated in Hartree unit 1 Hartree = 2 Rydberg = 27.210 eV [123] as $1s = 67.02$, $2s = 5.5435$, $2p = 3.977$, $3s = 0.49875$, $3p = 0.2401$. The electron affinity for Si crystal is 4.018 eV and 1.385 eV for Si atom [125].

In the rotating frame, the reduced form of protons equation of motion, considering small angle approximation in transverse position plane [59], is

$$\frac{\partial x}{\partial z} = \varphi_x, \quad \frac{\partial y}{\partial z} = \varphi_y, \quad \frac{\partial \varphi_x}{\partial z} = -\frac{1}{2E_{\perp}} \frac{\partial U(x, y)}{\partial x}, \quad \frac{\partial \varphi_y}{\partial z} = -\frac{1}{2E_{\perp}} \frac{\partial U(x, y)}{\partial y}. \quad (6.39)$$

φ_x and φ_y represent the x - y component of the proton scattering angle. The channeled proton distributions are mapped in configuration space and angular space in two steps: to transverse position phase plane, $x' - y'$ and to scattering angle phase plane, $\theta_x - \theta_y$

[20, 79] in accordance with the chosen value of reduced crystal thickness, Λ and the tilt angle, φ .

The phase space transformations are determined via Jacobean:

$$J_{\theta} \equiv \frac{\partial \theta_x}{\partial x} \cdot \frac{\partial \theta_y}{\partial y} - \frac{\partial \theta_y}{\partial x} \cdot \frac{\partial \theta_x}{\partial y}, J_{\theta_{x,y}} = J(x, y, \varphi, \Lambda). \quad (6.40)$$

Eq. (6.40) comprises the proton trajectory components: $\theta_x(x, y, \varphi, \Lambda)$ and $\theta_y(x, y, \varphi, \Lambda)$.

It establishes a bond transformation between differential transmission cross section, $\sigma = 1/|J|$ and phase space manifolds in configuration and angular plane.

The one-dimensional thermal vibration amplitude of the crystal's atoms is 0.0074 nm [20, 67, 79, 83, 85]. The average frequency of transverse motion of protons moving close to the channel axis is equal to 5.94×10^{13} Hz. It is determined from the second order terms of the Taylor expansion of the crystal continuum potential in vicinity of the channel axis [66, 126]

$$U(x, y) = \frac{2Z_1 Z_2 e^2}{d} \sum_{i=1}^3 \sum_{j=1}^M \alpha_i K_0 \left(\beta_i \frac{\rho_c}{a} \right), \quad (6.41)$$

where $\rho_c = \sqrt{(x-x_i)^2 + (y-y_i)^2}$,

$$\frac{\partial^2 U(x, y)}{\partial x^2} = \frac{2Z_1 Z_2 e^2}{d} \sum_{i=1}^3 \sum_{j=1}^M \alpha_i \frac{\beta_i}{a} \cdot \left(K_0 \left(\frac{\beta_i \rho_c}{a} \right) \left(\frac{\beta_i}{a} \right) \frac{(x-x_j)^2}{\rho_c^2} + \right. \\ \left. + \frac{2(x-x_j)^2 - \rho_c^2}{\rho_c^3} K_1 \left(\frac{\beta_i \rho_c}{a} \right) \right), \quad (6.42)$$

$$\frac{\partial^2 U(x, y)}{\partial y^2} = \frac{2Z_1 Z_2 e^2}{d} \sum_{i=1}^3 \sum_{j=1}^M \alpha_i \frac{\beta_i}{a} \cdot \left(K_0 \left(\frac{\beta_i \rho_c}{a} \right) \left(\frac{\beta_i}{a} \right) \frac{(y-y_j)^2}{\rho_c^2} + \right. \\ \left. + \frac{2(y-y_j)^2 - \rho_c^2}{\rho_c^3} K_1 \left(\frac{\beta_i \rho_c}{a} \right) \right), \quad (6.43)$$

$$\Delta(U(x, y)) = \frac{2Z_1 Z_2 e^2}{d} \sum_{i=1}^3 \sum_{j=1}^M \alpha_i \frac{\beta_i}{a} \cdot \left(\left(K_0 \left(\beta_i \frac{\rho_c}{a} \right) \right) \left(\frac{\beta_i}{\rho_c a} \right) \right). \quad (6.44)$$

K_1 denotes the first order modified Bessel function of the second kind, d and M represent distance from atomic strings and their number, respectively.

The components of the proton scattering angle, $\varphi_x = \frac{v_x}{v_0}$ and $\varphi_y = \frac{v_y}{v_0}$, are solved numerically using the implicit Runge-Kutta method of the fourth order [66].

The components of the proton impact parameter are obtained randomly from the uniform distributions inside the channel. The transverse components of the final proton velocity, v_x and v_y are presented within the Gaussian distribution of probability that the quantum spin state is recognized correctly, according to standard deviation $\Omega_{bx} = \Omega_{by} = \frac{\Omega_b}{\sqrt{2}}$, where Ω_b denotes the CP divergence. Since the channeled

protons angular distributions can be easily measured, they are used to reconstruct the quantum information regarding the protons distribution in transverse phase space [127].

In order to quantify the read out fidelity the information from entangled quantum trajectories is sampled from $\theta_x - \theta_y$ phase plane from 550,000 shots datasets [128]. The initial number of protons correspond to quantum trajectories spin states obtained from 5×10^7 traces.

6.6 Discussion

3-d representation of channeled protons contour plots for 92 nm $\langle 100 \rangle$ ^{29}Si nanocrystal, $\Lambda = 0.5$ [24, 25], for tilt angles: $\varphi = 0.05 \psi_c$, $\varphi = 0.15 \psi_c$ and $\varphi = 0.20 \psi_c$, where φ is the angle of external field relative to symmetry axis of the spin transformation tensor, are represented in figure 6.1 (a, b, c). The external field of 1 MeV is chosen to match the limits of Bohr radius with initial CP peak separation at 20% of the critical angle

(relative to tensor principal axis). It allows generation of the final mixed quantum state, controlled by the pseudosecular term $B = 3D \cos(\varphi) \sin(\varphi)$, i.e. it allows efficient dipolar coupling, D , between electron and nuclear spin states. The spacing between separate peaks about longitudinal z -direction of the confinement field is calculated via $\frac{\pi^2 \hbar^2 (n+1/2)}{(L^2 m_e)}$, $L = 92$ nm, for n -discretized 2-d potential: $E = E_n \left(n_{(X,\theta_x)}, n_{(Y,\theta_y)} \right)_Z$.

Obtained results show density of states (DOS) evolution in phase space for angular and transverse position profiles. Figures 6.1 (b) show that incident tilt angles above 15 % of the critical angle for channeling, consequent faster amplitude and phase attenuation for angular density profile. This effect induces further splitting of the channeling pattern.

Relative change of 5% for crystal tilts leads to strong yield redistribution in angular distribution profiles and it mostly affects phase profile central parts. The analysis in configuration space for tilts: $\varphi = 0.05 \psi_c$ and $\varphi = 0.15 \psi_c$ shows strongly picked circular cross section. Only a slight variation in pattern sharpness can be seen in density profile edges.

Figures 6.1(c), illustrate the angular and configuration DOS analysis for $0.20 \psi_c$. The angular phase space profile, 6.1(c (left)) shows non-homogenous transition in charge state density and splitting of channeled proton distribution pattern.

The characteristic splitting shows two pronounced maxima on the θ_x -axis followed by few nonsymmetrical peaks as lateral satellites. Their spatial positions and amplitudes are correlated via CP mediated Zeeman interaction by $g\beta_e B/2$ term. This non-secular term shifts the energy levels of singlet spin states and splits DOS peaks (shift affects the Fermi level for electron spin-down and spin-up configuration). Consequently, spin DOS structure is uniquely described via two mixed quantum states.

The central positions of angular and spatial density distributions in phase space are shown in figure 6.2 (a, b). Maximal amplitudes of tilt angles equals $\varphi = 0.05 \psi_c$, $0.10 \psi_c$ and $0.15 \psi_c$. Designated plots correspond to reduced crystal thickness in range of 0.00 - 300.0., for $L = 1.69 \mu\text{m}$ and 0.00 - 0.300, for $L = 99.2$ nm, respectively. These

dependencies determine the focusing region, i.e. specify the proton beam full width at half maximum (FWHM).

A comparative analysis for the same values of φ , Λ and amplitude maxima in configuration plane is presented in figure 6.2(b), it determines the length and phase space transformation bond between scattering angle plane and mapped transverse position (configuration) plane.

Yield dependence of harmonic confinement potential (governed by first two terms in eq. 6.21) becomes zero for tilts over $0.50 \psi_c$ in transverse and angular phase plane, as shown by figure 6.3. The normalization and boundary condition are restricted to effective Bohr radius: $a^* = \hbar^2 k / m_e$. Changing tilts while keeping fixed thickness parameter to $L = 99.2$ nm gives the non-monotonic dependence to exchange coupling energy $J(\varepsilon)$ as a function of quantum displacement from harmonic oscillator stability point. It goes to zero asymptotically and indicates the complete separation of quantum states and inexistence of singlet-triplet transitions at higher tilts due to small orbitals overlap (eqs. 6.37, 6.38).

Figure 6.4 illustrates the localization of quantum spin waves corresponding to uncertainty principle. The CP superimposed electron spin states (spin wave probability density functions) are positioned inside the Bohr radius. Electron probability densities produce maxima over each nuclear position. The quantum proton trajectory evolution with various tilt angles is calculated for $\Lambda = 0.25$ in configuration space, i.e. $\Lambda = 0.50$ in (mapped) angular space. We analyze eight characteristic tilt shifts: $\varphi = 0.00, 0.05 \psi_c, 0.10 \psi_c, 0.15 \psi_c, 0.20 \psi_c, 0.25 \psi_c, 0.35 \psi_c$, and $0.50 \psi_c$. Inside the Bohr radius at distance $x = \pm d$ around the peak centers, the confinement field is parabolic so that ground state of mixed wave functions coincides with harmonic oscillator state.

Observed amplitude dependences of proton yield for tilts $\geq 0.10 \psi_c$ are attributed to stronger interaction influences of higher anharmonic terms in eq. (6.21). This is more pronounced for the spatial CP distribution.

Amplitude decreasing and changes of peaks FWHM (positions and spatial symmetry) are indicators for the state of strong system perturbation, i.e. due to the effect of quartic anharmonic terms in the exchange interaction, eq. 6.21.

The observed modulation of DOS states for tilts $\geq 0.20 \psi_c$ is disregarded, i.e. the main contribution to the superfocusing effect comes from the crystal tilts below 20% of the critical angle for channeling.

The analysis of the asymptotic behavior of the channeled protons axial yield for proton distributions: $\varphi = 0.00\psi_c$, $\Lambda = 0.5$, (when FWHM of generated focused area converges to zero making the sub-nanometer spatial resolution possible) has shown that the only case when the angular yield is singular corresponds to the zero-degree focusing effect. It is shown that an increase in the crystal tilt angle value of 15% of the critical angle for channeling facilitates the suppression of the zero-degree focusing effect. Former leads to a significant change in amplitude and width of the angular channeled protons profile, causing the splitting on two lateral non-uniform circular patterns with maxima located along θ_x -axis which corresponds to smaller lateral peaks.

This behavior is confirmed for energy range from several eV up to several MeV which can be employed for PIXE analysis. To facilitate and control close encounter collision processes in order to induce nuclear reactions one can also use this method as intermediate process for nuclear collision cascade. However for the proton beam energies above 100 MeV the FWHM of the channeled proton peaks in density profiles is highly narrower ≤ 5 pm less than effective Bohr radius due to enhanced orbitals overlap of superfocusing effect governed by higher degree of spatial confinement.

Figure 6.5 represents the scheme of energy splitting and exchange coupling energy between singlet $|S\rangle$ state and $|T\rangle$ triplet-polarized state localized inside the Bohr radius. Upon modulation the CP field, unitary spin rotations are performed around two non-commuting axes: θ, z . Before manipulation, discretized proton spin states mediated through Zeeman interaction include sublevels $|01\rangle$ and $|10\rangle$. The populations of quantum states are distributed according to electron spin polarization at thermal equilibrium: in

electron manifold the nuclear quantization axes $-\frac{B}{2}I_{(x,y,\theta_x,\theta_y)} + \left(\omega_n - \frac{A}{2}\right)I_Z$, correspond to electron spin in $|\downarrow\rangle$ state, whereas the nuclear axes, $+\frac{B}{2}I_{(x,y,\theta_x,\theta_y)} + \left(\omega_n + \frac{A}{2}\right)I_Z$, apply to electron spin in $|\uparrow\rangle$ state. We then impose a pulse sequence of π/n tilts relative to \mathcal{G} axes on Bloch sphere. This lifts the system energy close to triplet state where exchange $\mathbf{J}(\varepsilon)$ is large. It triggers the coherent transition of proton eigenstates $|01\rangle \rightarrow |\uparrow\rangle$, $|10\rangle \rightarrow |\downarrow\rangle$ and forms the final mixed quantum entangled state containing the superposition of proton - electron eigenstates, $|\downarrow\uparrow\rangle, |\uparrow\downarrow\rangle$.

To provide a transition to triplet state $|\downarrow\downarrow\rangle$ upon initialization the system is rotated by π pulse about z axes of Bloch sphere through the angle $\varphi = \mathbf{J}(\varepsilon)/\hbar$, where $\mathbf{J}(\varepsilon)$ denotes the exchange coupling as a function of energy difference, ε between the levels. Presented energy diagram shows that former sequence corresponds to the initial exchange splitting E_{ST} further dominated by CP induced $\mathbf{J}(\varepsilon)$ mixing between energy levels detuned by φ . While increasing the confinement energy $E(\varphi, \Lambda)$, the (1, 1) triplet state hybridizes and produces a tunneling effect so that different superposition states can be realized. Dependency of the field caused by lifted degeneracy of triplet state further decreases the separation between energy levels, while the exchange coupling increases the Gaussian of orbitals overlap, as defined in eq. (6.37).

The CP simulation patterns in transverse position plane for fixed value of $\Lambda = 0.175$ are shown by figure 6.6 (a, b, c).

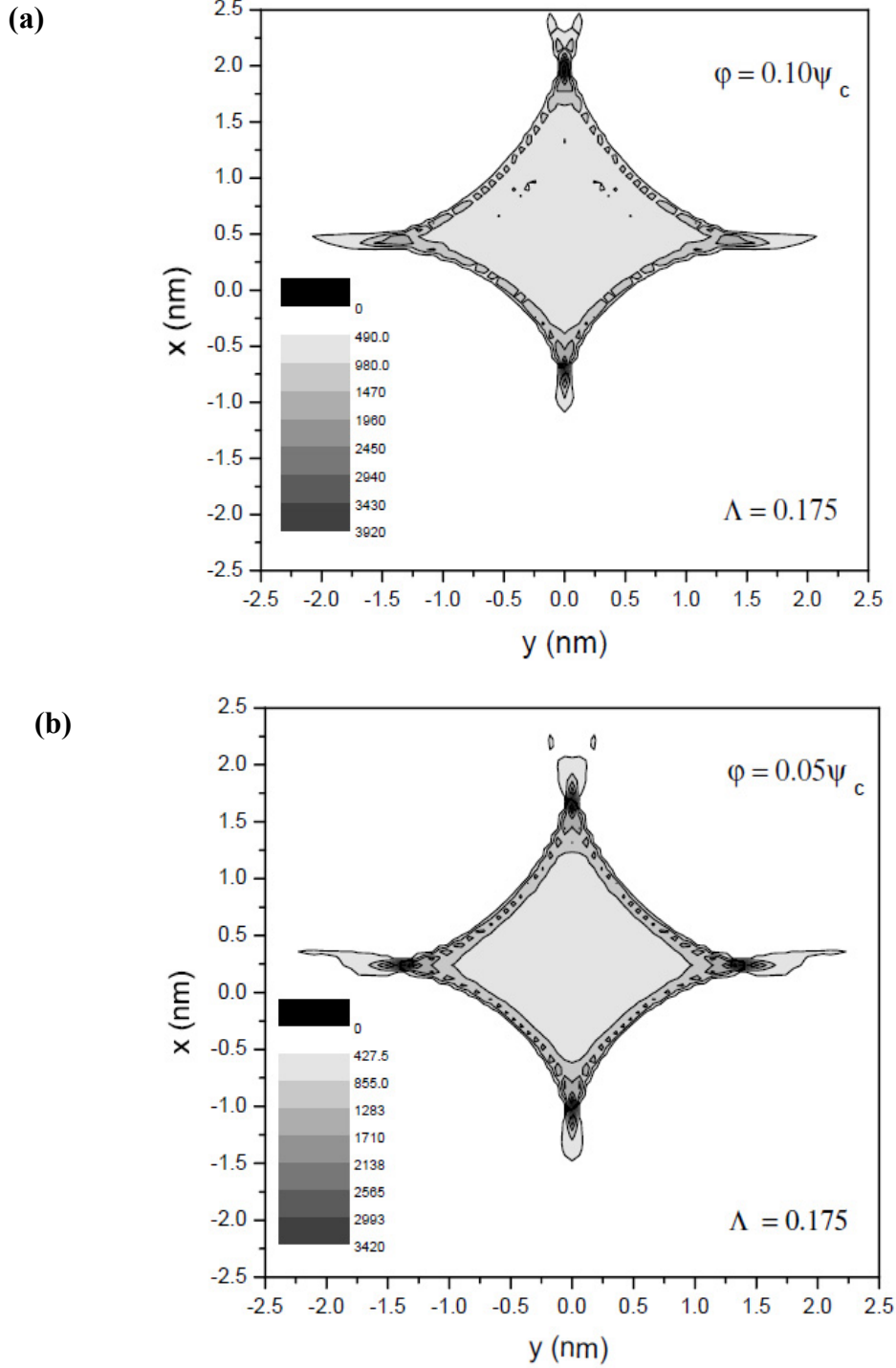


Figure 6.6 (a, b): The evolution of CP modulated quantum trajectories. The mixed entangled states in the transverse position plane are represented for $L=0.175$. The tilt angles correspond to $\phi = 0.05 \psi_c$ (a), $\phi = 0.10 \psi_c$ (b). Channeled protons intensity distributions levels are designated with increasing gray scale tone.

The proton trajectory shifts with tilt angle along $y = 0$ axis and spreads from intersection area of x - y plane into cusped elongated deltoidal pattern. The shifts are governed by

atomic strings repulsive potential. Even a small change of tilt angle causes a strong system perturbation and therefore activates the higher power terms in the ion-atom interaction potential. Former influences regularity of proton trajectories and leads to a gradual reduction of DOS in central area of channel.

This causes the non-uniform flux redistribution, now filled with gaps. Hence, it affects the continuous conservation of distribution functions in phase space volume [110, 111]. Consequently, the axially channeled protons cannot encounter the state of statistical equilibrium.

(c)

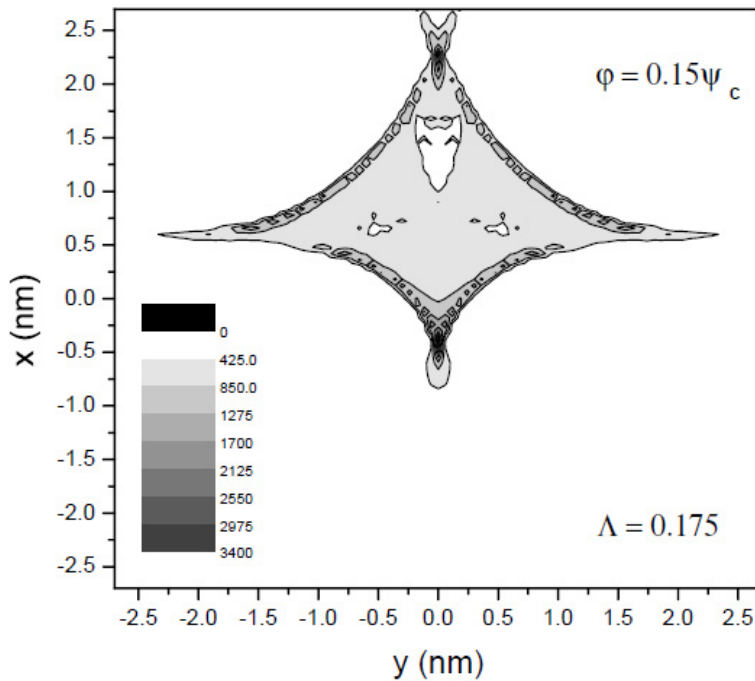


Figure 6.6 (c): The evolution of CP modulated quantum trajectories. The mixed entangled states in the transverse position plane are represented for $L= 0.175$. The tilt angle corresponds to $\varphi = 0.15 \psi_c$. Channeled protons intensity distributions levels are designated with increasing gray scale tone.

That effect has been resolved in scope of KAM theory [127], when the classical integrability of the Hamiltonian's is broken by sufficiently small perturbation, the system nevertheless retains its dynamics in the form of periodic oscillation moving on invariant phase space profile. Although these invariants of phase space have form of

intricate fractal structure in vicinity of $\langle 100 \rangle$ axis, they still cover a large portion of phase space. In that sense the reduced crystal thickness can be fully discretized by performing the power law expansion of random points described for interval $[n_i, n_i+n]$ between two nearest neighboring fractal points $\Lambda(n) = Ln^\alpha$, $n \rightarrow \infty$, where fractal dimension for $\alpha < 0$ draws logarithmic singularity for proton density distribution.

Chapter 7

Concluding remarks and outlook

In conclusion our calculations and simulation results demonstrate a hybrid proton-electron quantum interface for multipartite entanglement under constraint metric of uncertainty principle. We established the correlation between electronic spin states and off-diagonal hyperpolarized nuclear spin states under CP induced field. We used axial configuration of Si $\langle 100 \rangle$ channel to initialize and control each electron spin state via superimposed proton spin chain. Utilizing a dynamically decoupled sequence we have obtained the universal quantum control and controllable coupling between singlet and triplet-polarized spin states.

By calculating the electron spin and CP field eigenstates via full density matrix we established the proof of non-orthogonal mixed quantum state. Upon hyperpolarization sequence, the increased sensitivity of nuclear spin subspaces dependence to electron spin states reduces the linear spin entropy and leads to maximized entanglement of mixed states in density matrix. We have shown that stability dependence of nuclear field results from anisotropic term of the hyperfine coupling, here regarded as a tunable parameter for unitary spin control. It can be chosen to enhance the feasibility of producing entangled mixed states. A resultant mixed quantum state that we demonstrated in S-T systems represents important step toward realization of scalable architecture for quantum information processing. Complementary, a scalable network of entangled electron-nuclear states would form a basis for a cluster state of quantum processors integrated in silicon. In addition, generation of entanglement process comprising the network of such correlated spin states would enhance the quantum error correction beyond any separable state and extend the precision in quantum metrology. That would allow implementation of quantum error correcting techniques (QEC codes) directly to perfectly entangled mixed states and direct protection of quantum states from interaction with environment without prior entanglement purification protocols (EPP).

In that context, the off-diagonal electron-nuclear eigenstates as mixed quantum states are not longer invariant under unitary spin operations and represent observables in density matrix.

Finally, the controllable addressing of single spins in quantum networks, the individual control of unitary spin precessions (electron-nuclear spin phase rotations) in combination with local g -factor engineering would provide a scheme for deposition of multipartite entangled states and manipulation of quantum memory and quantum key distribution (QKD) based on transmission of Gaussian-modulated individual coherent states.

Another possibility for further exploration points toward active control of the channeled proton beam properties in the superfocusing effect, revealing the important role of mutual contribution of the harmonic and anharmonic terms. This emphasizes the importance in careful selection regarding the appropriate combination of the crystal tilt angle value with crystal thickness in order to gain high spatial resolution and localization accuracy. As a result the implementation of such nano-scale precision scanning method could produce a detailed map of discrete inter-atom positions, and create a highly resolved image, built-up through a process of the proton beam focusing.

This behavior is confirmed for energy range from several eV up to several MeV which can be employed for PIXE analysis. To facilitate and control close encounter collision processes in order to induce nuclear reactions one can also use this method as intermediate process for nuclear collision cascade. However for the proton beam energies above 100 MeV the FWHM of the channeled proton peaks in density profiles is highly narrower ≤ 5 pm less than effective Bohr radius due to enhanced orbitals overlap of superfocusing effect governed by higher degree of spatial confinement.

Bibliography

- [1.] J. J. Pla, K. Y. Tan, J. P. Dehollain, W. H. Lim, J. J. Morton D. N Jamieson, A. Morello, *Nature*, 489(7417), 541-545 (2012).
- [2.] L. Pavesi, S. V. Gaponenko, and L. D. Negro, *Towards the First Silicon Laser*, Dordrecht: Kluwer Academic Publishers, 2003.
- [3.] G. Feher and E. A. Gere, *Phys. Rev.* 114, 1245 (1959).
- [4.] C. Tahan, M. Friesen, and R. Joynt, *Phys. Rev. B* 66, 035314 (2002).
- [5.] F.A. Zwanenburg, A.S. Dzurak, A. Morello, M.Y. Simmons, L.C. L. Hollenberg, G. Klimeck, S. Rogge, S.N. Coppersmith and M.A. Eriksson, *Rev. Mod. Phys.* 85, 961 (2013).
- [6.] G. Burkard, D. Loss, and D.P. Di Vincenzo, *Phys. Rev. B* 59, 2070 (1999).
- [7.] X. Hu and S. Das Sarma, *Phys. Rev. A* 61, 062301 (2000).
- [8.] T. Kojima, R. Nebashi, K. M. Itoh, and Y. Shiraki, *Appl. Phys. Lett.* 83, 2318 (2003).
- [9.] K. M. Itoh, J. Kato, M. Uemura, A. K. Kaliteyevskii, O. N. Godisov, G. G. Devyatych, and H. Riemann, *Jpn. J. Appl. Phys.* 42, 6248 (2003).
- [10.] B. E. Kane, *Nature* 393,133 (1998).
- [11.] T. D. Ladd, J. R. Goldman, F. Yamaguchi, Y. Yamamoto, E. Abe and K. M. Itoh, *Phys. Rev. Lett.* 89, 017901 (2002).
- [12.] G. W. Morley, M. Warner, A. M. Stoneham, P. T. Greenland, J. van Tol, C. W. M. Kay, and G. Aeppli, *Nature Materials* 9, 725 (2010).
- [13.] T. D. Ladd, D. Maryenko, Y. Yamamoto, E. Abe, and K. M. Itoh, *Phys. Rev. B* 71, 014401 (2005).
- [14.] T. Sekiguchi, S. Yoshida, Y. Shiren, K. M. Itoh, J. Myslivecek, and B. Voigtlander, *J. Appl. Phys.* 101, 081702 (2007).
- [15.] T. Sekiguchi, S. Yoshida, and K. M. Itoh, *Phys. Rev. Lett.* 95, 106101 (2005).
- [16.] S. Yoshida, T. Sekiguchi, and K. M. Itoh, *Appl. Phys. Lett.* 87, 031903 (2005).
- [17.] A. S. Verhulst, D. Maryenko, Y. Yamamoto, and K. M. Itoh, *Phys. Rev. B* 68, 054105 (2003).
- [18.] E. Dementyev, D. Li, K. Mac Lean, and S. E. Barrett, *Phys. Rev. B* 68, 153302 (2003).

- [19.] A. S. Verhulst, I.G. Rau, Y. Yamamoto and K. M. Itoh, *Phys. Rev. B* 71, 235206 (2005).
- [20.] S. Petrović, N. Nešković, V. Berec, M. Ćosić, *Phys. Rev. A* 85, 032901 (2012).
- [21.] V. Berec, *PLoS ONE* 7(9), e45254 (2012). doi:10.1371/journal.pone.0045254.
- [22.] V. I. Berec, *PIERS Proceedings*, Stockholm, Sweden, Aug. 12-15, Published by Electromagnetics Academy, Cambridge, 794-796 (2013).
- [23.] J. J. Morton, B. W. Lovett, *Annu. Rev. Condens. Matter Phys.* 2, 189-212 (2011).
- [24.] A. Einstein, B. Podolsky and N. Rosen, *Phys. Rev.* 47, 777 (1935).
- [25.] E. Schrödinger, *Naturw.* 23, 807 (1935).
- [26.] J. S. Bell, *Physics* 1, 195 (1964).
- [27.] R. F. Werner, *Phys. Rev. A* 40, 4277 (1989).
- [28.] K. Phillip, L. Raymond, M. Michele, *An introduction to quantum computing*, Oxford University Press, 2007.
- [29.] R. F. Werner and M. M. Wolf, *Quantum Information & Computation*, 1(3), 1-25 (2001).
- [30.] W. K. Wootters, *Quantum Information and Computation*, 1(1), 27-44 (2001).
- [31.] S. J. Jones, H. M. Wiseman, and A. C. Doherty, *Phys. Rev. A* 76(5), 052116.
- [32.] N. L. Harshman and K.S. Ranade, *Phys. Rev. A* 84, 012303 (2011).
- [33.] W. Thirring, R. A. Bertlmann, P. Köhler and H. Narnhofer. *Eur. Phys. J. D*64, 181 (2011).
- [34.] C.W. Curtis and I. Reiner, *Representation Theory of Finite Groups and Associative Algebras*, AMS Chelsea Publishing, 1962.
- [35.] M. Horodecki, P. Horodecki, and R. Horodecki, *Phys. Lett. A* 223 1, (1996).
- [36.] A. Peres, *Phys. Rev. Lett.* 77 1413 (1996).
- [37.] M. A. Nielsen and I. L. Chuang. *Quantum Computation and Quantum Information*. Cambridge University Press, Cambridge, 2000.
- [38.] N. A. Gershenfeld and I. L. Chuang, *Science* 275, 350 (1997).
- [39.] K. Dorai, Arvind, and A. Kumar, *Phys. Rev. A* 61, 042306 (2000).
- [40.] J. Kim, J.-S. Lee, and S. Lee, *Phys. Rev. A* 65, 054301 (2002).
- [41.] L. M. K. Vandersypen, M. Steffen, G. Breyta, C. S. Yannoni, *Nature* 414(6866) 883-887 (2001).

- [42.] I. L Chuang, N. Gershenfeld and M. Kubinec, *Phys. Rev Lett.* 80 3408 (1998).
- [43.] A. Schweiger and G. Jeschke, *Principles of Pulse Electron Paramagnetic Resonance*, Oxford University Press, New York, 2001.
- [44.] F. Hoehne, H. Huebl, B. Galler, M. Stutzmann, M. S. Brandt, *Phys. Rev. Lett.* 104, 046402 (2010).
- [45.] E. Abe, J. Isoya, and K. M. Itoh, *Journal of superconductivity*, 18(2), 157-161 (2005).
- [46.] M. Belli, M. Fanciulli, and N. V. Abrosimov, *Phys. Rev. B* 83(23), 235204. (2011).
- [47.] C. D. Weis, C. C. Lo, V. Lang, A. M. Tyryshkin, R. E. George, K. M. Yu, and T. Schenkel, *Appl. Phys. Lett.* 100(17), 172104-172104 (2012).
- [48.] M. H., Mohammady, G. W. Morley, and T. S. Monteiro, *Phys. Rev. Lett.* 105, 067602 (2010).
- [49.] J. J. Morton, A. M. Tyryshkin, R. M. Brown, S. Shankar, B. W. Lovett, A. Ardavan, and S. A. Lyon, *Nature* 455, 1085-1088 (2008).
- [50.] G. W. Morley, M. Warner, A. M. Stoneham, P. T. Greenland, J. van Tol, C. W. Kay, and G. Aeppli, *Nature Materials*, 9(9), 725-729 (2010).
- [51.] D. Rugar, R. Budakian, H. J. Mamin, and B. W. Chui, *Nature* 430, 329 (2004).
- [52.] S. Simmons, R. M. Brown, H. Riemann, N. V. Abrosimov, P. Becker, H. J. Pohl, and J. J. Morton, *Nature* 470, 69-72 (2011).
- [53.] A. Morello, J. J. Pla, F. A. Zwanenburg, K. W. Chan, K. Y. Tan, H. Huebl, and A. S. Dzurak, *Nature* 467, 687-691 (2010).
- [54.] A. Abragam, *Principles of Nuclear Magnetism*, Clarendon Press, 1978.
- [55.] C. Cohen-Tannoudji, B. Diu, and F. Laloe, *Quantum Mechanics* John Wiley & Sons, New York, 1977.
- [56.] F. H. Eisen, *Phys. Lett.* 23, 401 (1966).
- [57.] M. R. Altman, L. C. Feldman, and W. M. Gibson, *Phys. Rev. Lett.* 24, 464 (1970).
- [58.] D. V. Morgan, *Channeling: Theory, observation and applications*, John Wiley and Sons, 1973.
- [59.] D. S. Gemmell, *Rev. Mod. Phys.* 46, 129 (1974).

- [60.] Beloshitsky V. V., Komarov F. F. and Kumakhov M. A., Phys. Rep. 139, 293 (1986).
- [61.] M. T. Robinson, and O. S. Oen, Phys. Rev. 132, 2385 (1963).
- [62.] B. R. Appleton, C. D. Moak, T. S. Noggle, and J. H. Barrett, Phys. Rev. Lett. 28, 1307 (1972).
- [63.] W. Scandale, A. Vomiero, S. Baricordi, P. Dalpiaz, M. Fiorini, V. Guidi, A. Mazzolari and M. Prest, Phys. Rev. Lett. 101(16), 164801 (2008).
- [64.] J. Lindhard, K. Dan. Vidensk. Selsk., Mat.-Fys. Medd. 34 (14), 1 (1965).
- [65.] G. Z. Molière, Naturforsch, A 2, 133 (1947).
- [66.] M. Abramowitz and I. A. Stegun, Handbook of Mathematical Functions, Dover, New York, p. 896, 1965.
- [67.] B. W. Batterman and D. R. Chipman, Phys. Rev. 127, 690 (1962); Ya. S. Umanskii and V. I. Prilepskii, Fiz. Tverd. Tela 7, 2958 (1966) Sov. Phys., Solid State 7, 2399 (1966).
- [68.] B. R. Appleton, C. Erginsoy, and W. M. Gibson, Phys. Rev. 161, 330 (1967).
- [69.] Yu. N. Demkov and J. D. Meyer, Eur. Phys. J. B 42, 361 (2004).
- [70.] E. Betzig, J. K. Trautman, T. D. Harris, J. S. Weiner, and R. L. Kostelak, Science 251, 1468 (1991).
- [71.] J. Orloff, M. Utlaut, and L.W. Swanson, Interaction of Ions with Solids, in: High Resolution Focused Ion Beams, Kluwer Academic and Plenum, p. 123, 2002.
- [72.] M. Y. Simmons, Nature Physics 4, 165 (2008).
- [73.] W. Schnitzler, N. M. Linke, R. Fickler, J. Meijer, F. Schmidt-Kaler, and K. Singer, Phys. Rev. Lett. 102, 070501 (2009).
- [74.] S. Bellucci, V. M. Biryukov, Yu. A. Chesnokov, V. Guidi, and W. Scandale, Phys. Rev. ST AB 6, 033502 (2003).
- [75.] X. Artru, S. P. Fomin, N. F. Shulga, K. A. Ispirian, and N. K. Zhevago, Phys. Rep. 412, 89 (2005).
- [76.] L. Miletić, S. Petrović, and N. Nešković, Nucl. Instrum. Meth. Phys. Res. B 115, 337 (1996).
- [77.] L. Miletić, S. Petrović, and N. Nešković, Radiat. Eff. Def. Solids 141, 235 (1997).

- [78.] L. Živković, S. Petrović, S. Kossionides, and N. Nešković, *Phys. Lett. A* 286, 292 (2001).
- [79.] N. Nešković, S. Petrović, and D. Borka, *Nucl. Instrum. Meth. Phys. Res. B* 267, 2616 (2009).
- [80.] N. Nešković, *Phys. Rev. B* 33, 6030 (1986).
- [81.] N. Nešković and S. Petrović, *J. Electron Spectrosc.* 129, 233 (2003).
- [82.] H. F. Krause, S. Datz, P. F. Dittner, J. Gomez del Campo, P. D. Miller, C. D. Moak, *Phys. Phys. Rev. B*, 33(9), 6036 (1986).
- [83.] H. F. Krause, J. H. Barrett, S. Datz, P. F. Dittner, N. L. Jones, J. Gomez del Campo, and C. R. Vane, *Phys. Rev. A* 49(1), 283 (1994).
- [84.] S. Petrović, L. Miletić, and N. Nešković, *Phys. Rev. B* 61, 184 (2000).
- [85.] H. F. Krause and S. Datz, *Channeling of Heavy Ions through Crystalline Lattices*, in: *Advances in Atomic, Molecular, and Optical Physics*, Academic, New York, Vol. 37, p. 139, 1996.
- [86.] I. V. Komarov and A. P. Shcherbakov, *Vestnik Leningrad. Univ., Ser. Fiz. Khim.* (16), 24 (1979) (in Russian).
- [87.] Yu. N. Demkov, *Vestnik Leningrad. Univ., Ser. Fiz. Khim.* (2) 31 (1987) (in Russian).
- [88.] S. Petrović, L. Miletić, and N. Nešković, *Phys. Rev. B* 61, 184 (2000).
- [89.] J. C. Slater, *J. Chem. Phys.* 41, 3199 (1964).
- [90.] J. F. Nye, *Natural Focusing and Fine Structure of Light*, Institute of Physics Publishing, p. 198, 1999.
- [91.] N. Nešković, G. Kapetanović, S. Petrović, and B. Perović, *Phys. Lett. A* 179, 343 (1993).
- [92.] N. Nešković, S. Petrović, G. Kapetanović, B. Perović, and W. N. Lennard, *Nucl. Instrum. Meth. Phys. Res. B* 93, 249 (1994).
- [93.] W. Assmann, H. Huber, S. A. Karamian, F. Grüner, H. D. Mieskes, *Phys. Rev. Lett.* 83, 1759 (1999).
- [94.] A. V. Krashenninnikov and F. Banhart, *Nature Materials*, 6 (2007).
- [95.] M. Richard, P. Langford, M. Nellen, G. Jacques, and Fu. J. Yongqi, *MRS Bulletin*, 32, (2007).

- [96.] R. Haakenaasen, L. V. Hau, J. A. Golovchenko, *Phys. Rev. Lett.* 75, (8), 1650 (1995).
- [97.] V. M. Biryukov, S. Bellucci and V. Guidi, *Nucl. Instrum. Meth. B* 231 70 (2005).
- [98.] A. J. F. Levi, *Proceedings of the IEEE* 96, 335-342 (2007).
- [99.] M. Friesen, P. Rugheimer, D. E. Savage, M. G. Lagally, D.W. van der Weide, et al., *Phys. Rev. B* 67, 12130111, (2003).
- [100.] I. Žutić, J. Fabian, S. Das Sarma, *Rev. Mod. Phys.* 76, 323-410 (2004).
- [101.] H. W. Liu, T. Fujisawa, Y. Ono, H. Inokawa, A. Fujiwara, et al., *Phys. Rev. B* 77, 073310 (2008).
- [102.] E. P. Nordberg, G. Ten Eyck, H. L. Stalford, R. P. Muller, R. W. Young, et al., *Phys. Rev. B* 80, 115331 (2009).
- [103.] R. Hanson, L. P. Kouwenhoven, J. R. Petta, S. Tarucha, and L. M. K. Vandersypen, *Rev. Mod. Phys.* 79, 1217 (2007).
- [104.] K. C. Nowack, F. H. L. Koppens, Y. V. Nazarov, and L. M. K. Vandersypen, *Science* 318, 1430 (2007).
- [105.] S. Foletti, H. Bluhm, D. Mahalu, V. Umansky, and A. Yacoby, *Nature Phys.* 5, 903 (2009).
- [106.] D. Press, T. D. Ladd, B. Zhang, and Y. Yamamoto, *Nature* 456, 218 (2008).
- [107.] I. Appelbaum, B. Q. Huang, and D. J. Monsma, *Nature* 447 (7142), 295 (2007).
- [108.] Y. Demkov, *Physics of atomic nuclei*, 72, 779-785 (2009).
- [109.] V. Guidi, A. Mazzolari, D. De Salvador, L. Bacci, *Phys. Rev. Lett.* 108, 014801 (2012).
- [110.] M. A. Kumakhov, E. Kührt, R. Wedell, *Radiat. Eff. Def. Solids*, 41, 1 (1979).
- [111.] D. van Vliet, *Radiat. Eff. Def. Solids*, 10(3), 137–155 (1971).
- [112.] D. Hinrichsen, A. J. Pritchard, *Modelling, State Space Analysis, Stability and Robustness*, Series: Texts in Applied Mathematics, Vol. 48, Volume package: Mathematical Systems Theory.
- [113.] L. M. Surhone, M. T. Timpledon, S. F. Marseken (ed.), *Liouville's Theorem (Conformal Mappings)*, VDM Publishing House, 2010.
- [114.] D. Heiss (ed.), *Fundamentals of quantum information: Quantum computation, communication, decoherence, and all that*, Berlin, Heidelberg: Springer, 2002.

- [115.] R. Horodecki, P. Horodecki, M. Horodecki, and K. Horodecki, *Rev. Mod. Phys.* 81, 865, (2009).
- [116.] J. H. Barrett, *Phys. Rev. Lett.* 31, 1542 (1973).
- [117.] G. Mitrikas, Y. Sanakis, G. Papavassiliou, *Phys. Rev. A* 81, 020305 (2010).
- [118.] J. M. Elzerman, R. Hanson, L. H. Willems van Beveren, B. Witkamp, L. M. K. Vandersypen et al., *Nature* 430, 431 (2004).
- [119.] J. J. Sakurai, *Modern Quantum Mechanics*, Addison Wesley, pp. 109-116, 1993.
- [120.] D. C. Mattis, *The Theory of Magnetism Made Simple: An Introduction to Physical Concepts and to Some Useful Mathematical Methods*, World Scientific, Singapore, 2006.
- [121.] C. Kittel, *Introduction to Solid State Physics*, John Wiley & Sons, pp. 66-71 1995.
- [122.] F. J. García de Abajo, P. M. Echenique, *Phys. Rev. B* 46, 2663 (1992).
- [123.] M Rösler, F. J. García de Abajo, *Phys. Rev. B* 54, 17158 (1996).
- [124.] C.-T. Sah, *Fundamentals of Solid State Electronics*, World Scientific, Singapore, pp. 90 -93, 1991.
- [125.] J. C. Slater, in *Quantum Theory of Matter*, 2nd, ed. Herman and Skillman, McGraw Hill, pp.145 and 150, 1968.
- [126.] T. S. Parker, L.O. Chua, *Practical Numerical Algorithms for Chaotic Systems*, New York: Springer-Verlag, pp. 278-296, 1989.
- [127.] H. W. Broer, *Kam Theory: The Legacy of Kolmogorov's 1954 paper*, *Bulletin, New Series, of the American Mathematical Society*, 41(4) pp. 507-521 (2004).
- [128.] Fortran source library: http://people.sc.fsu.edu/~jburkardt/f_src/f_src.html

Биографија

Весна И. Берез, рођена 1975. године у Београду, дипломирала је на Физичком факултету у Београду 2007. године са просечном оценом 9,26. Исте године је стекла звање дипломирани физичар-Мастер на физичком факултету, Универзитет у Београду. Од јануара 2007. до децембра 2008. године била је ангажована у Институту за физику у оквиру центра за чврсто стање и нове материјале и укључена у експериментално и теоријско истраживање вибрационих и електронских стања наноструктурних система: полупроводничких нанокompозитних материјала базираних на титанијуму и силицијуму. Од јануара 2009. запослена је у Институту за нуклеарне науке "Винча" где се бави проучавањем ефекта суперфокусирања каналисаних протона у комплексним системима и преносом квантне информације базираним на теоријском и нумеричком моделовању спинских интеракција у физици кондензоване материје.

Научни радови укључени у тезу:

V. Beres,

"Quantum Entanglement and Spin Control in Silicon Nanocrystal",
PLoS ONE 7(9) e45254 (2012). doi:10.1371/journal.pone.0045254

-Рад у врхунском међународном часопису – првих 30% (M21) = 8

S. Petrović, N. Nešković, V. Beres, M. Čosić,

"Superfocusing of channeled protons and subatomic measurement resolution",
Phys. Rev. A 85, 032901 (2012).

-Рад у врхунском међународном часопису – првих 30% (M21) = 8

V. I. Beres,

"Proton Beam Induction of Quantum Correlations in Silicon Nanocrystal",
Progress in Electromagnetics Research Symposium, Stockholm, Sweden, Aug. 12-15,
Published by Electromagnetics Academy, Cambridge, PIERS 794-796 (2013).

-Рад у међународном часопису

и саопштење по позиву са међународног конгреса, Progress in Electromagnetics Research Symposium, PIERS Stockholm 2013.

Прилог 1.

Изјава о ауторству

Потписани-а Берец Весна

број уписа 1/2007

Изјављујем

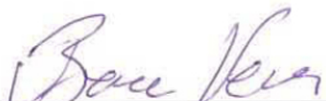
да је докторска дисертација под насловом

ION-ATOM QUANTUM ENTANGLEMENT IN A MAGNETIC FIELD BASED ON
THE SUPERFOCUSING EFFECT - THE SPIN QUBIT PROCESSING IN SILICON

- резултат сопственог истраживачког рада,
- да предложена дисертација у целини ни у деловима није била предложена за добијање било које дипломе према студијским програмима других високошколских установа,
- да су резултати коректно наведени и
- да нисам кршио/ла ауторска права и користио интелектуалну својину других лица.

Потпис докторанда

У Београду, 14. 10. 2013.



Прилог 2.

Изјава о истоветности штампане и електронске верзије докторског рада

Име и презиме аутора Берец Весна

Број уписа 1/2007

Студијски програм Физика кондензованог стања материје

ION-ATOM QUANTUM ENTANGLEMENT IN A MAGNETIC FIELD BASED ON THE SUPERFOCUSING

Наслов рада EFFECT - THE SPIN QUBIT PROCESSING IN SILICON

Ментор Марин Тадић

Потписани Берец Весна

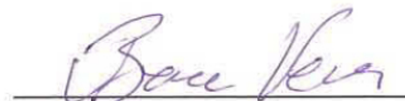
изјављујем да је штампана верзија мог докторског рада истоветна електронској верзији коју сам предао/ла за објављивање на порталу **Дигиталног репозиторијума Универзитета у Београду**.

Дозвољавам да се објаве моји лични подаци везани за добијање академског звања доктора наука, као што су име и презиме, година и место рођења и датум одбране рада.

Ови лични подаци могу се објавити на мрежним страницама дигиталне библиотеке, у електронском каталогу и у публикацијама Универзитета у Београду.

Потпис докторанда

У Београду, 14. 10. 2013.



Прилог 3.

Изјава о коришћењу

Овлашћујем Универзитетску библиотеку „Светозар Марковић“ да у Дигитални репозиторијум Универзитета у Београду унесе моју докторску дисертацију под насловом:

ION-ATOM QUANTUM ENTANGLEMENT IN A MAGNETIC FIELD BASED ON THE
SUPERFOCUSING EFFECT - THE SPIN QUBIT PROCESSING IN SILICON

која је моје ауторско дело.

Дисертацију са свим прилозима предао/ла сам у електронском формату погодном за трајно архивирање.

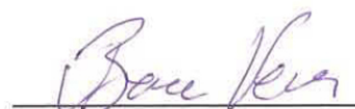
Моју докторску дисертацију похрањену у Дигитални репозиторијум Универзитета у Београду могу да користе сви који поштују одредбе садржане у одабраном типу лиценце Креативне заједнице (Creative Commons) за коју сам се одлучио/ла.

1. Ауторство
2. Ауторство - некомерцијално
3. Ауторство – некомерцијално – без прераде
4. Ауторство – некомерцијално – делити под истим условима
5. Ауторство – без прераде
6. Ауторство – делити под истим условима

(Молимо да заокружите само једну од шест понуђених лиценци, кратак опис лиценци дат је на полеђини листа).

Потпис докторанда

У Београду, 14. октобар 2013.



1. Ауторство - Дозвољавање умножавање, дистрибуцију и јавно саопштавање дела, и прераде, ако се наведе име аутора на начин одређен од стране аутора или даваоца лиценце, чак и у комерцијалне сврхе. Ово је најслободнија од свих лиценци.
2. Ауторство – некомерцијално. Дозвољавање умножавање, дистрибуцију и јавно саопштавање дела, и прераде, ако се наведе име аутора на начин одређен од стране аутора или даваоца лиценце. Ова лиценца не дозвољава комерцијалну употребу дела.
3. Ауторство - некомерцијално – без прераде. Дозвољавање умножавање, дистрибуцију и јавно саопштавање дела, без промена, преобликовања или употребе дела у свом делу, ако се наведе име аутора на начин одређен од стране аутора или даваоца лиценце. Ова лиценца не дозвољава комерцијалну употребу дела. У односу на све остале лиценце, овом лиценцом се ограничава највећи обим права коришћења дела.
4. Ауторство - некомерцијално – делити под истим условима. Дозвољавање умножавање, дистрибуцију и јавно саопштавање дела, и прераде, ако се наведе име аутора на начин одређен од стране аутора или даваоца лиценце и ако се прерада дистрибуира под истом или сличном лиценцом. Ова лиценца не дозвољава комерцијалну употребу дела и прерада.
5. Ауторство – без прераде. Дозвољавање умножавање, дистрибуцију и јавно саопштавање дела, без промена, преобликовања или употребе дела у свом делу, ако се наведе име аутора на начин одређен од стране аутора или даваоца лиценце. Ова лиценца дозвољава комерцијалну употребу дела.
6. Ауторство - делити под истим условима. Дозвољавање умножавање, дистрибуцију и јавно саопштавање дела, и прераде, ако се наведе име аутора на начин одређен од стране аутора или даваоца лиценце и ако се прерада дистрибуира под истом или сличном лиценцом. Ова лиценца дозвољава комерцијалну употребу дела и прерада. Слична је софтверским лиценцама, односно лиценцама отвореног кода.